Conjunctive Management of Water Resources in IGNP Command

Final Report

Funded by:

NATIONAL INSTITUTE OF HYDROLOGY, ROORKEE
DoWR, RD & GR, Ministry of Jal Shakti, Govt. of India

GROUNDWATER HYDROLOGY DIVISION
NATIONAL INSTITUTE OF HYDROLOGY, ROORKEE

March 2025

PROJECT TEAM

PI	Dr. Nitesh Patidar, Scientist-C
Co-PIs	Dr. MK Goel, Scientist-G
	Dr. Anupma Sharma, Scientist-G
	Dr. Gopal Krishan, Scientist-E
	Dr. Surjeet Singh, Scientist – G
	Dr. Sumant Kumar, Scientist-E

TABLE OF CONTENTS

LIST OF FIGURES

* * *

LIST OF TABLES

* * *

CHAPTER – 1

INTRODUCTION

1.1 Background

The Indira Gandhi Nahar Pariyojana (IGNP) is one of India's largest canal projects. Its implementation began in the late 1950s in two stages. It covers the districts of Sri Ganganagar, Hanumangarh, Bikaner, Churu, Jaisalmer, Barmer and Jodhpur in the state of Rajasthan. It is one of the largest irrigation systems in the world, with a cultural command area (CCA) of 1.963 million hectares, comprising many canals and irrigation structures. It ensures the cultivation of wheat, pulses, and oil seeds and hence contributes to the growth of this region economically. It also transforms the desert environment within which it falls. Moreover, through the increase in vegetation in the command area, otherwise dust storm-prone areas have been reclaimed; several plant and animal species have found new habitats. Additionally, due to the IGNP project, potable water is made available for use by people residing within the Thar Desert and other areas across Rajasthan state, which is one of the country's driest parts. The IGNP canal system exemplifies how visionary irrigation systems combined with efficient water usage in agriculture can help societies adjust to adverse climatic conditions.

The IGNP project has two stages; its first part is covered by a feeder that is approximately 204 km long and has its origin at Harike Barrage in Punjab up to Masitawali in Rajasthan. From there, a 189 km long main canal runs from Masitawali to Chattergarh in Bikaner district. Stage II comprises a 256 km long main canal from Chattergarh to Mohangarh in Jaisalmer. It also includes a distributary canal network of about 3,600 kilometres. Changes in climate, soil type and topography differentiate its command area from surrounding regions. It is quite challenging to grow crops in the Thar Desert due to shifting sand dunes, sparse and unevenly distributed rainfall, severe temperature fluctuations and periodical droughts. In the Kharif season, mainly, crops like pearl millet, bajra, pulses, sesamum, groundnut, sugarcane and guar are cultivated, while the Rabi season mainly involves the cultivation of wheat, barley and gram. Paddy, sugarcane, cotton, and mustard are also grown. Ustic and hyperthermic types of moisture and thermic regimes are used to classify the region’s soils in relation to climatic characteristics. These soils are also at risk of moderate to strong wind erosion and are situated at an altitude of over 180-200 meters above sea level. Plains with sandy soils, sand dunes, flood plains depressions and inter-dunal flats are typical features of the area. A report produced by the FAO/UNDP in 1971 revealed that of 2.2 million hectares, 59% is non-irrigable, while 80% of irrigated land is sandy. Reportedly the water level rises at a rate of 1-2 meters a year (Government of Rajasthan 1999). Challenges such as flood irrigation practices, seepage from canals, sandy soil texture, and lack of natural surface drainage present a major hindrance to the sustainability of irrigated agriculture.

The water availability in the IGNP canal has been a crucial factor in changing the arid lands into productive agricultural fields, thus greatly stimulating the region's agricultural economy. However, it is also accompanied by an unintended consequence of waterlogging. In some places where the canal based extensive irrigation occurs, the soil has accumulated excess water than it can hold naturally. Consequently, there is an increase in soil salinity and a decrease in plant root oxygen that results from waterlogging. The major sources of seepage in the main canal, according to the Central Water and Power Research Centre (CWPRC), are silt content between 25-50% and fine to medium sediment between 50-75%, which are highly permeable to water, and breaches in the canal lining. In this area, the absence of natural drainage worsens the situation because there are no rivers through which surface run-off occurs, even though historical records indicate the presence of rivers here in the past. In contrast, the geological composition characterised by layers of sand, clay, silt and occasional gravel prevents further percolation down into the ground due to the formation of a hard pan. Furthermore, the soil properties in the IGNP region also contribute to this problem. These soils are part of extensive floodplains mixed with aeolian deposits that are prone to salinity and alkalinity issues.

Conjunctive management of surface water and groundwater for irrigation is recognized as an effective solution to water logging and root zone salinity. The conjunctive utilization of water resources also ensures consistent water availability for irrigation and support sustainable water management. However, despite these advantages the conjunctive management of water resources is scant in canal commands. The Indira Gandhi Nahar Pariyojana (IGNP) provides irrigation to an area of 1.963 million hectare (CCA) in Rajasthan. The project also provides domestic water supply to most of the Thar Desert of Rajasthan and is therefore the most important water source in the arid Rajasthan. Since the inception of the project, there have been various issues related to rising water table and increasing soil salinity. Several studies were conducted to assess the impact of canal on groundwater levels and water logging. It was observed that before the canal construction (before 1952) the depth to groundwater used to vary between 40 and 50 m. After the inception of irrigation through Stage-I of IGNP, groundwater level started rising. In 1972-82 the rise in groundwater level was observed to be 1.17 m/year. Later in 1995, an area of around 10% of CCA of Stage-I was waterlogged and around 25% area was under critical condition (depth to GW in range 1-6 m). Such rise in groundwater level transports the salts from deeper soil layers to surface and impact the agricultural productivity in the area.

The present scenario of groundwater and mapping of water-logged area is essential in the IGNP command for effective management of land and water resources. Such analysis would help in quantifying the current potential of groundwater in conjunction with canal water to maximize the irrigation potential in command and to contain salt mobilization in root zone.

1.2 Objective and Scope of Study

The major objectives of this study are as follows:

1. Analysis of present groundwater scenario in enroute command of IGNP.
2. Mapping of water-logged area in IGNP command using remote sensing.
3. Estimation of GW recharge from rainfall, canal and irrigation under present and future climatic scenarios.
4. Conjunctive management of water resources in enroute command area of IGNP canal.

* * *

CHAPTER – 2

STUDY AREA AND DATABASE DEVELOPMENT

2.1 The Study Area

The IGNP project was initiated in the late 50’s and is situated in the districts of Sriganganagar, Hanumangarh, Bikaner, Churu, Jaisalmer, Barmer, and Jodhpur. It has a CCA of 1.963 million hectares. The project was completed in two stage, Stage-I having a 204 km long feeder which originates from Harike Barrage, Punjab, to reach Masitawali, Rajasthan, and a 189 km long main canal from Masitawali to Chattergarh in Bikaner district. Stage-II encompasses a 256 km long main canal from Chattergarh to Mohangarh in Jaisalmer. The project has played an important role in providing irrigation and water supply to the arid regions of Rajasthan thereby improving the livelihoods of farmers. Additionally, it has supported afforestation efforts, reduced desertification, and contributed to the recharge of groundwater in certain areas.

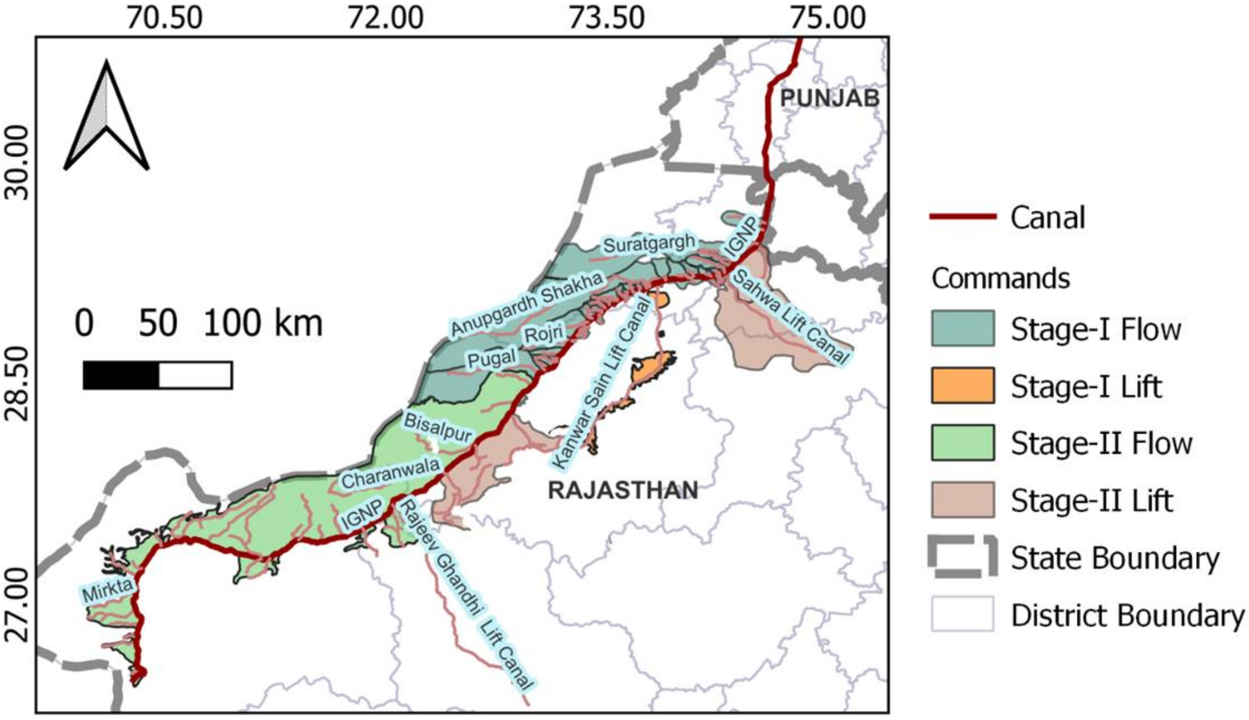

Figure – 2.1: Indira Gandhi Nahar Pariyojna (IGNP) command area under stage-I and stage-II

2.1.1 Basin topography

The IGNP region lies in the arid and semi-arid zones of Rajasthan, with land elevations ranging from around 100 to 250 meters above sea level. The topography is predominantly flat or gently undulating, though the landscape is interrupted by sand dunes, which vary in height and cover a significant portion of the area. These dunes are both stabilized and shifting, with some stabilized by vegetation and others moving with the seasonal winds. The original desert landscape had sparse natural drainage, and surface water was virtually absent before the introduction of the canal. The topography map of the IGNP command is shown in **Figure 2.2**.

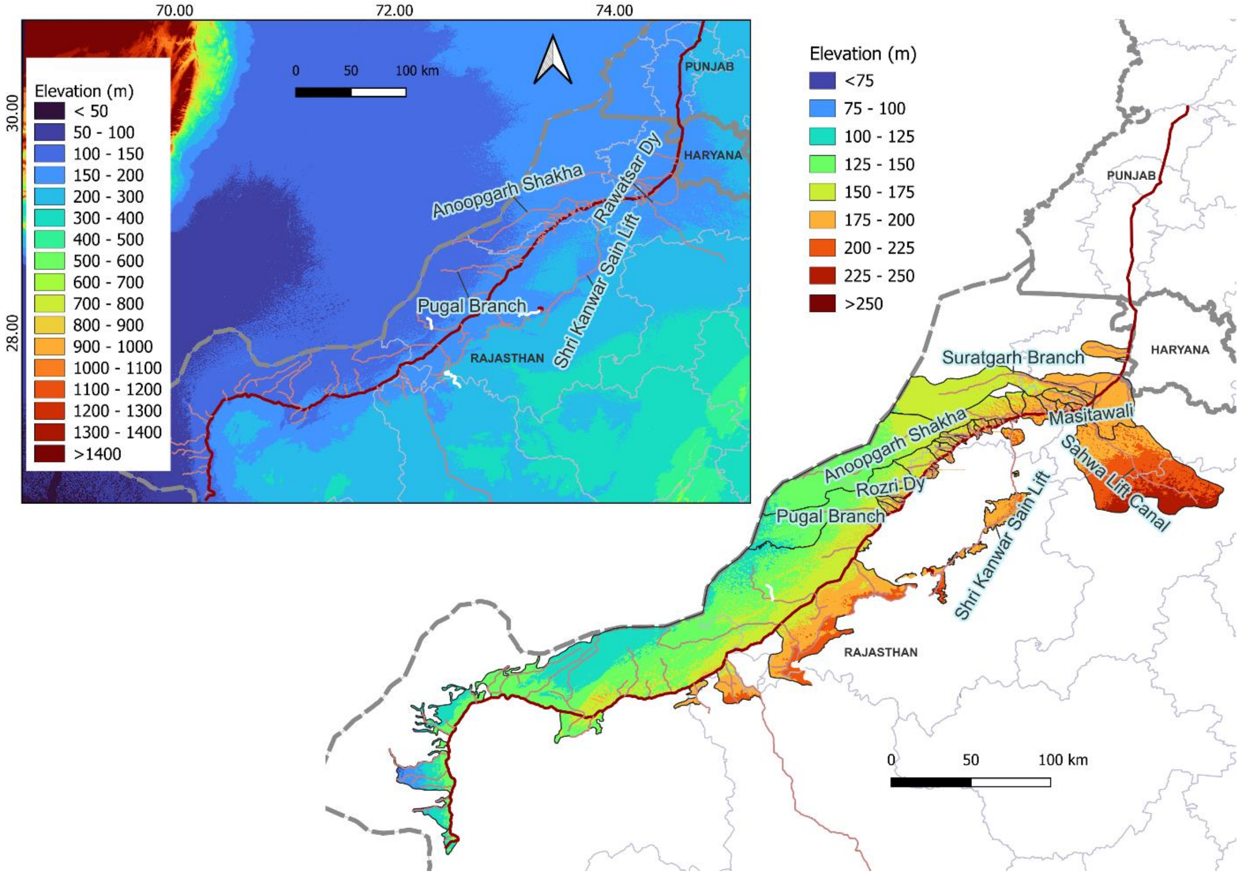

Figure – 2.2: Elevation map of the command area under IGNP.

2.2 Database Development for the Study Area

The impact analysis of various scenarios for the study area requires various spatial and non-spatial data. Land use/Land cover (LULC) map, topography, soil map, hydro-meteorological data, cropping pattern and crop characteristics, CGWB estimations and groundwater (GW) observations, canal system characteristics etc. are some of the key inputs for the analysis. For the study domain, various kind of spatial, temporal, and other data have been developed/collected from different sources.

2.2.1 Digitization of IGNP canal and enroute commands

The GIS layers of IGNP canal and enroute commands were developed through on-screen digitization in GIS software using the map provided by Water Resources Department (North), Rajasthan. The digitization was performed cautiously to obtain maximum accuracy. After digitization, the created shapefiles were thoroughly checked by overlaying them on high-resolution Google Earth images.

2.2.2 Land use land cover (LULC) maps

The Land Use Land Cover (LULC) map of IGNP canal command area provides a comprehensive view of the land utilization patterns and vegetation cover from 2016 to 2022. This map categorizes the IGNP area based on the dominant types of land cover, including agricultural fields that are utilized during different cropping seasons (Kharif and Rabi) and areas with mixed land use (Fig. 2.3). This categorization allows for better understanding of the region's agricultural and environmental dynamics, highlighting the influence of IGNP in transforming a traditionally arid region into a cultivated and productive landscape. The map reflects the transformation brought by IGNP in terms of land cover change and agricultural expansion in the region. By providing reliable irrigation, IGNP has enabled both seasonal and year-round cropping in areas that were previously arid and sparsely vegetated. Regions with Kharif-only and Rabi-only crops indicate reliance on seasonal irrigation or rainfall, while areas with dual cropping signify regions with ample water availability to support continuous agriculture.

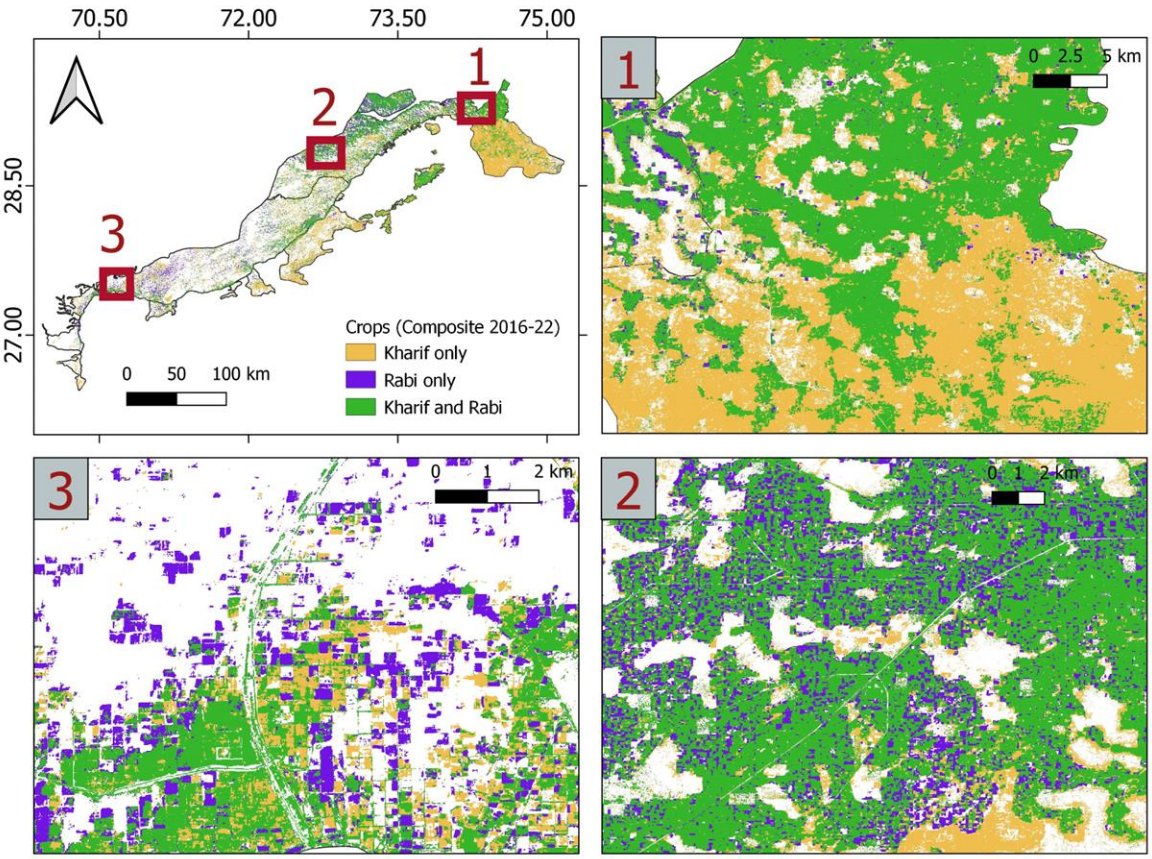

Figure – 2.3: LULC map from the year 2016-22

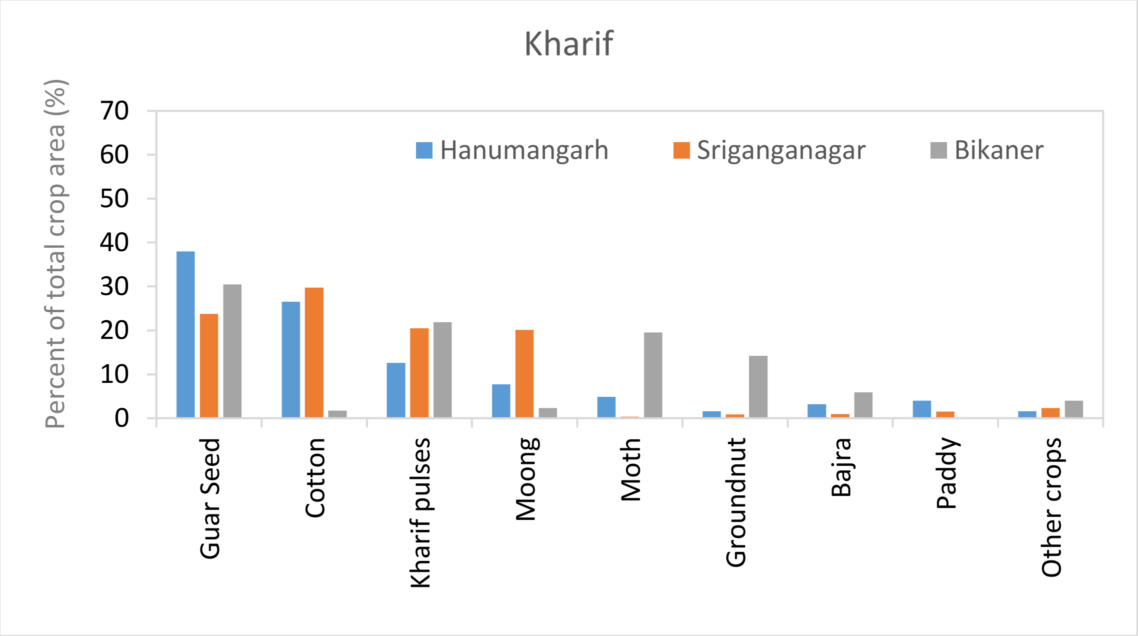

Figure – 2.4: Kharif crops in the command area.

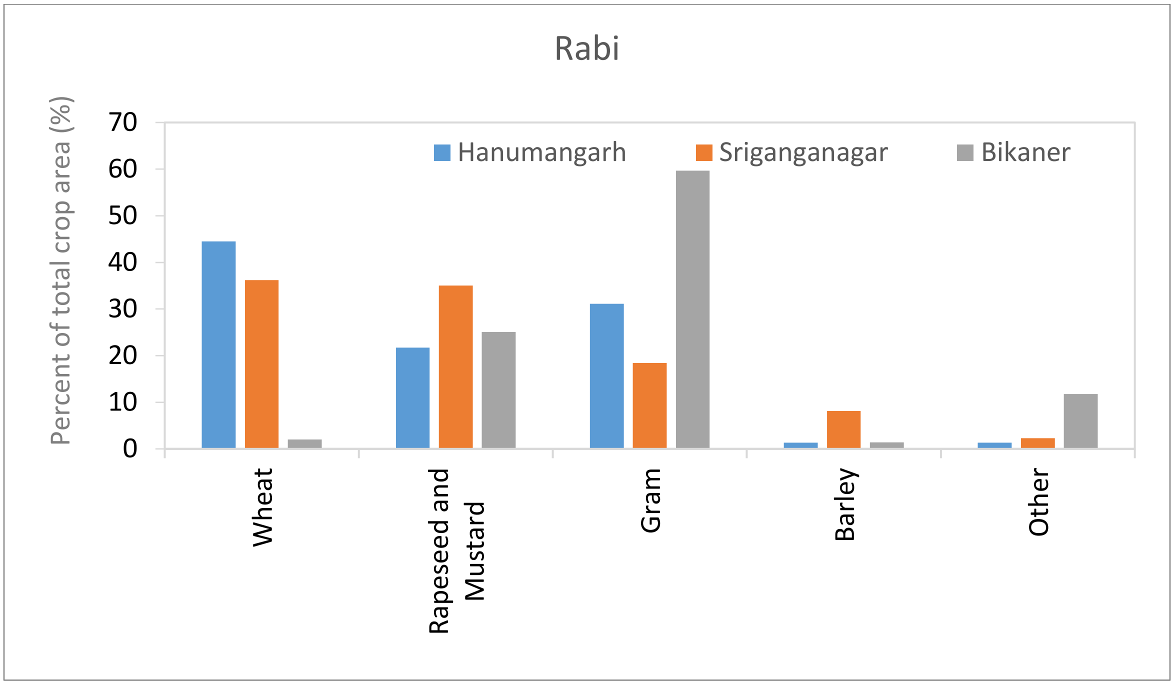

Figure – 2.5: Rabi crops in the command area.

The **Figures 2.4** and **2.5** display the distribution of crop areas in the Kharif and Rabi seasons across three districts: Hanumangarh, Sriganganagar, and Bikaner in the IGNP command area. These graphs, expressed in percentages of the total crop area, offer insights into the cropping patterns and agricultural priorities across these regions within the IGNP canal command area. In the Kharif season, Hanumangarh district shows a diverse mix of crop types, with several crops occupying moderate percentages of the total area. Hanumangarh's reliance on Kharif season crops suggests a favorable climate and adequate water availability for Kharif agriculture. Sriganganagar's crop distribution during the Kharif season is marked by some peaks, indicating that a few crops dominate the Kharif agriculture in the district. The percentage values in several categories are slightly higher than those in Bikaner, suggesting a more intensive utilization of the land in the Kharif season. In Bikaner, Kharif crops occupy a smaller percentage of the total area compared to the other two districts. This could be due to limited water availability that restrict extensive Kharif season cultivation.

Overall, Hanumangarh and Sriganganagar show a higher percentage of land under Kharif cultivation compared to Bikaner, suggesting that these districts benefit from more favorable conditions or irrigation for Kharif season crops.The Rabi season exhibits distinct cropping preferences across the three districts. In Hanumangarh, Rabi crops cover a significant portion of the agricultural area, indicating the district's dependence on winter crops. The district shows a more even distribution of crop percentages compared to Kharif, suggesting a diverse cropping strategy for the Rabi season. Similar to the Kharif season, Sriganganagar has a pronounced peak in one crop type, which occupies a large percentage of the total Rabi crop area. This suggests that farmers in Sriganganagar may focus on particular high-yield or high-demand crops during the Rabi season, benefiting from reliable water supply. In Bikaner, the Rabi season appears to be more significant than the Kharif season in terms of land use. The percentage of land under certain Rabi crops is high, suggesting that winter cropping is more viable here, likely due to a reliance on stored water or winter moisture.

Hanumangarh and Sriganganagar demonstrate high percentages of land under cultivation for both Kharif and Rabi crops, indicating the extensive use of IGNP irrigation for year-round farming. Bikaner shows a greater emphasis on Rabi crops, reflecting the challenges of Kharif cultivation in an arid environment. Rabi crops, which benefit from cooler temperatures and stored moisture, appear to be a better fit for the region's climate.

2.2.3 Characteristics of IGNP Canal and its Distributaries

Cross-section of canals affect the flow characteristics and the evaporation and seepage losses. The top width affects the area of surface water which is exposed for evaporation. Further, the wetted perimeter and the run-time affects the seepage losses from the canals. Thus, it is important to consider the canal system characteristics to find various hydrological consequences. The characteristics of IGNP main canal in different stretches that is considered in present study is given in **Table 2.1**.

For different distributaries bifurcating from the main canal, discharge capacity and the length were available but the section details were not available. The same have been approximated by trial and error so that the discharge capacity of sections match with the given discharge capacity. Distributary details are provided in **Table 2.2**.

Table – 2.1

Cross-section details of IGNP canal in different sections

Segment ID	Segment (From – to)	Length (km)	Bed width (m)	Side slope (H:V)	Roughness Coefficient	Longitudinal Slope
1	Rathikhera to Masitawali	11.08	35	2:1	0.018	0.00012
2	Masitawali to Suratgarh	20.97	35	2:1	0.018	0.00012
3	Suratgarh to Zorawarpura	0.01	35	2:1	0.018	0.00012
4	Zorawarpura to Sardarpura	10.21	35	2:1	0.018	0.00012
5	Sardarpura to Khedasari	4.18	35	2:1	0.018	0.00012
6	Khedasari to Thethar	5.52	35	2:1	0.018	0.00012
7	Thethar to Kanau	5.10	35	2:1	0.018	0.00012
8	Kanau to Bhojewala1	6.91	35	2:1	0.018	0.00012
9	Bhojewala1 to Bhojewala2	3.32	35	2:1	0.018	0.00012

10	Bhojewala2 to Piperan	15.89	35	2:1	0.018	0.00012
11	Piperan to Anoopgarh	1.96	35	2:1	0.018	0.00012
12	Anoopgarh to Govinda	9.89	35	2:1	0.018	0.00012
13	Govinda to Birmana1	2.21	35	2:1	0.018	0.00012
14	Birmana1 to Birmana2	5.68	35	2:1	0.018	0.00012
15	Birmana2 to Dungiawali	4.43	35	2:1	0.018	0.00012
16	Dungiawali to Sukhchainpura	4.75	35	2:1	0.018	0.00012
17	Sukhchainpura to Bhaktawarpura	3.19	35	2:1	0.018	0.00012
18	Bhaktawarpura to Govindsar	4.32	35	2:1	0.018	0.00012
19	Govindsar to Bhopalpura	0.60	35	2:1	0.018	0.00012
20	Bhopalpura to Surjansar	6.38	35	2:1	0.018	0.00012
21	Surjansar to Gomawali	3.84	35	2:1	0.018	0.00012
22	Gomawali to Takhatpura	4.35	35	2:1	0.018	0.00012
23	Takhatpura to Kanakpura	7.81	35	2:1	0.018	0.00012
24	Kanakpura to Sherpura	4.17	35	2:1	0.018	0.00012
25	Sherpura to Rozri	19.02	35	2:1	0.018	0.00012
26	Rozri to Chattargarh	13.43	35	2:1	0.018	0.00012
27	Chattargarh1 to Chattargarh2	2.69	35	2:1	0.018	0.00012
28	Chattargarh2 to Awa	2.05	35	2:1	0.018	0.00012
29	Awa to Sattasar	11.47	35	2:1	0.018	0.00012
30	Sattasar to Pugal	4.56	35	2:1	0.018	0.00012
31	Pugal to Tharoosar	6.56	35	2:1	0.018	0.00012

Table – 2.2

Cross-section details of distributaries of IGNP canal

Name	**Bed width (m)**	**Water depth (m)**	**Area (ha)**	**Longitudinal Slope**	**Roughness Coefficient (n)**	**Computed capacity (cumec)**
Masitawali	12	3.1	60.19	0.00012	0.018	5.00
Suratgarh	32	5	412.78	0.00012	0.018	27.31
Zorawarpura	8	2	21.04	0.00012	0.018	1.59
Sardarpura	8	2	37.75	0.00012	0.018	1.59
Khedasari	35	6.5	25.73	0.00012	0.018	47.38
Thethar	2	0.8	2.29	0.00012	0.018	0.10

Kanau	35	6.5	12.64	0.00012	0.018	47.38
Bhojewala1	2	0.8	2.99	0.00012	0.018	0.10
Bhojewala2	35	6.5	49.93	0.00012	0.018	47.38
Piperan	2	0.8	2.43	0.00012	0.018	0.10
Anoopgarh	32	5	786.34	0.00012	0.018	27.31
Govinda	2	0.8	1.41	0.00012	0.018	0.10
Birmana1	2	0.8	2.44	0.00012	0.018	0.10
Birmana2	2	0.8	2.70	0.00012	0.018	0.10
Dungiawali	2	0.8	4.95	0.00012	0.018	0.10
Sukhchainpura	2	0.8	1.54	0.00012	0.018	0.10
Bhaktawarpura	3	0.8	4.80	0.00012	0.018	0.13
Govindsar	3	1	8.45	0.00012	0.018	0.20
Bhopalpura	2	0.8	2.74	0.00012	0.018	0.10
Surjansar	2	0.8	7.38	0.00012	0.018	0.10
Gomawali	5	1	11.87	0.00012	0.018	0.30
Takhatpura	2	0.8	5.62	0.00012	0.018	0.10
Kanakpura	4	1	9.14	0.00012	0.018	0.25
Sherpura	5	1	16.89	0.00012	0.018	0.30
Rozri	8	2	43.17	0.00012	0.018	1.59
Chattargarh1	6	1.5	12.84	0.00012	0.018	0.74
Chattargarh2	2	0.8	1.47	0.00012	0.018	0.10
Awa	6	1	16.96	0.00012	0.018	0.35
Sattasar	2	0.8	5.32	0.00012	0.018	0.10
Pugal	21	4	165.98	0.00012	0.018	12.69

2.3 Field Investigations

2.3.1 Geophysical Investigations

The geophysical investigations conducted in the IGNP region aim to unravel the subsurface characteristics and provide critical insights for water management and agricultural planning. The IGNP, situated in the arid and semi-arid zones of Rajasthan, India, represents a region where groundwater management and soil salinity mitigation are vital for sustaining agricultural activities. These investigations utilize Electrical Resistivity Tomography (ERT), a geophysical method renowned for its effectiveness in mapping subsurface resistivity variations.

The ERT surveys in the IGNP region have been meticulously conducted across 10 different locations, with the primary goal of understanding the resistivity distribution at various depths (**Table 2.3**). These measurements help identify zones of high and low resistivity, which correspond to variations in soil moisture, salinity, and geological formations. High-resistivity zones often indicate dry or coarse-grained materials, while low-resistivity zones are indicative of waterlogged or saline areas. Such information is invaluable for managing irrigation practices and ensuring the long-term sustainability of the canal command areas.

Table – 2.3

Table showing different ERT locations in IGNP command area

S.No	Location	ERT Code	Lat	Long	Electrode Spacing (m)	El-array
Field Visit 1 (April 2023)						
1	Near Tibbi	S1	29.527499	74.506366	5	Schlumberger
2	Near Shahid Bhagat Singh Law College	D2REV	29.587441	74.234267	5	Schlumberger
3	Near Badopal wines	S2	29.356685	74.090331	5	Schlumberger
4	RD315	315RD	29.125354	73.680077	5	Schlumberger
Field Visit 2 (November 2023)						
1	Kherwala	ignp4	29.264528	74.363029	5	Schlumberger
2	Chaya	CHAYA	29.260311	74.482273	5	Schlumberger
3	Chak1spd	CHAK1SPD	29.267242	74.301868	5	Schlumberger
4	Khedasari	KHEDASARI	29.288566	74.229035	10	Wenner-Schlumberger
5	Sardarpura	SARDARPURA	29.288214	74.167307	10	Mixed/Non-conventional
6	Rangmahal	RANGM	29.328065	73.944651	10	Mixed/Non-conventional

The measured resistivity pseudosections from these surveys provide a two-dimensional representation of the subsurface resistivity. This is complemented by calculated resistivity pseudosections, which are derived through inversion techniques. The iterative inversion process minimizes the discrepancy between measured and calculated data, achieving a close match with minimal error percentages. This ensures the reliability of the resistivity models generated for interpretation. The inverted resistivity sections reveal detailed insights into the subsurface. For example, regions with shallow, low-resistivity zones may signify areas prone to waterlogging due to excessive irrigation or poor drainage. Conversely, deeper high-resistivity layers may correspond to aquifers or sandy layers critical for groundwater recharge. The information gained from these surveys is pivotal in identifying and mitigating potential risks of salinization and waterlogging, which are significant challenges in the IGNP command areas.

The strategic placement of ERT survey points, as outlined in the geophysical campaign, ensures comprehensive spatial coverage across key areas of interest. Locations such as Sardarpura, Kherwala, Chaya, and others have been carefully analyzed to correlate resistivity variations with surface conditions and hydrogeological data. The integration of ERT results with other geospatial datasets enhances the precision of groundwater modeling and enables us to take necessary steps for agricultural and water resource management. The obtained resistivity at different locations is shown in **Figure 2.6(a-j)**. These results are utilized to define aquifer parameters during model calibration.

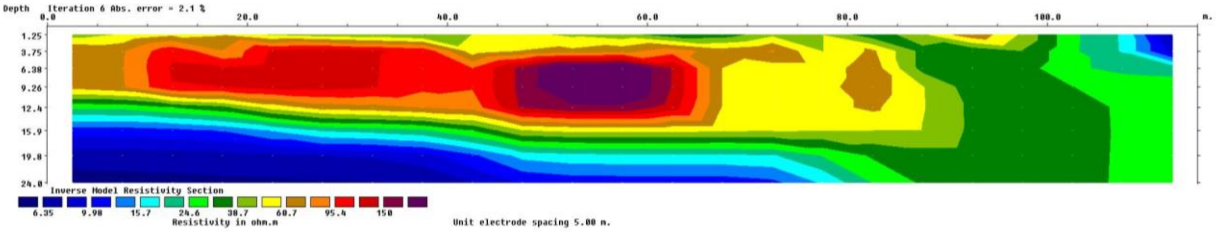

Figure – 2.6a: Resistivity section near Tibbi

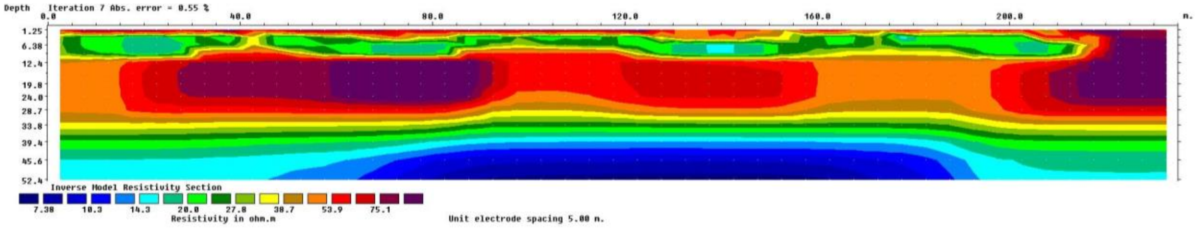

Figure – 2.6b: Resistivity section near Shahid Bhagat Singh Law College

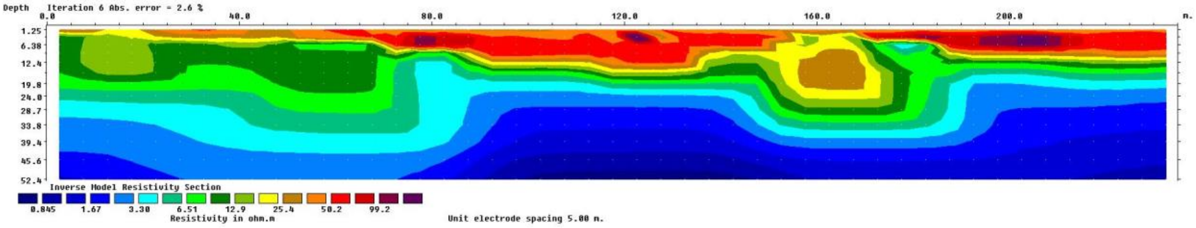

Figure – 2.6c: Resistivity section near Badopal Vines

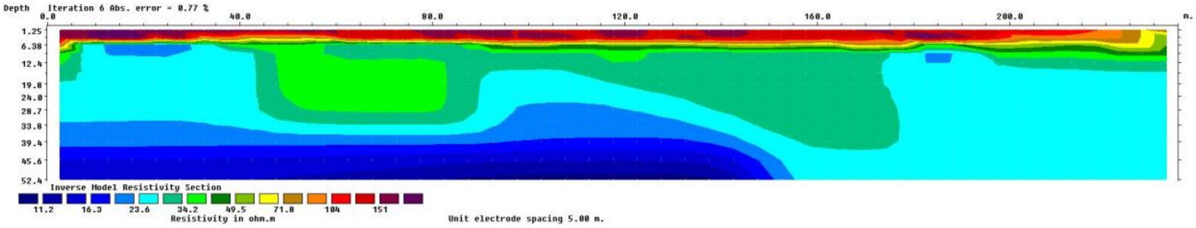

Figure – 2.6d: Resistivity section near RD315

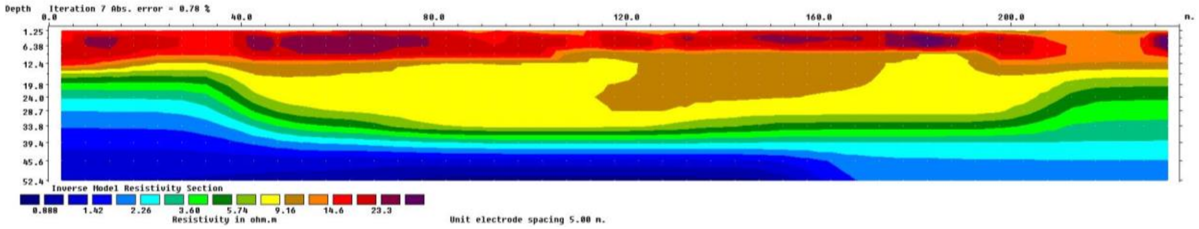

Figure – 2.6e: Resistivity section in Kherwala

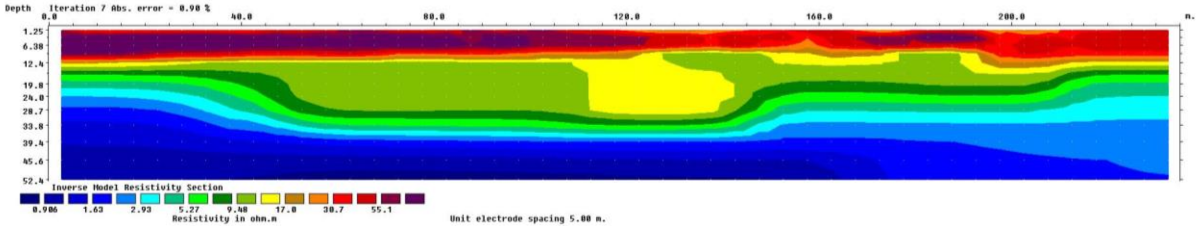

Figure – 2.6f: Resistivity section in Chaya

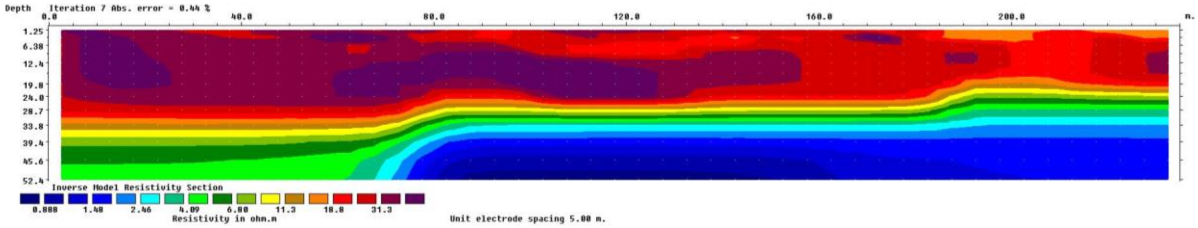

Figure – 2.6g: Resistivity section in Chak1spd

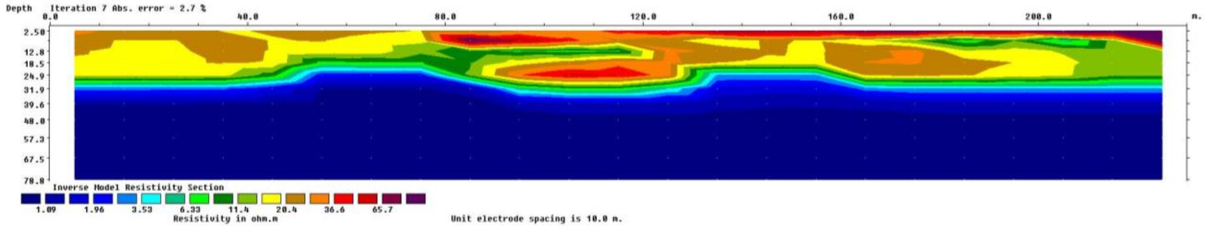

Figure – 2.6h: Resistivity section in Khedasari

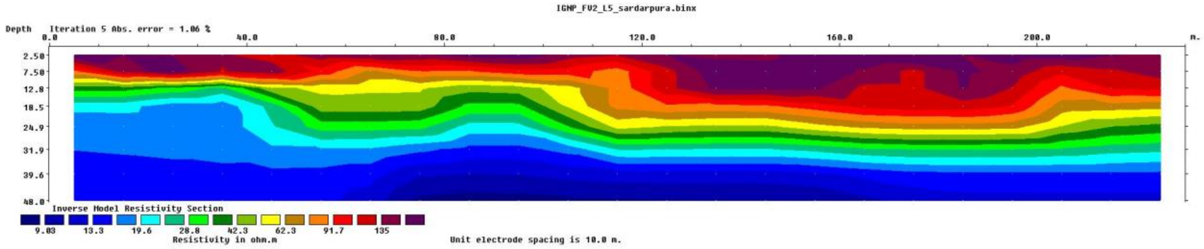

Figure – 2.6i: Resistivity section in Sardarpura

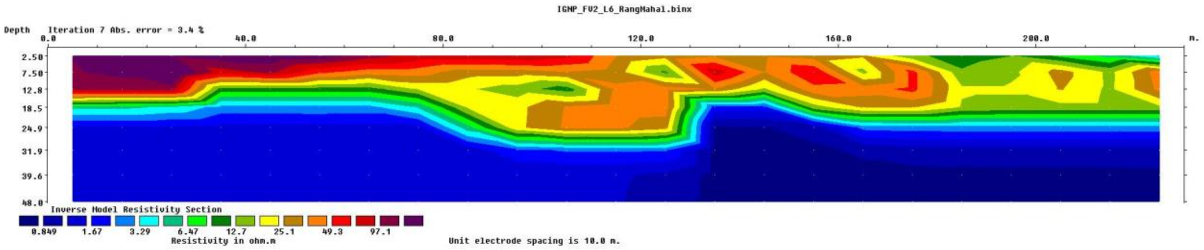

Figure – 2.6j: Resistivity section in Rangmahal

In addition to addressing current challenges, the geophysical investigations also provide a foundation for long-term monitoring and planning. By periodically repeating ERT surveys in the IGNP region, changes in subsurface conditions can be tracked over time. This enables the early detection of emerging issues, such as the encroachment of saline water into freshwater zones or the progressive degradation of soil health. Such insights are critical for adapting water management practices to the evolving needs of the region, particularly in the context of climate change and increasing water scarcity.

The process of creating a comprehensive ERT profile, as depicted in **Figure 2.8**, involved synthesizing individual resistivity sections from multiple ERT survey locations shown in **Figure 2.7**. Each ERT section provided detailed resistivity data at specific transects, capturing the subsurface characteristics at varying depths and locations. These sections were carefully aligned based on their spatial coordinates and interpolated to create a continuous subsurface profile. The interpolation process incorporated variations in resistivity values across adjacent ERT sections, allowing the generation of a seamless three-dimensional representation of the subsurface.

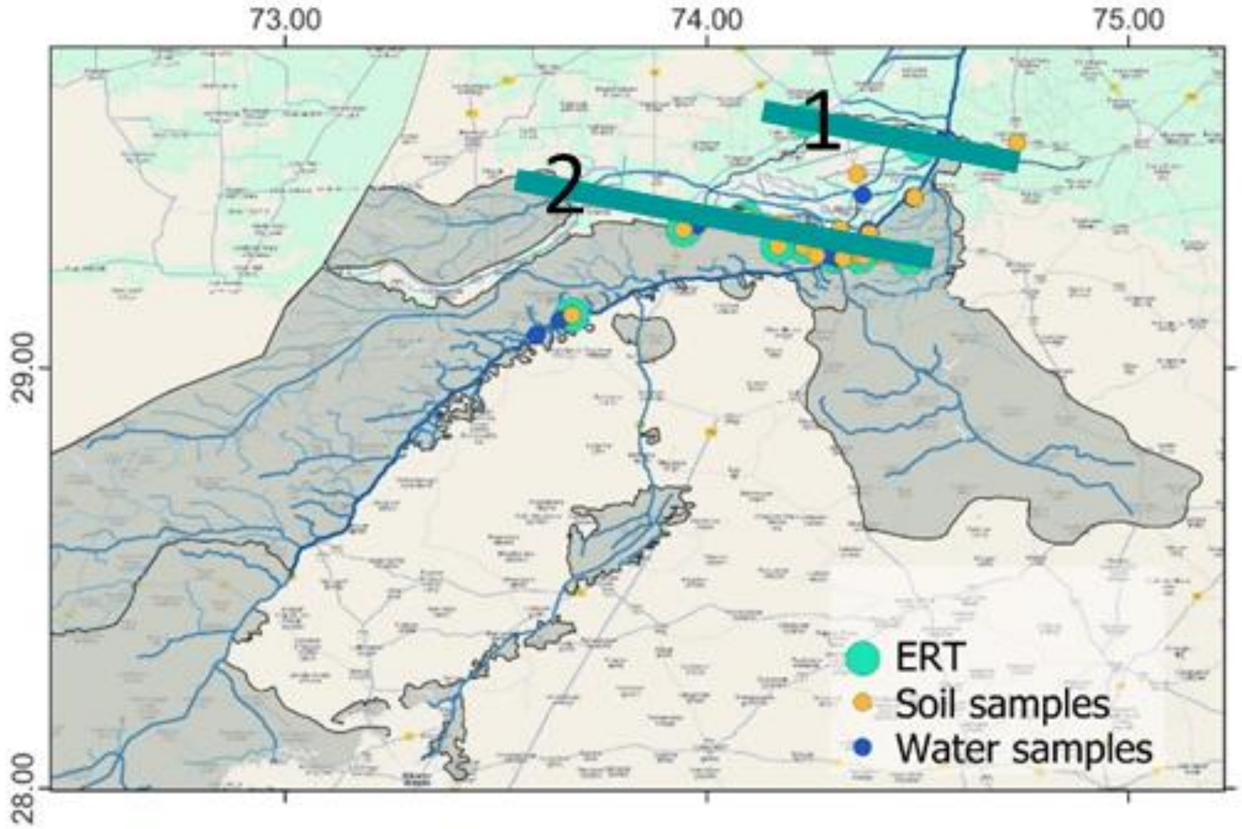

Figure – 2.7: Locations of ERT, soil and water sampling

In this comprehensive profile, distinct zones corresponding to freshwater, the fresh-saline water interface, saline water, and the unsaturated zone were identified. These zones were interpreted by analyzing the resistivity ranges observed in the individual ERT sections and correlating them with known hydrogeological conditions in the IGNP region. For example, low-resistivity values near the surface in some sections indicated potential waterlogging or saline conditions, while deeper high-resistivity values highlighted aquifer zones. By integrating these findings, the final profile accurately represented the spatial distribution of critical subsurface features.

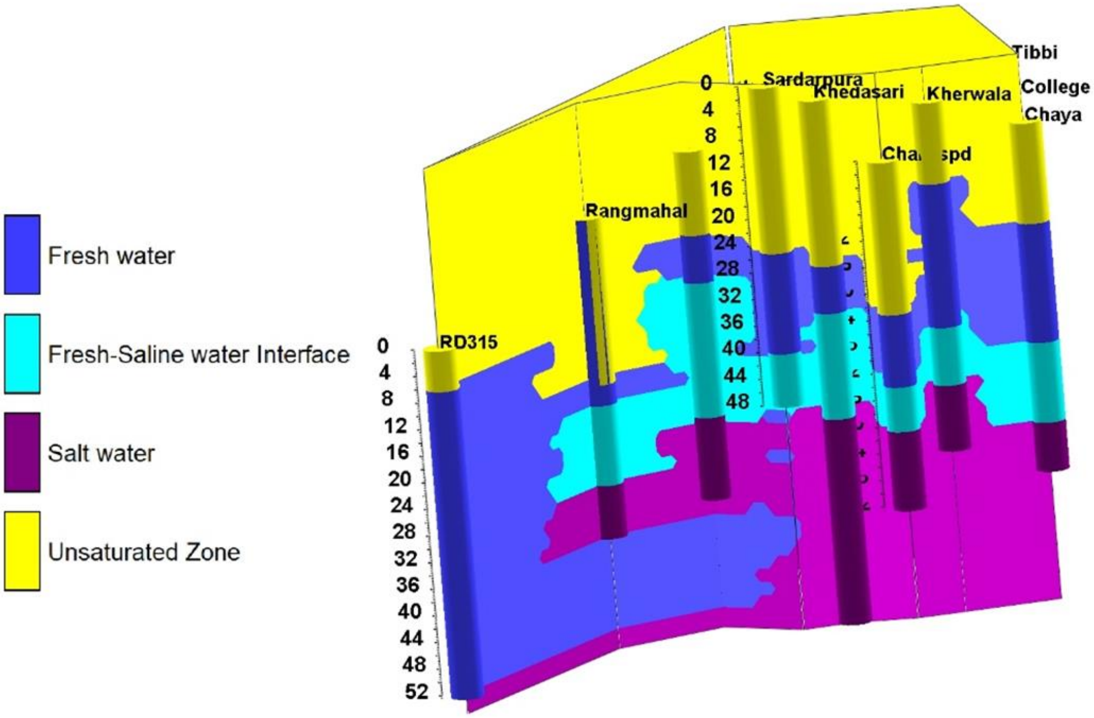

Figure – 2.8: ERT Profile Depicting Freshwater, Saltwater, and Unsaturated Zone Distribution in the IGNP Command Area

The geophysical investigations in the IGNP region underscore the critical role of advanced subsurface imaging techniques like ERT in addressing the challenges of waterlogging and salinity. By providing a detailed understanding of the subsurface resistivity distribution, these studies contribute significantly to the sustainable management of water resources and agricultural productivity in this region. The results not only improve current practices but also lay the foundation for future research and development in geophysical applications for canal command areas.

2.3.2 Water Quality Assessment

Water quality assessment in the IGNP region is a critical aspect of understanding the suitability of water for drinking, irrigation, and ecological health. The analysis of water samples collected from 29 different locations, including ponds, handpumps, and rivers, provides insights into both trace metal concentrations and general water quality parameters such as pH and electrical conductivity (EC).

The trace metal analysis revealed varying concentrations of elements such as Aluminum (Al), Arsenic (As), Cadmium (Cd), Chromium (Cr), Copper (Cu), Iron (Fe), Manganese (Mn), Nickel (Ni), Lead (Pb), and Zinc (Zn). Among these, Arsenic was detected in notable quantities in certain samples, such as Dabli Khurd Pond (18.85 ppb) and Tibbi Road Handpump (10.6 ppb), indicating potential contamination risks.

Manganese levels were found to be elevated in some samples, with Dabli Khurd Pond showing 227.27 ppb. Iron was present in small amounts, with concentrations typically below 0.2 ppm. Many trace metals, including Cadmium and Chromium, were below detection limits in most cases, suggesting minimal contamination by these elements (**Table 2.4 and 2.5**).

Table – 2.4

Trace Elements in Water Samples collected from IGNP

Sample Code	Al (ppb)	As (ppb)	Cd (ppb)	Cr (ppb)	Cu (ppb)	Fe (ppm)	Mn (ppb)	Ni (ppb)	Pb (ppb)	Zn (ppb)
IGNP-A1	70.26	18.85	ND	ND	ND	0.04	227.27	15.95	ND	26.95
IGNP-A2	ND	ND	ND	ND	5.32	0.18	4.45	ND	ND	90.46
IGNP-A3	ND	10.6	ND	ND	ND	ND	9.84	ND	ND	460.16
IGNP-A4	128.82	11.25	ND	ND	6.25	0.18	39.65	ND	ND	166.68
IGNP-A5	14.33	6.56	ND	ND	14.98	0.43	5.33	ND	ND	1486.64
IGNP-A7	53.77	11.12	ND	ND	1.64	0.06	18.04	ND	ND	57.45
IGNP-A 8	43.71	ND	ND	ND	7.17	0.51	14.34	ND	ND	382.55
IGNP-A 9	57.46	7.44	1.06	5.82	9.39	0.04	4.27	2.27	ND	43.46
IGNP-A 10	50.18	10.19	ND	ND	ND	0.07	18.46	ND	ND	14.1
IGNP-A 11	26.64	ND	ND	ND	1.9	0.08	66.86	ND	ND	8.92
IGNP-A 12	1678.36	18.54	ND	ND	ND	1.42	61.59	ND	ND	ND
IGNP- A13	15.18	10.76	ND	ND	1.84	ND	10.99	ND	ND	263.07
IGNP- A14	ND	7.33	ND	ND	ND	ND	ND	ND	ND	142.66
IGNP- A15	19.92	8.79	ND	ND	ND	0.01	7.56	ND	ND	38.19
IGNP- A16	3.42	8.21	ND	ND	ND	ND	ND	ND	ND	13.49
IGNP- A17	ND	8.08	ND	ND	1.7	ND	ND	ND	ND	8.79

Table – 2.5

Water sample details of various samples collected in IGNP command area

S. No.	Sample Code/ID	Lat.	Long	Location	Source
1	IGNP-A1	29.405537	74.487336	Dabli Khurd Pond	Pond
2	IGNP-A2	29.402873	74.488056	Dabli Khurd	Handpump

3	IGNP-A3	29.557564	74.450449	19 Ggr, Tibbi Road	Handpump
4	IGNP-A4	29.557503	74.454329	19 Ggr, Tibbi Road	River
5	IGNP-A5	29.514858	74.583114	Near Talwara Police Stn	Handpump
6	IGNP-A7	29.541166	74.557807	Tibbi Ellenabad Road Canal	Canal
7	IGNP-A8	29.541212	74.558189	Tibbi Ellenabad Road	Handpump
8	IGNP-A9	29.328885	74.315779	Jorawarpura	Borewell
9	IGNP-A10	29.317655	74.316193	Ghaggar River	River
10	IGNP-A11	29.260017	74.308504	Khetawali Rani	River
11	IGNP-A12	29.262479	74.307818	Khetawali Rani 2	Pond
12	IGNP-A13	29.363558	74.075040	Badopal Pond	Pond
13	IGNP-A14	29.125748	73.679213	RD 715	Handpump
14	IGNP-A15	29.078064	73.595398	RD 350	Handpump
15	IGNP-A16	29.114053	73.651727	RD 315	Pond
16	IGNP-A17	29.078610	73.594796	RD 315 Canal	Canal
17	IGNP-B1	29.409985	74.369313	15 Ndr-A	Canal
18	IGNP-B2	29.327009	74.382191	1 Stb	Canal
19	IGNP-B3	29.319019	74.386435	1 Stb	Handpump
20	IGNP-B4	29.265441	74.364310	3 Zwm	Borewell
21	IGNP-B5	29.260375	74.481644	Kanwani Rd	Borewell
22	IGNP-B6	29.266728	74.301029	5 Spd-A	Borewell
23	IGNP-B7	29.262429	74.307818	5 Spd-A	Pond
24	IGNP-B8	29.260017	74.308504	4 Spd	Canal
25	IGNP-B9	29.262953	74.304572	5 Spd-A	Handpump
26	IGNP-B10	29.266476	74.285785	5 Spd-A	Handpump
27	IGNP-B11	29.331610	74.191451	14 Spd	Handpump
28	IGNP-B12	29.356719	74.059671	2 Brp Rcp	Borewell
29	IGNP-B13	29.338975	73.977691	Rangmahal	River

General water quality parameters also varied significantly across locations. The pH of the samples ranged from 5.73 in Kanwani Road to 9.49 in 19 Ggr, Tibbi Road, indicating variations from slightly acidic to highly alkaline water. Most water sources were on the alkaline side, particularly ponds and canal water. Salinity, measured as electrical conductivity, varied widely, with borewell samples like 2 Brp Rcp showing extreme values of 25 mS, indicating severe salinity concerns. Other borewell locations, such as 3 Zwm and Kanwani Road, also recorded high salinity levels of 5100 µS and 3600 µS, respectively. In contrast, canal water samples generally showed lower EC values, such as 370 µS at 15 Ndr-A and 290 µS at 4 Spd, making these sources relatively more suitable for irrigation and domestic use.These findings raise important concerns about the usability of water in the IGNP region. For drinking purposes, the presence of Arsenic in some locations could pose health risks if concentrations approach or exceed permissible limits. High salinity levels, indicated by elevated EC values, may also render the water unsuitable for consumption without appropriate treatment. For agricultural use, saline water could adversely affect crop health and soil properties, necessitating the adoption of effective irrigation management practices. The observed high pH levels also point to potential challenges for aquatic ecosystems, emphasizing the need for regular monitoring to understand and address long-term impacts.

Handpumps exhibited moderate variability in salinity and pH. For instance, samples from 5 Spd-A had EC values ranging from 1450 µS to 2800 µS, with pH levels between 7.51 and 7.65. Rivers, such as the sample collected from Rangmahal, recorded an EC of 6600 µS with a neutral pH of 7.49, indicating high levels of dissolved salts but a balanced pH. Pond water, such as at 5 Spd-A, displayed a combination of high salinity (5200 µS) and alkalinity (pH 8.17), reflecting the influence of evaporation and dissolved minerals.

The findings highlight spatial variability in water quality across the IGNP region. Canal and river water generally had lower salinity levels, making them more suitable for agricultural use compared to borewell and pond water, which exhibited higher salinity and greater pH variability. Borewell samples, particularly from 2 Brp Rcp, 3 Zwm, and Kanwani Road, were of particular concern due to extreme salinity levels, which pose challenges for both drinking and irrigation purposes. High salinity can degrade soil quality, reduce crop productivity, and necessitate costly treatment for safe consumption.

This assessment highlights the critical need for continuous monitoring and targeted management of water quality in the IGNP region. Areas with elevated salinity or trace metal contamination require immediate attention, including the implementation of treatment facilities and exploration of alternative water sources. Sustainable irrigation practices must be adopted to mitigate the adverse effects of saline water on agriculture. By addressing these challenges proactively, the IGNP region can ensure the long-term usability and safety of its vital water resources.

Figure – 2.9: A Highly Saline Pond at Dabli Khurd (EC: 20 mS/cm)

2.3.3 Isotope Analysis

The isotope analysis of water samples collected from the IGNP command area provides valuable insights into the hydrological and environmental processes influencing water sources. Samples were obtained from diverse sources, including ponds, rivers, canals, and groundwater, across various locations in the command area. These samples were analyzed for stable isotopes of oxygen ($\delta^{18}O$) and hydrogen (δD), which serve as indicators of the water's origin and history.

The $\delta^{18}O$ and δD values vary significantly across the sampled locations, reflecting the isotopic signatures of different hydrological processes. For instance, the isotope values for water sourced from ponds, such as the sample from Dabli Khurd Pond ($\delta^{18}O$: 3.10, δD: 8.43), suggest significant evaporation, a common characteristic of surface water bodies exposed to high temperatures and arid conditions. Conversely, groundwater samples, such as those from handpumps in Dabli Khurd and 19 Ggr, Tibbi Road, exhibit depleted isotopic signatures ($\delta^{18}O$: -6.85 to -6.33, δD: -43.79 to -41.72), indicating recharge from precipitation with minimal evaporative influence.

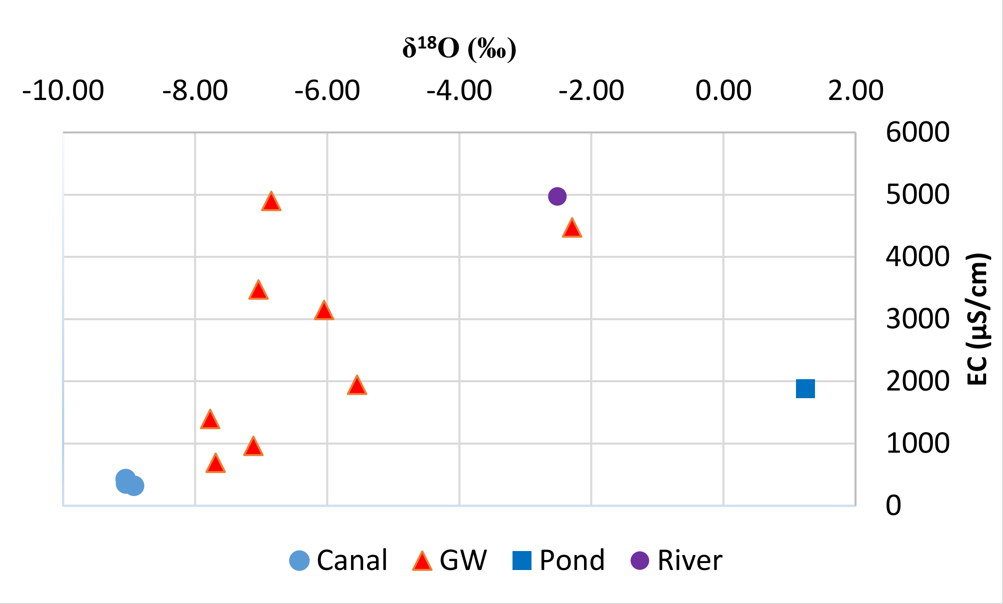

Figure – 2.10: Relationship between EC and δ¹⁸O for Different Water Sources: River, Groundwater, Canal, and Pond for IGNP region

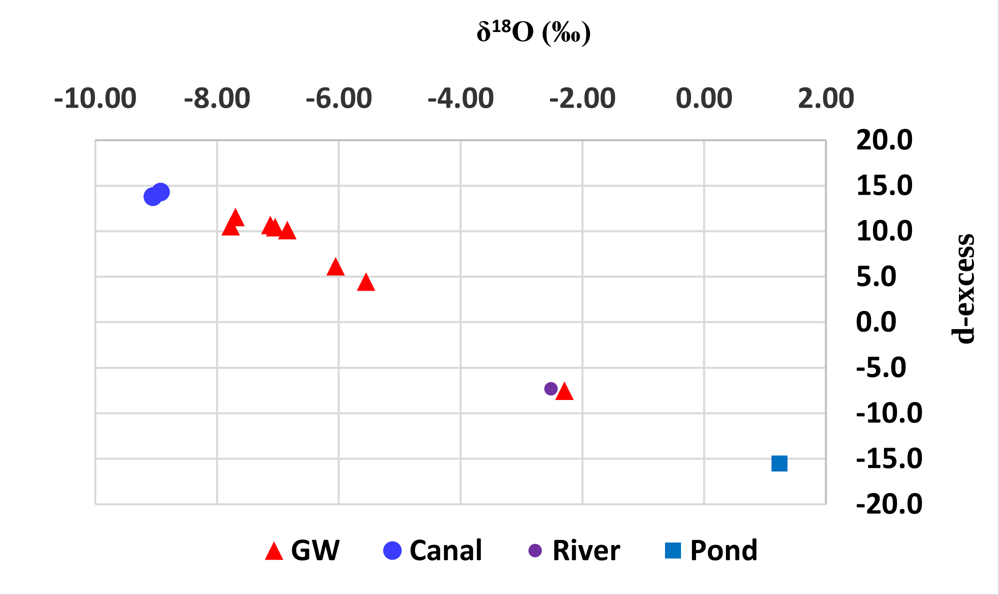

Figure – 2.11: Variation of δ¹⁸O and d-excess Across Different Water Sources

Figures 2.10, 2.11 and 2.12 demonstrate the clustering of samples along distinct isotopic trends, with groundwater samples aligning closely with the global meteoric water line (GMWL) and the Indian meteoric water line (IMWL). This alignment indicates that groundwater is primarily recharged by meteoric water with limited secondary processes. In contrast, canal and pond samples deviate from these lines, showing higher $\delta^{18}O$ and δD values due to evaporation. The d-excess values further reinforce these findings, with lower values in surface water sources highlighting significant evaporative enrichment.

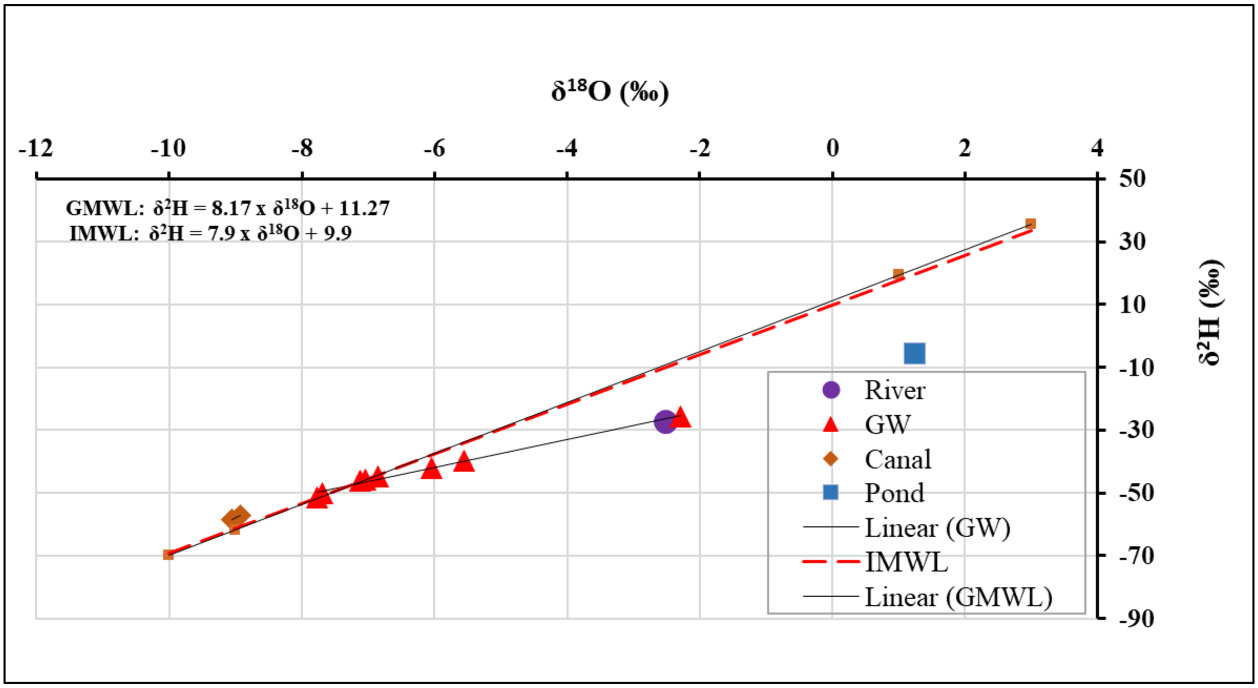

Figure – 2.12: Stable Isotope Analysis of $\delta^{18}O$ and δ^2H for Water Sources: Comparison of Global and Local Meteoric Water Lines for IGNP region

The spatial map of sampling locations highlights the geographic distribution of isotopic variation, with groundwater samples predominantly collected from areas near the IGNP canal. This spatial correlation supports the hypothesis that canal seepage contributes to groundwater recharge in the region. The mixing trends observed in the $\delta^{18}O$-δD plot further suggest interactions between groundwater and canal water, emphasizing the dynamic exchange between these sources. Additionally, the figures provide evidence that groundwater contributes to river flow in certain areas, as indicated by the isotopic overlap between river and groundwater samples.

Laboratory analysis confirmed these findings, with unique identifiers assigned to each sample for quality assurance. The combination of isotopic data, geographic coordinates, and hydrological trends enables the development of spatial maps and predictive models, aiding in the visualization of water resource dynamics. This isotope analysis underscores the importance of integrating geochemical tools with field observations and spatial data to understand and manage water resources sustainably within the IGNP command area.

* * *

CHAPTER – 3

CLIMATE ANALYSIS AND PROJECTION SCENARIOS

3.1 Introduction

As per the latest climate change assessment reports (ARs) by the Intergovernmental Panel on Climate Change (IPCC 2023), recent anthropogenic emissions remain the primary driver of global warming, which has exhibited widespread impacts on Earth's ecosystems and water resources. Greenhouse gas (GHG) emissions, especially carbon dioxide and methane, have continued to rise, with an accelerated increase in the past few decades. Between 2010 and 2020, emissions grew at an average rate of approximately 2.4% per year, further amplifying global temperatures and intensifying climatic changes. Projections from the most recent models under the Coupled Model Inter-comparison Project Phase 6 (CMIP6) scenarios (e.g., SSP2-4.5 and SSP5-8.5) suggest that the negative effects of climate change on freshwater ecosystems and their availability will be more pronounced by the mid and late 21st century. These models, which build upon advanced numerical coupling across Earth systems (atmosphere, hydrosphere, cryosphere, and biosphere), provide higher-resolution simulations of climate patterns. Their applicability in simulating and projecting climate impacts is influenced by regional topography, climatology, and socioeconomic drivers.

Disturbances in the hydrological cycle, fueled by rising temperatures, shifting precipitation patterns, and increased variability, are projected to exacerbate water-related risks. Recent CMIP6 datasets highlight that the frequency and intensity of extreme weather events—such as floods and droughts—will increase significantly. These changes are particularly concerning for regions like India, where existing vulnerabilities are amplified by shifting agricultural practices, over-exploitation of groundwater, inefficient water management, rapid urbanization, and industrial growth. The compounded impacts of climate change have already been observed in major river basins across India, with discernible alterations at both the continental and local scales. The hydrological challenges India faces—ranging from irregular monsoon patterns to the overuse of groundwater resources—underscore the need for urgent, integrated water management strategies. While floods and droughts have long been natural occurrences, the increased unpredictability and severity due to climate change demand immediate attention. These impacts have far-reaching implications for agriculture, drinking water supply, and ecosystem health. Given these challenges, assessing water resource availability in light of 21st-century climate projections is critical for shaping long-term national and regional development strategies. Sustainable development in India's water resources sector will depend on incorporating climate resilience into planning, leveraging advanced climate modeling tools, and adopting adaptive management practices to mitigate the growing risks of climate change.

3.2 Selection of the Best CMIP6 Model Based on Historical Performance

3.2.1 Overview of dataset used for climatic projections

The NEX-GDDP-CMIP6 (NASA Earth Exchange Global Daily Downscaled Projections based on the Coupled Model Intercomparison Project Phase 6) dataset was used for future climatic projections in this study. It consists of globally downscaled climate scenarios based on General Circulation Model (GCM) simulations conducted as part of the Coupled Model Intercomparison Project Phase 6 (CMIP6) [Eyring et al., 2016]. These simulations encompass the four "Tier 1" greenhouse gas emission scenarios referred to as Shared Socioeconomic Pathways (SSPs) [O'Neill et al., 2016; Meinshausen et al., 2020]. CMIP6 GCM outputs were developed to support the Sixth Assessment Report of the Intergovernmental Panel on Climate Change (IPCC AR6). This dataset includes downscaled projections from ScenarioMIP model simulations [O'Neill et al., 2016; Tebaldi et al., 2021], with daily projections distributed via the Earth System Grid Federation. The primary aim of this dataset is to offer global, high-resolution, bias-corrected climate projections that facilitate the assessment of climate change impacts on processes influenced by finer-scale climatic variations and local topographic effects.

The need for GCM output downscaling arises due to two main limitations of current global simulations. First, many GCMs employ coarse spatial resolutions (e.g., grids of several degrees or approximately 102 km), which restrict their capacity to depict detailed climate patterns essential for regional or local analysis. Second, while GCMs may provide globally reliable projections, they often exhibit localized biases in their statistical properties (e.g., mean and variance) when compared to observational data.

To address these challenges, the NEX-GDDP-CMIP6 dataset was generated using the Bias-Correction Spatial Disaggregation (BCSD) method, a statistical downscaling technique (Wood et al., 2002; Wood et al., 2004; Maurer et al., 2008; Thrasher et al., 2012). This method adjusts GCM outputs by comparing them with observed climate data over a common reference period. The derived adjustments are then applied to future projections, enhancing consistency with historical records and improving realism for specific spatial domains. Additionally, the method incorporates spatial details from observational datasets to interpolate GCM outputs onto finer-resolution grids.

3.2.1.1 Datasets used for generation of NEX-GDDP-CMIP6

The generation of the CMIP6 dataset involves the integration of outputs from climate models and observational datasets to create a comprehensive resource for climate projections. The primary climate model data were sourced from thirty-five General Circulation Models (GCMs) included in the CMIP6 project. These models encompass the historical experiment as well as four future climate scenarios known as Shared Socioeconomic Pathways (SSPs): SSP1-2.6 (low emissions), SSP2-4.5 (moderate emissions), SSP3-7.0 (high emissions), and SSP5-8.5 (extreme emissions). The data span two key periods: the retrospective simulation from 1950 to 2014, representing historical conditions, and the prospective simulation from 2015 to 2100, projecting future climate conditions. Daily average variables such as temperature, precipitation, humidity, radiation, and wind speed were included in the dataset. The retrospective simulations served as the training data and were compared against observational climate records to establish relationships that could then be used to downscale the prospective projections. To ensure consistency, all projections underwent the same downscaling procedures, and the resulting outputs are collectively referred to as "GCM data" without distinguishing between individual models.

In addition to the climate model outputs, observational data were incorporated from the Global Meteorological Forcing Dataset (GMFD) for Land Surface Modeling, developed by the Terrestrial Hydrology Research Group at Princeton University. This dataset blends reanalysis data with observations to provide accurate climate records. It is available at multiple spatial resolutions (0.25 degrees, 0.5 degrees, and 1.0 degree) and temporal resolutions (3-hourly, daily, and monthly). For the development of the CMIP6 dataset, historical daily-averaged data at 0.25-degree resolution were utilized for the period from 1960 to 2014. Key variables from this dataset included maximum and minimum temperature, precipitation, near-surface humidity, downwelling shortwave and longwave radiation, and near-surface wind speed. These observational records provided the baseline for validating and training the downscaling process.

The downscaling process involved comparing the retrospective simulations from CMIP6 models with the observational data to derive statistical relationships. These relationships were then applied to the prospective projections, enabling the creation of high-resolution climate projections. By maintaining a consistent downscaling methodology across all models, the CMIP6 dataset provides reliable and uniformly processed data for studying past, present, and future climate scenarios. This comprehensive dataset is invaluable for advancing climate research and supporting informed decision-making in the face of global climate challenges.

3.2.1.2 Bias correction

The bias correction process is a crucial step in ensuring the reliability of climate model projections. This process adjusts biases in the General Circulation Model (GCM) data by comparing them against historical observational data, specifically the Global Meteorological Forcing Dataset (GMFD). For each climate variable on a given day, the algorithm generates cumulative distribution functions (CDFs) for both the GMFD data and the retrospective GCM simulations. This is done by pooling and sorting values from the same day of the year, including a 15-day window on either side, for the period from 1960 to 2014.

The algorithm then compares the CDFs of the two datasets at various probability thresholds to establish a quantile mapping relationship. This mapping enables the translation of GCM values in a specific quantile (for example, the 90th percentile) to their corresponding GMFD values in the same quantile. Assuming that the CDF of the GCM simulations remains stable across both retrospective and prospective periods, this relationship is used to adjust future climate projections. For projected values, the algorithm identifies the associated probability quantile from the GCM CDF and maps it to the equivalent value in the GMFD CDF, producing adjusted climate predictions.

The adjusted projections align with the statistical structure of the GMFD data, ensuring that any biases in the variance or other statistical attributes of the original GCM outputs are corrected. This process also preserves the original temperature trends extracted from the GCM data, which are added back to the adjusted climate fields at the end of the bias correction. As a result, the corrected climate projections provide a more reliable and accurate representation of future climate conditions, suitable for research and decision-making.

3.2.1.3 Spatial Disaggregation (SD)

The Spatial-Disaggregation (SD) process involves interpolating Adjusted GCM data to align with the finer resolution of the 0.25-degree GMFD grid. Instead of relying solely on linear interpolation, the SD algorithm employs multiple steps to maintain the spatial characteristics of observational data. Initially, a smoothed daily climatology is created from gridded observations for the 1960–2014 reference period using a Fast Fourier Transform, preserving three harmonics at both native and GCM resolutions. Next, for each time step, the algorithm determines "scaling factors" by comparing bias-corrected GCM variables with corresponding GMFD climatology. These scaling factors are computed as differences for temperature and as quotients for other variables to prevent negative values. Subsequently, the coarse-resolution scaling factors undergo bilinear interpolation to match the fine-resolution GMFD grid. Finally, the scaling factors are applied to the GMFD climatologies—using addition or shifting for temperature and multiplication for other variables—to generate downscaled climate fields. This approach integrates observed spatial climatology with GCM-simulated temporal changes, producing the final outputs.

3.2.2 Precipitation

To evaluate the historical precipitation data (1984–2014) for the IGNP region, daily, monthly and yearly precipitation values were plotted for different CMIP6 (Coupled Model Intercomparison Project Phase 6) models. The evaluation considered 12 models: ACCESS-ESM1-5, BCC-CSM2-MR, CanESM5, EC-Earth3, EC-Earth3-Veg-LR, INM-CM4-8, INM-CM5-0, MPI-ESM1-2-HR, MPI-ESM1-2-LR, MRI-ESM2-0, NorESM2-LM, and NorESM2-MM. Each model represents a unique simulation approach for precipitation and climate dynamics. The models vary in their parameterization schemes, and sensitivity to climatic variables, allowing for a diverse set of predictions. This diversity provides insights into the robustness and reliability of the simulated precipitation patterns when compared to observed IMD data. The analysis was carried out for multiple subregions: top, middle, bottom, east, west, north, and south. Each subregion was represented by a unique point and the performance of models was compared across these points. IMD observations served as the reference data for validating the models. The plotting process involved organizing daily, monthly and yearly precipitation data from CMIP6 models and IMD observations. Each model's data was extracted for all subregions to ensure comprehensive spatial coverage. Line plots were created to represent yearly trends for each mode. The visual consistency of models with IMD data was examined. Key observations included the variability, alignment with trends, and extreme deviations in precipitation values. **Figures 3.1 to 3.4** show the precipitation values and distribution of various climate models.

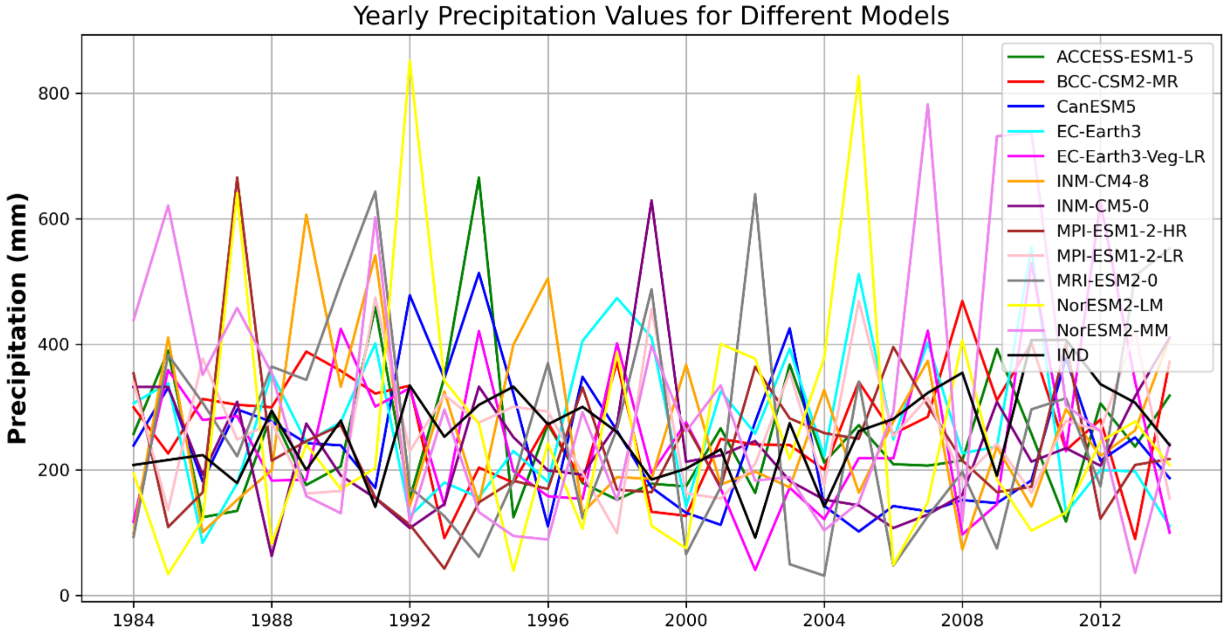

Figure – 3.1: Yearly precipitation values for different CMIP6 models in IGNP region from 1984-2014.

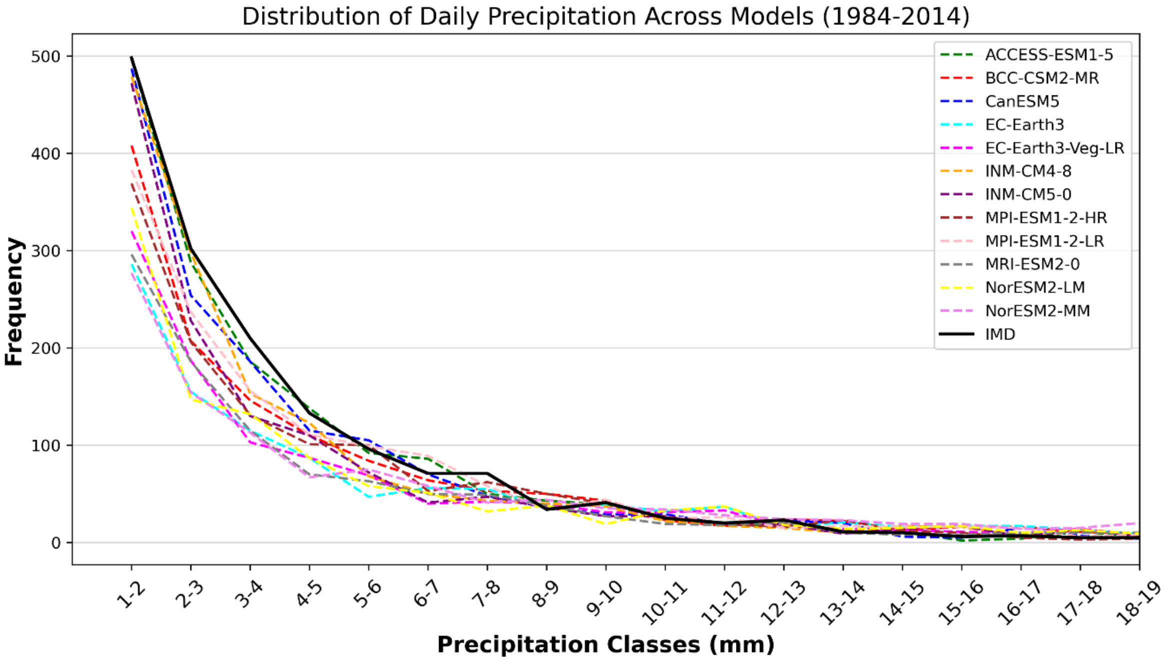

Figure – 3.2: Distribution of daily precipitation values for different CMIP6 models in IGNP region from 1984-2014.

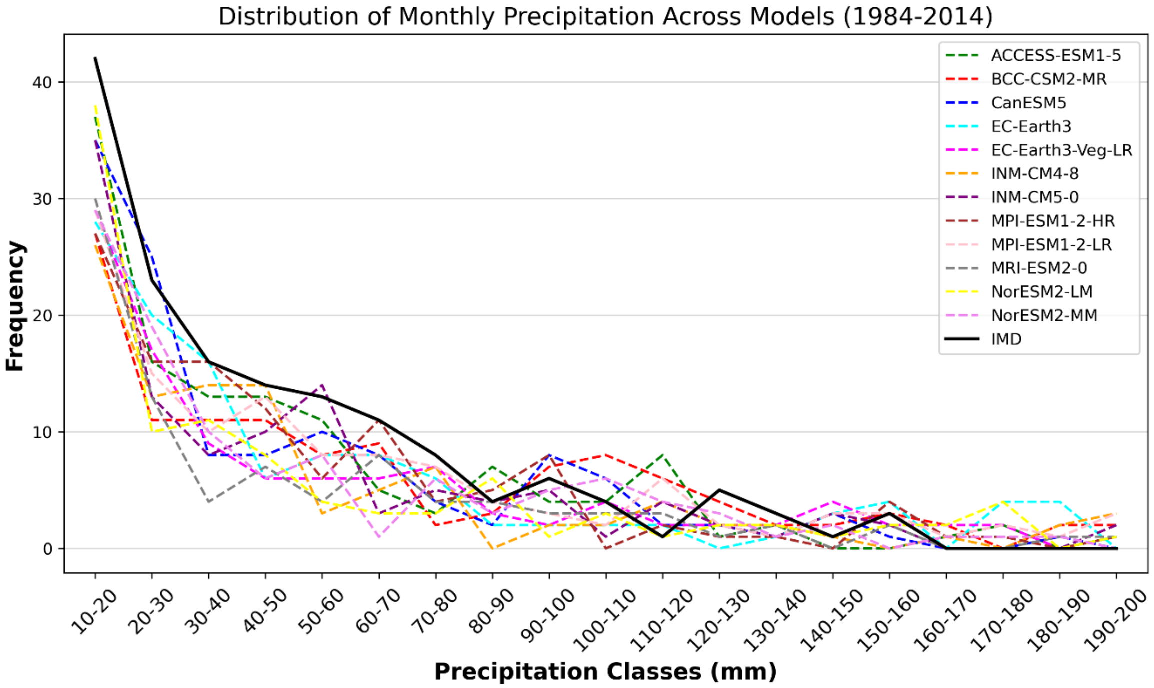

Figure – 3.3: Distribution of monthly precipitation values for different CMIP6 models in IGNP region from 1984-2014.

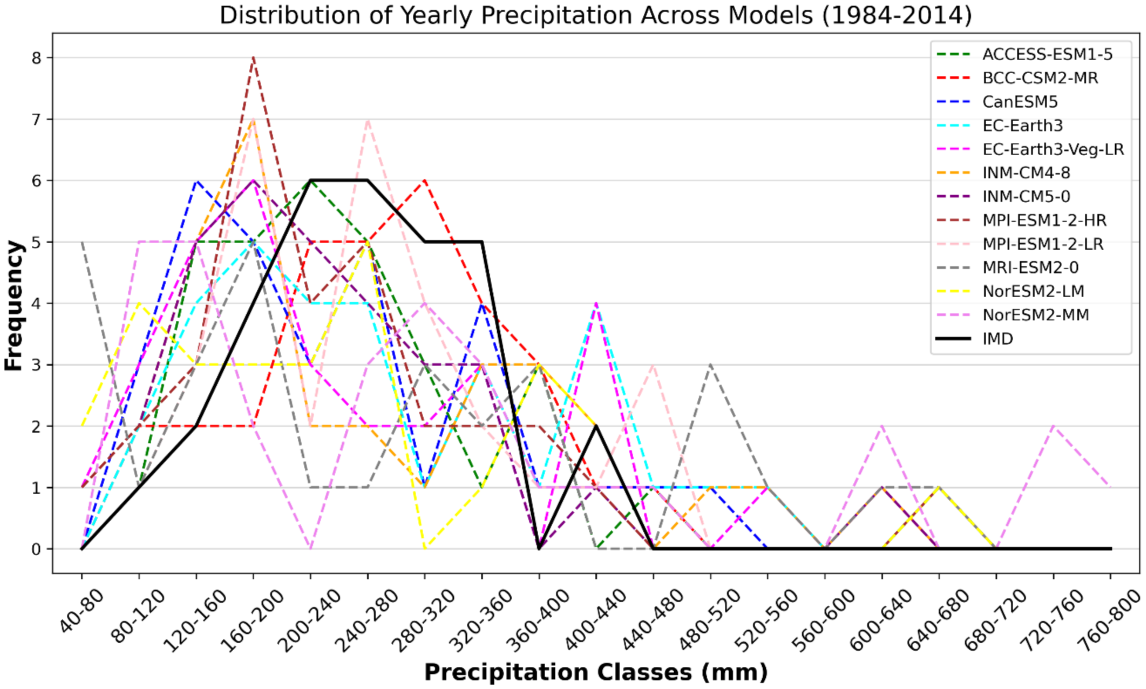

Figure – 3.4: Distribution of yearly precipitation values for different CMIP6 models in IGNP region from 1984-2014.

In addition to visual analysis, statistical parameters were computed to quantify model performance. These parameters were analysed for overall precipitation performance and average performance across subregions. The key metrics included Bias and Relative Bias to evaluate the degree of overestimation or underestimation by the models; Root Mean Square Error (RMSE) and Mean Absolute Error (MAE) to measure the magnitude of deviations from IMD observations; correlation with IMD to assess the linear relationship between model predictions and observed data; variance to quantify the variability in model predictions compared to IMD data; and Nash-Sutcliffe Efficiency (NSE) to determine the models' ability to replicate observed patterns.

Visual observations of the plots were done on the basis of consistency across subregions. Models with consistent trends across subregions were considered reliable. Extreme variability indicated lower reliability and models closely following IMD trends were deemed more accurate. On the basis of visual performance CanESM5 exhibited stable performance with good alignment to IMD trends across multiple subregions. INM-CM5-0 and ACCESS-ESM1-5 showed reasonable performance but with slight overestimations in some subregions.

Statistical evaluation of different models shows that CanESM5 has low RMSE and MAE, indicating smaller deviations from IMD observations (**Table 3.1**). It also exhibits minimal bias, showing accurate predictions and shows balanced performance across all metrics.

Table – 3.1

Statistical performance of precipitation values for various CMIP6 models for IGNP region

Rank	Model	Bias	Relative Bias (%)	RMSE	MAE	Correlation with IMD	Variance	Nash-Sutcliffe Efficiency (NSE)
1	ACCESS-ESM1-5	-0.02	-2.58	3.14	1.06	0.15	6.14	-0.79
2	MPI-ESM1-2-LR	0.01	1.48	3.19	1.08	0.16	6.55	-0.85
3	CanESM5	-0.05	-6.49	3.02	1.06	0.14	5.08	-0.66
4	INM-CM5-0	-0.07	-10.03	3.14	1.06	0.14	5.93	-0.8
5	INM-CM4-8	0.01	1.67	3.42	1.13	0.09	7.37	-1.12
6	EC-Earth3-Veg-LR	-0.02	-2.35	3.57	1.12	0.13	9.05	-1.32
7	BCC-CSM2-MR	0.03	4.29	3.45	1.14	0.14	8.23	-1.16
8	NorESM2-LM	0	0.45	3.61	1.16	0.11	9.13	-1.37
9	MPI-ESM1-2-HR	-0.06	-9.14	3.24	1.09	0.1	6.24	-0.92
10	EC-Earth3	0.04	5.9	3.68	1.2	0.12	9.83	-1.47
11	MRI-ESM2-0	0.02	2.52	3.97	1.19	0.08	11.57	-1.87
12	NorESM2-MM	0.12	17.13	3.95	1.27	0.13	12.18	-1.84

ACCESS-ESM1-5 shows moderate RMSE and MAE, with minimal overestimation. It shows consistent variance and good NSE values, indicating reliable pattern replication. INM-CM5-0 shows slightly higher RMSE but stable performance across subregions. It has lower bias and better correlation compared to other models. MPI-ESM1-2-LR shows high correlation with IMD but larger variability, making it less consistent.

Based on the combined analysis of plots and statistical parameters, CanESM5 emerged as the most reliable model for the IGNP region due to its low errors, minimal bias, and strong correlation with IMD observations. ACCESS-ESM1-5 and INM-CM5-0 were identified as robust alternatives, demonstrating consistent performance across subregions and metrics.

3.2.3 Maximum Temperature

For identifying the best performing CMIP6 model for maximum temperature historical maximum temperature data (1984–2014) for the IGNP region, daily, monthly and yearly precipitation values were plotted for different CMIP6 (Coupled Model Intercomparison Project Phase 6) models. The analysis was carried out for multiple points in the IGNP area. A total of 10 points were taken in different parts of the study area to take into account varying climatic conditions in the area. Visual performance and statistical performance of the models was carried out using the same method used for precipitation data. Based on the graphical representation and statistical metrics provided, it is clear that certain models perform better in capturing the maximum temperature trends when compared to others. Among these, the NorESM2-MM model emerges as the most reliable and accurate in reflecting the observed data trends from the Indian Meteorological

Department (IMD). A closer look at the performance metrics highlights the strengths of NorESM2-MM. With a Bias of 0.09 and a Relative Bias of 0.27%, it demonstrates minimal deviation from the observed data. The Root Mean Square Error (RMSE) of 3.42 and Mean Absolute Error (MAE) of 2.69 are also relatively low, indicating its precision in predicting maximum temperature values. Furthermore, the correlation coefficient of 0.86 with IMD data underscores its strong alignment with observed trends. This high level of correlation suggests that the model effectively captures inter-annual variability in maximum temperatures for the IGNP region.

Another key metric, the Nash-Sutcliffe Efficiency (NSE), provides a measure of how well the model's predictions align with observed data relative to the mean of the observations. NorESM2-MM achieves an NSE of 0.71, which is among the highest values recorded across all the models. This further reinforces its reliability in replicating temperature dynamics. The model's variance score of 42.52 demonstrates that it captures the spread of temperature values effectively without overestimating or underestimating extremes.

In addition to the individual metric performance, the ranking system provides an aggregate view of the models' performance across all statistical measures. NorESM2-MM consistently ranks in the top tiers across metrics, securing an overall rank of 24.0. This comprehensive evaluation solidifies its standing as a dependable model for studying maximum temperature patterns in the IGNP region.

Comparatively, other models like MRI-ESM2-0 and INM-CM5-0 also show strong performance but fall slightly behind NorESM2-MM in certain metrics. For example, while MRI-ESM2-0 has a similarly high correlation coefficient of 0.86 and comparable RMSE and MAE values, its overall rank of 31.0 places it below NorESM2-MM. INM-CM5-0, despite having a higher NSE of 0.72, exhibits slightly higher Bias and Relative Bias values, impacting its overall reliability.

The visual representation of yearly maximum temperature trends further corroborates these findings. NorESM2-MM exhibits patterns that closely follow the observed IMD data, with minimal divergence in extreme years. This visual consistency, combined with its strong statistical performance, makes it the preferred model for maximum temperature analysis in the IGNP region.

In conclusion, the NorESM2-MM model stands out as the best-performing model for representing maximum temperature trends in the IGNP region. Its low error metrics, high correlation with IMD data, and strong rankings across key statistical measures demonstrate its robustness and reliability.

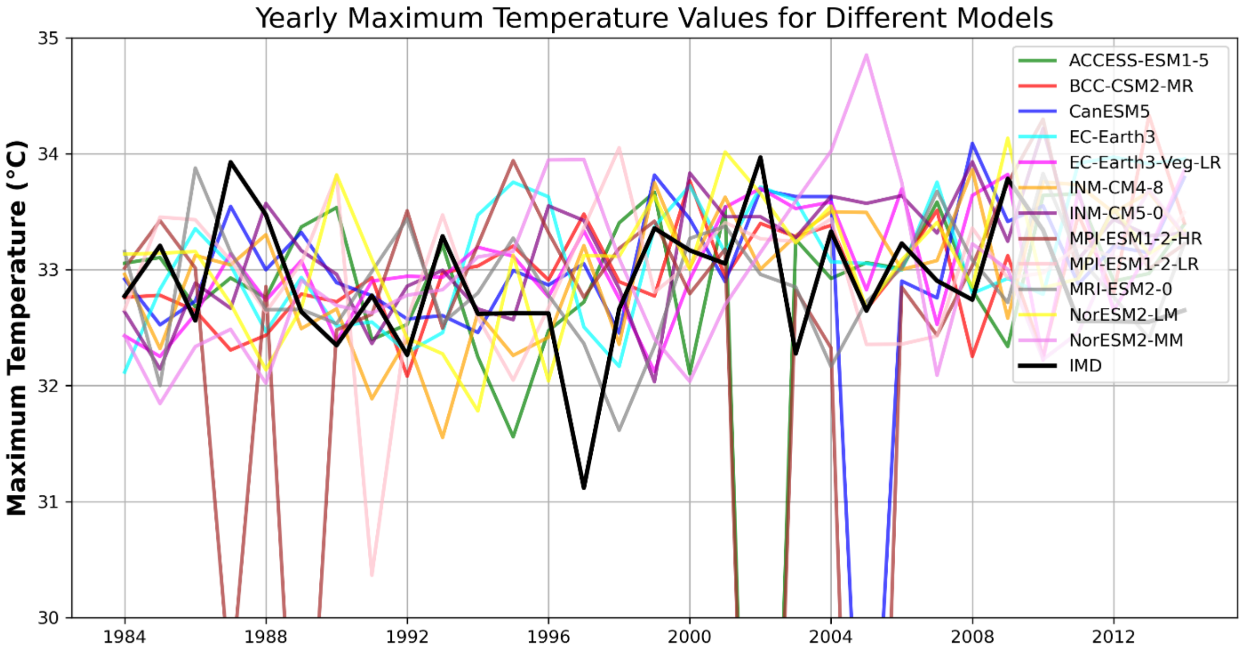

Figure – 3.5: Yearly maximum temperature values for different CMIP6 models in IGNP region from 1984-2014.

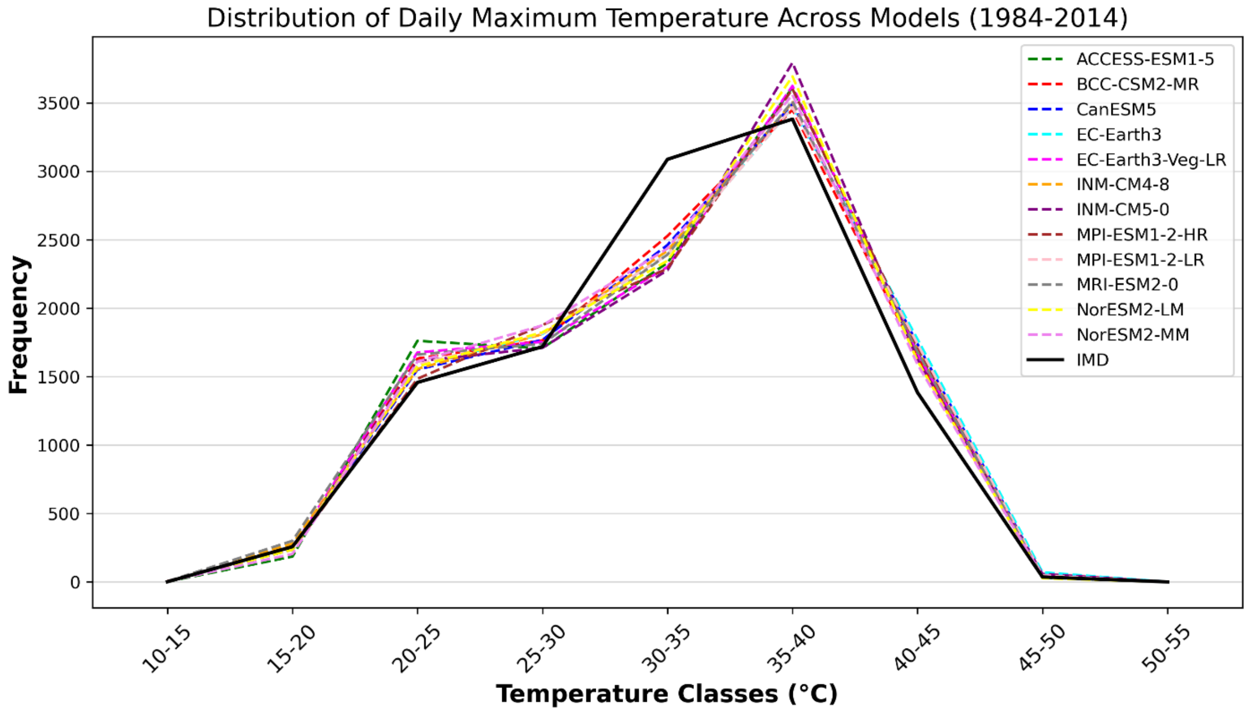

Figure – 3.6: Distribution of daily maximum temperature values for different CMIP6 models in IGNP region from 1984-2014.

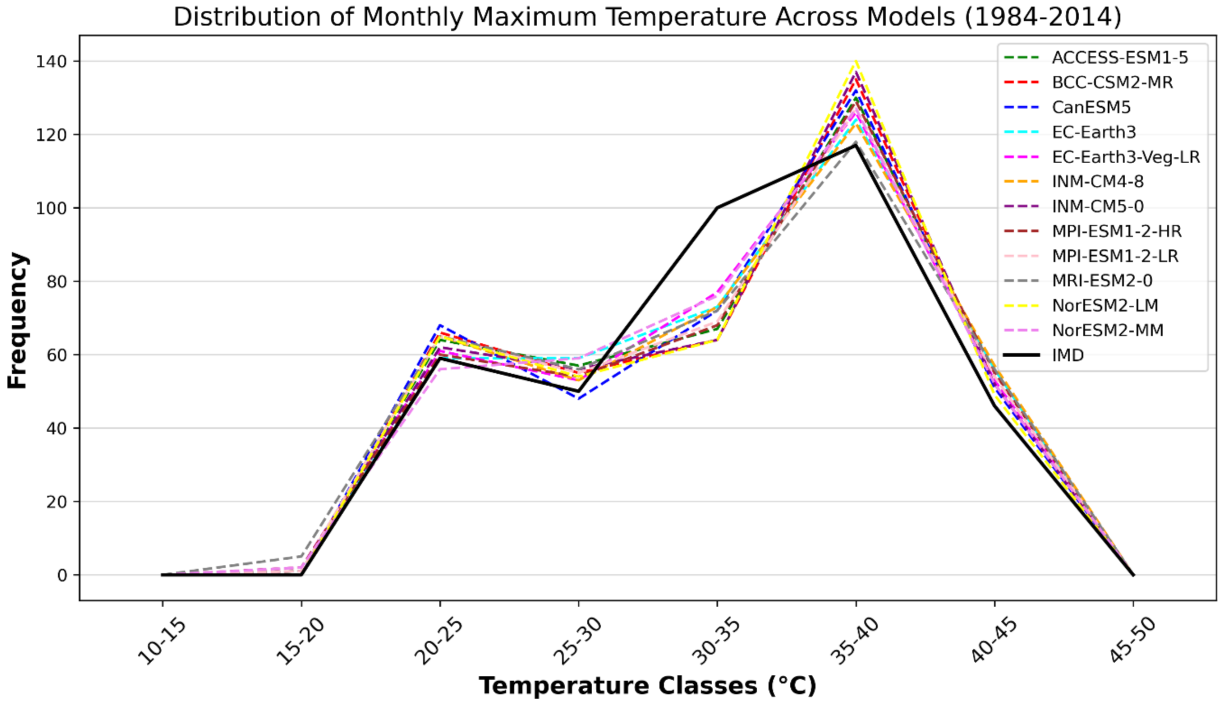

Figure – 3.7: Distribution of monthly maximum temperature values for different CMIP6 models in IGNP region from 1984-2014.

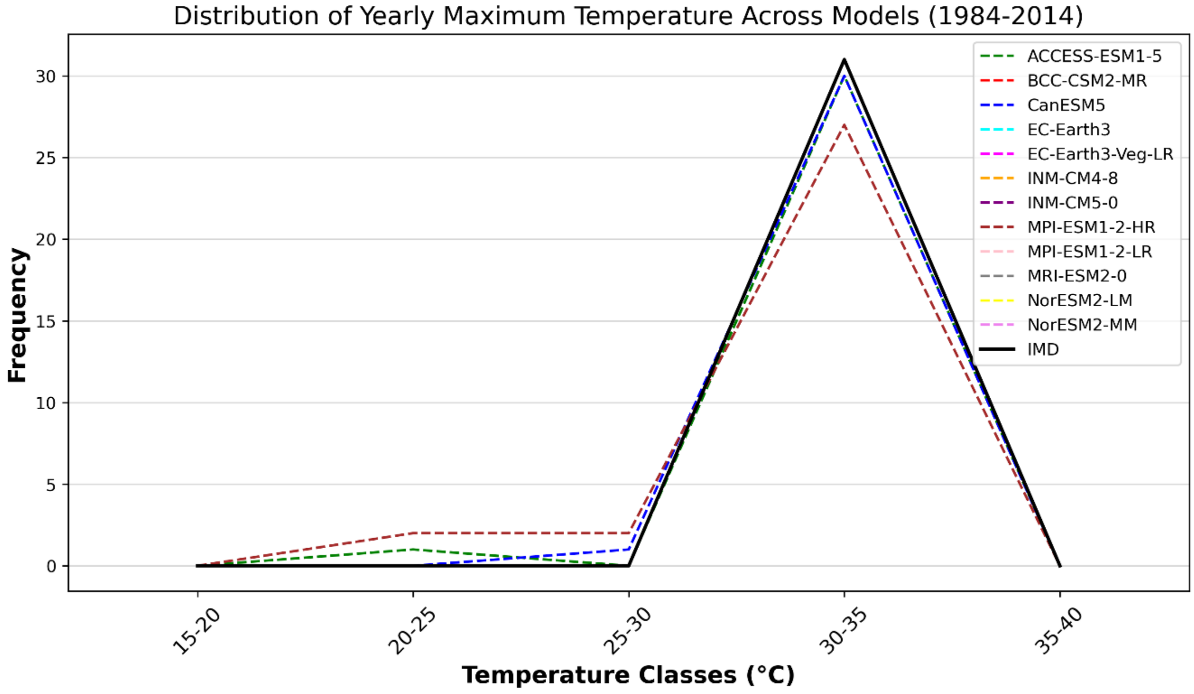

Figure – 3.8: Distribution of yearly maximum temperature values for different CMIP6 models in IGNP region from 1984-2014.

Table – 3.2

Statistical performance of maximum temperature values for various CMIP6 models for IGNP area

Rank	Model	Bias	Relative Bias (%)	RMSE	MAE	Correlation with IMD	Variance	Nash-Sutcliffe Efficiency (NSE)
1	NorESM2-MM	0.09	0.27	3.42	2.69	0.86	42.52	0.71
2	MRI-ESM2-0	0.01	0.03	3.44	2.72	0.86	45.23	0.7
3	NorESM2-LM	0.18	0.55	3.4	2.68	0.86	42.95	0.71
4	INM-CM5-0	0.29	0.88	3.35	2.64	0.87	44	0.72
5	BCC-CSM2-MR	0.11	0.32	3.48	2.73	0.86	44.15	0.7
6	INM-CM4-8	0.12	0.36	3.45	2.73	0.86	44.41	0.7
7	EC-Earth3-Veg-LR	0.16	0.49	3.48	2.74	0.86	44.97	0.7
8	EC-Earth3	0.25	0.76	3.48	2.74	0.86	44.56	0.7
9	MPI-ESM1-2-LR	0.09	0.27	3.81	2.76	0.84	48.43	0.64
10	CanESM5	0.06	0.17	6.63	2.82	0.67	80.28	-0.1
11	ACCESS-ESM1-5	-0.21	-0.63	9.43	2.8	0.55	127.36	-1.23
12	MPI-ESM1-2-HR	-0.7	-2.14	14.5	3.62	0.44	258.53	-4.27

3.2.4 Minimum Temperature

The evaluation of models for minimum temperature trends in the IGNP region highlights significant differences in their performance across key statistical metrics such as Bias, RMSE, Correlation with IMD, and Nash-Sutcliffe Efficiency (NSE). Among these models, MRI-ESM2-0 emerges as the most reliable and accurate for representing minimum temperature trends, closely followed by EC-Earth3-Veg-LR and MPI-ESM1-2-LR. These models consistently exhibit strong alignment with observed data and rank high across multiple performance indicators.

The MRI-ESM2-0 model stands out with a Bias of 0.04 and a Relative Bias of 0.22%, indicating the smallest deviation from observed IMD data. Its RMSE of 2.89 and MAE of 2.21 further demonstrate its precision in predicting minimum temperatures. The model's correlation coefficient of 0.94 with IMD data underscores its strong predictive capability, while an NSE value of 0.85 confirms its robustness in capturing inter-annual variability. With an overall rank of 28, MRI-ESM2-0 consistently outperforms other models in terms of accuracy and reliability.

EC-Earth3-Veg-LR also delivers strong performance, with a Bias of 0.14 and a Relative Bias of 0.76%. Its RMSE of 2.83 and MAE of 2.15 are among the lowest, making it highly competitive. Like MRI-ESM2-0, this model achieves a correlation coefficient of 0.94 and an NSE value of 0.86, highlighting its reliability in replicating minimum temperature trends. The model's overall rank of 29 reflects its consistency across all metrics, making it a close competitor to MRI-ESM2-0.

Similarly, MPI-ESM1-2-LR demonstrates strong alignment with observed data. With a Bias of 0.05 and a Relative Bias of 0.26%, it shows minimal deviation. Its RMSE of 2.88 and MAE of 2.17 are slightly higher than those of EC-Earth3-Veg-LR but still reflect high accuracy. The model's correlation coefficient of 0.94 and NSE value of 0.85 further establish its reliability, resulting in an overall rank of 29, tied with EC-Earth3-Veg-LR.

ACCESS-ESM1-5 also performs well, with a correlation coefficient of 0.94 and an NSE value of 0.87. However, its higher Bias (0.23) and Relative Bias (1.27%) slightly diminish its overall standing. CanESM5, while demonstrating good correlation (0.94) and variance, ranks slightly lower overall due to its RMSE and MAE values. On the other hand, models such as BCC-CSM2-MR and INM-CM5-0 perform poorly, with high RMSE and significantly lower correlation values. INM-CM5-0, in particular, exhibits extreme deviations, with a high Bias (-5.31) and an NSE of -20.75, rendering it unreliable for minimum temperature analysis.

The graphical representation of yearly minimum temperature trends aligns with the statistical analysis. Models such as MRI-ESM2-0 and EC-Earth3-Veg-LR closely follow the observed IMD trend, with minimal deviations even during extreme years. This visual consistency corroborates their strong statistical performance and underscores their suitability for climate analysis in the IGNP region.

In conclusion, MRI-ESM2-0 emerges as the best-performing model for minimum temperature analysis in the IGNP region, offering accurate and consistent predictions. EC-Earth3-Veg-LR and MPI-ESM1-2-LR also demonstrate strong reliability and are viable alternatives.

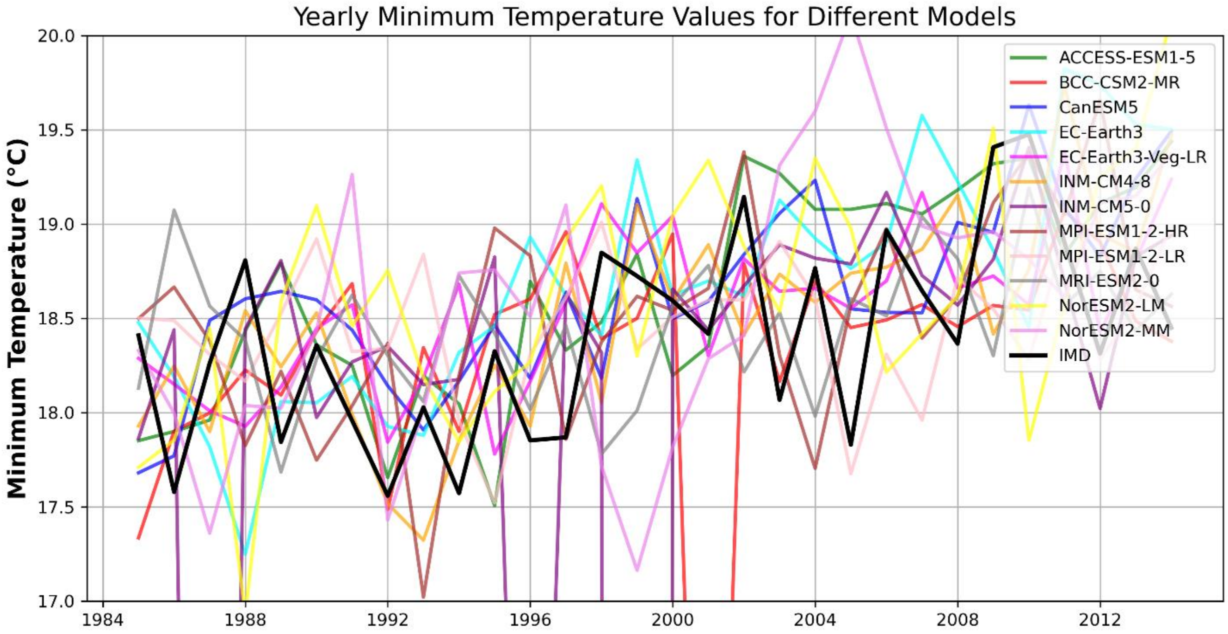

Figure – 3.9: Yearly minimum temperature values for different CMIP6 models in IGNP region from 1984-2014.

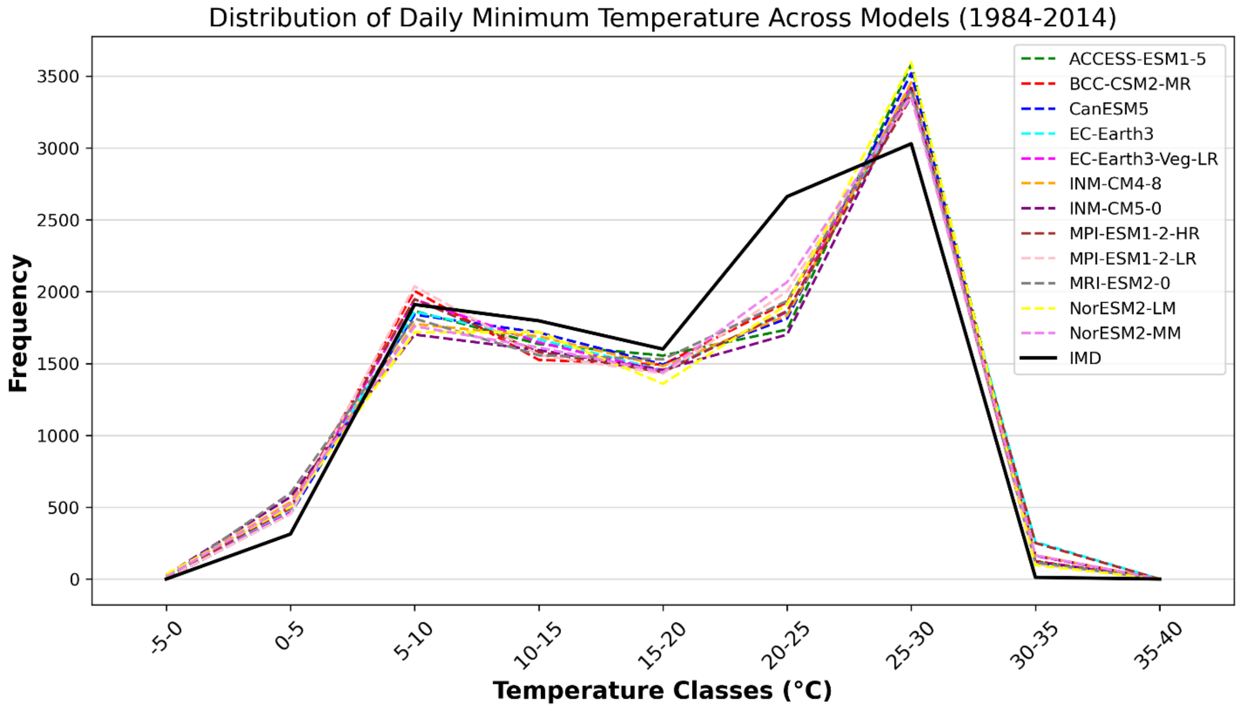

Figure – 3.10: Distribution of daily minimum temperature values for different CMIP6 models in IGNP region from 1984-2014.

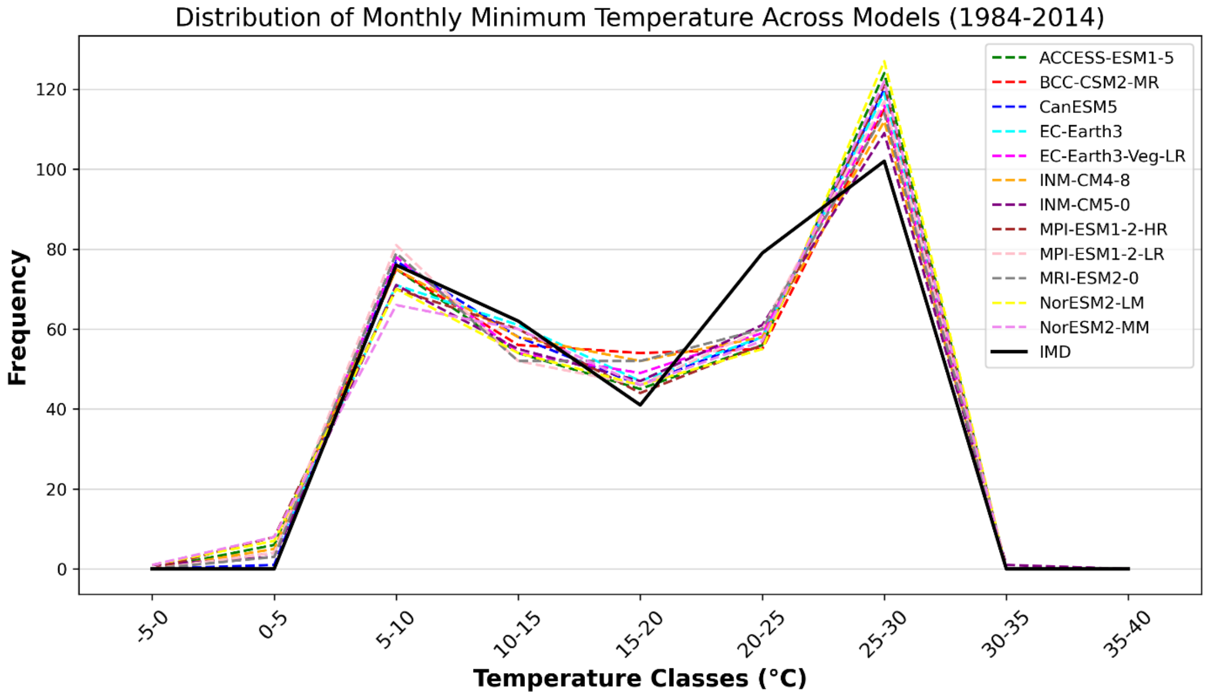

Figure – 3.11: Distribution of monthly minimum temperature values for different CMIP6 models in IGNP region from 1984-2014.

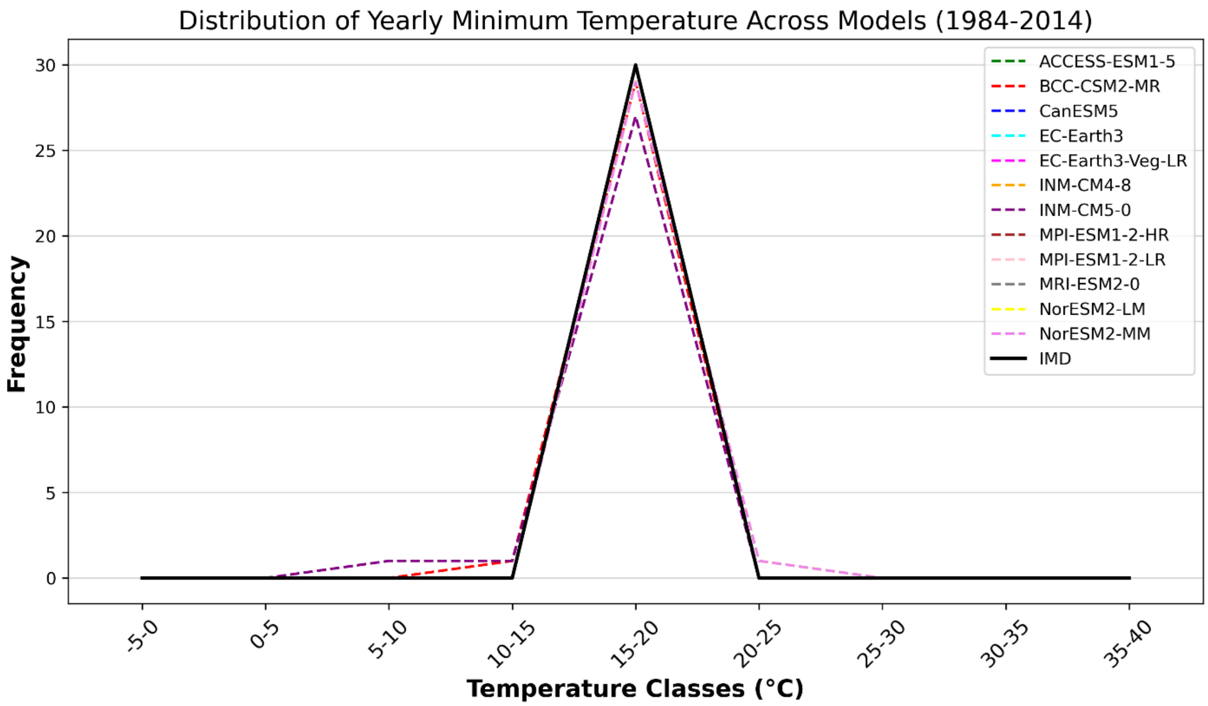

Figure – 3.12: Distribution of yearly minimum temperature values for different CMIP6 models in IGNP region from 1984-2014.

Table – 3.3

Statistical performance of minimum temperature values for various CMIP6 models for IGNP area

Rank	Model	Bias	Relative Bias (%)	RMSE	MAE	Correlation with IMD	Variance	Nash-Sutcliffe Efficiency (NSE)
1	MRI-ESM2-0	0.04	0.22	2.89	2.21	0.94	67.22	0.85
2	EC-Earth3-Veg-LR	0.14	0.76	2.83	2.15	0.94	66.99	0.86
3	MPI-ESM1-2-LR	0.05	0.26	2.88	2.17	0.94	67.27	0.85
4	ACCESS-ESM1-5	0.23	1.27	2.73	2.07	0.94	66.18	0.87
5	CanESM5	0.23	1.23	2.79	2.14	0.94	66.66	0.86
6	INM-CM4-8	0.09	0.51	2.97	2.21	0.93	67.92	0.85
7	NorESM2-MM	0.18	1	3.05	2.24	0.93	68.32	0.84
8	EC-Earth3	0.27	1.46	2.95	2.26	0.93	67.51	0.85
9	MPI-ESM1-2-HR	0.1	0.54	3.14	2.28	0.93	71.1	0.83
10	NorESM2-LM	0.21	1.16	3.08	2.25	0.93	69.21	0.83
11	BCC-CSM2-MR	-0.17	-0.94	5.11	2.31	0.84	88.41	0.54
12	INM-CM5-0	-5.31	-28.87	35.21	7.7	0.18	1253.18	-20.75

3.2.5 Selection of the Best CMIP6 Models for Future Climate Projections

The selection of the best CMIP6 models for future climate projections requires a thorough assessment of their historical performance in representing key climatic variables such as temperature and precipitation. The evaluation of these models was conducted using statistical metrics such as Bias, Root Mean Square Error (RMSE), Mean Absolute Error (MAE), Correlation with IMD data, and Nash-Sutcliffe Efficiency (NSE). Based on these metrics and visual consistency with observed data, CanESM5 was selected for minimum temperature and precipitation, while NorESM2-LM was chosen for maximum temperature. The selection of these models ensures a balance between accuracy, reliability, and predictive capability for future climate analysis.

For minimum temperature, CanESM5 exhibited strong alignment with observed data while maintaining minimal bias and lower errors compared to other models. The statistical evaluation showed that CanESM5 had a low RMSE and MAE, signifying reduced deviations from the IMD observations. Moreover, the model demonstrated balanced performance across different subregions, reinforcing its reliability. The variance and NSE values indicated that CanESM5 was able to replicate historical trends effectively, making it a robust choice for minimum temperature projections. While MRI-ESM2-0 and EC-Earth3-Veg-LR also showed competitive performance, CanESM5 was selected due to its consistent ranking across multiple statistical measures and its ability to capture regional climatic variations effectively.

In terms of precipitation, CanESM5 was selected based on its strong statistical performance and agreement with observed IMD trends. The model demonstrated stable performance across multiple subregions and exhibited minimal bias in precipitation estimation. The evaluation of yearly, monthly, and daily precipitation values revealed that CanESM5 closely followed observed trends with minimal overestimation or underestimation. The RMSE and MAE values were among the lowest, confirming the model's ability to capture precipitation variability accurately. Furthermore, the Nash-Sutcliffe Efficiency (NSE) values suggested that CanESM5 was effective in replicating the observed patterns, making it the most suitable model for future precipitation projections.

For maximum temperature, NorESM2-LM emerged as the best-performing model due to its strong correlation with IMD data and superior ranking across multiple statistical metrics. The model exhibited minimal bias, low RMSE, and MAE values, confirming its accuracy in predicting maximum temperature trends. A key strength of NorESM2-LM was its high correlation coefficient, indicating that it captured inter-annual temperature variability effectively. Additionally, the NSE values suggested that the model was capable of replicating observed temperature patterns with high reliability. Among other models, NorESM2-MM and MRI-ESM2-0 also performed well, but NorESM2-LM's consistency across different metrics and its ability to capture regional climatic trends made it the preferred choice for maximum temperature projections.

The selection of these models is critical for ensuring robust climate projections that can be effectively integrated into impact assessments and adaptation planning. Given the increasing variability in temperature and precipitation due to climate change, it is essential to rely on models that have demonstrated high accuracy in historical simulations. The use of CanESM5 for minimum temperature and precipitation, along with NorESM2-LM for maximum temperature, provides a reliable framework for assessing future climate scenarios in the study region. These selections not only enhance the credibility of climate projections but also support the development of sustainable water resource management strategies in the face of changing climatic conditions.

* * *

CHAPTER – 4

IDENTIFICATION OF SURFACE PONDING

4.1 Overview

Indira Gandhi Nahar Pariyojana (IGNP) represents a remarkable endeavour towards irrigation aimed at converting arid regions in Rajasthan's Thar Desert into productive agricultural land. Initiated in the late 1950's, it is one of the largest canals globally and occupies the north-western and far western parts of the Thar Desert. Its goals are multifaceted and include relief from droughts, provision of clean drinking water, environmental protection, livestock production promotion, and a substantial increase in agricultural output. Hence, it has become an important source of irrigation for the region, converting once barren lands into productive agricultural fields through its canals. However, some areas within the command area of IGNP have encountered the development of waterlogging, which negatively affects the health of the crops, thereby rendering the land unsuitable for agricultural purposes. Thus, there is a need to identify and apply effective water management strategies to reduce waterlogged areas in the canal command area.

Remote sensing is an important and efficient tool, particularly in the agricultural sector, for the effective identification of waterlogged sites. The remote sensing technologies widely used include satellite remote sensing, which uses various techniques like the deployment of multispectral sensors and calculation of indices such as Normalized Difference Vegetation Indexes (NDVI) and Normalized Difference Water Indexes (NDWI) that play a key role in delineating waterlogged areas. These indices facilitate the development of detailed risk maps that highlight perennial and permanent waterlogged sites. Additionally, remote sensing helps in the analysis of changes in vegetation indices like the Enhanced Vegetation Index (EVI) or Normalized Difference Vegetation Index (NDVI) that can be used to track waterlogged croplands over time. Such constant monitoring provides timely information for agricultural decision-making, including crop selection and land management strategies. Moreover, improvements in the quality and resolution of Digital Elevation Models (DEM) combined with optical satellite data significantly improve the accuracy of waterlogging studies through an integrated approach. This integration of remote sensing data allows for better management of irrigation systems and helps in mitigating the risks associated with waterlogging by adopting appropriate water management practices (den Besten et al., 2021).

The use of remote sensing data provided by Landsat missions has proven to provide vital insights into the identification and monitoring of water bodies. Landsat images offer a spatial resolution of 30 metres; thus, the resolution is suitable for the definition and continuous observation of water bodies. The satellites' ability to revisit any given area more often increases their usefulness in terms of change detection over time.

Since 1984, Landsat datasets have been available continuously, making them an excellent dataset for studying water bodies' variations, thereby helping scientists and hydrologists understand and document hydrological shifts and trends. Such long-term data continuity would allow for reliable analysis of waterbodies' changes using Landsat, making these datasets a preferred choice among many scientists and analysts focused on hydrological studies. However, handling vast volumes of satellite data is computationally demanding because these collections are complex and have huge sizes. For instance, when satellite images are acquired over large extents and at high-resolution levels, they create petabytes of data that must be processed efficiently using advanced computer systems. High-performance computing environments are essential for handling image processing, data analysis, and storage tasks often featuring powerful CPUs and GPUs. They enable quick data processing by parallel computing methods thus allowing for real-time data feeding as well as quicker decision making. Additionally, cloud computing platforms are being increasingly used these days to provide adaptable resources that can be scaled according to the load, thereby making satellite data processing operations more flexible and efficient.

Access to high-performance computers has become relatively common and widespread nowadays, and cloud computing is now a common service as well, with supercomputers becoming increasingly available. With advances in data collection from different satellites, a lot of remote sensing data archives are also freely available online. Some of these archives consist of information from government institutions like NASA, USGS (the United States Geological Survey) or ESA (the European Space Agency). Various tools have also been created to process large amounts of geospatial data at once. Despite all these developments, due to the technical skills and effort required, it remains difficult to utilise data from the remote sensing archives quickly and efficiently. Data acquisition and storage are critical issues in basic IT management regarding these resources, besides dealing with complex file formats, databases, machine assignments, job queues, CPUs, GPUs, and network configurations and sorting through numerous geospatial data processing platforms. Consequently, these difficulties create entry barriers for many researchers since they may not have access to both highly specialised equipment for high performance computing as well as substantial expertise in remote sensing altogether. Google Earth Engine addresses this challenge by offering an easy-to-use cloud-based portal that allows the utilisation of supercomputers in processing extensive geospatial datasets, thereby circumventing the typical IT complications. Furthermore, unlike conventional supercomputer centres, Earth Engine has been designed as a tool for sharing findings with ease among scientists, policymakers, NGOs and other stakeholders, including field workers and ordinary citizens. Once users develop an algorithm on Earth Engine, they can generate useful data products or create interactive interfaces supported by Earth Engine's resources, all without needing expertise in application development, HTML or programming (Gorelick et al., 2017).

The Google Earth Engine (GEE) platform provides access to large sets of publicly available geospatial datasets (e.g., Landsat, Sentinel and MODIS) and also enables visualisation and advanced computational analysis processing of these datasets with an explorer web app that supports widely used coding languages, such as JavaScript and Python. This helps in lowering research costs by allowing users access to large amounts of data and providing computational power to perform advanced data processing on these datasets without needing access to supercomputers (Tamiminia et al., 2020). Also, it empowers the researchers from countries that are currently in the developing stage with less financial resources and computing infrastructure to carry out research at a level comparable to the researchers in prosperous and developed countries (Mutanga & Kumar, 2019).

Earth Engine has been and is being effectively used in a wide range of fields, including global forest monitoring (Hansen et al., 2013), global surface water dynamics (Pekel et al., 2016), and crop yield predictions (Lobell et al., 2015), among others. Gujrati & Jha, (2018) used GEE to access change in the surface water resources of mainland India using images from five consecutive years. Its applications also encompass urban development tracking (Zhang et al., 2015; Patel et al., 2015), flood detection (Coltin et al., 2016), assessment of fire recovery efforts (Soulard et al., 2016), and malaria risk analysis (Sturrock et al., 2014). Additionally, Earth Engine has been successfully integrated into miscellaneous platforms like examining species habitats (Map of Life, 2016), climate monitoring (Climate Engine, 2016), and land use changes (Collect Earth, 2016).

A convenient way of identifying water bodies from remote sensing images is by using threshold values of water indices (Wang et al., 2019). The most widely used water identification indices are the Normalized Difference Water Index (NDWI) (McFeeters, 1996), Modified NDWI (MNDWI) (Xu, 2006), and Automatic Water Extraction Index (AWEI) (Zhou et al., 2021). While NDWI and MNDWI have been applied extensively in water body identification, they have certain shortcomings. Finding appropriate threshold values for NDWI and MNDWI to classify all water pixels is difficult, especially for mixed pixels that contain vegetation hence affecting the accuracy of the water detection process. Though optimal threshold values can be obtained based on visual interpretation, it is a tedious process that may be subject to human judgment errors. Combining MNDWI with normalised difference vegetation index (NDVI) and enhanced vegetation index (EVI) will help identify water precisely from the satellite images. One good example is by Zou et al. (2018), who proposed an algorithm that identifies a pixel as water if ((MNDWI > NDVI or MNDWI > EVI) and (EVI < 0.1)). This algorithm has been extensively tested and proved to be quite efficient for water identification (Huang et al., 2021). Moreover, it has enhanced image classification efficiency by eliminating the need to set threshold values for each image.

4.2 Methodology

For this study, Landsat 5, 6 and 8 images for the command area from 1984 to 2023 were used (Landsat 5 was launched in 1984, but no images of the area were available from 1984 and 1985). Six spectral bands from collection-2 level-2 data in Google Earth Engine (GEE) were selected for the calculation of spectral indices for the identification of water. The spectral bands used are red, green, blue, Near-Infrared (NIR), and Short-Wave Infrared (SWIR1). A total of 8525 Landsat images were used for waterlogged areas identification, including 2086 Landsat 5 images from 1986-1998, 2717 Landsat 7 images from 1999 to 2012 and 3722 Landsat 8 images for 2013-2023. The Landsat images used in the study spanning different time periods is presented in **Figure 4.2**. The overall methodology is shown in **Figure 4.1**.

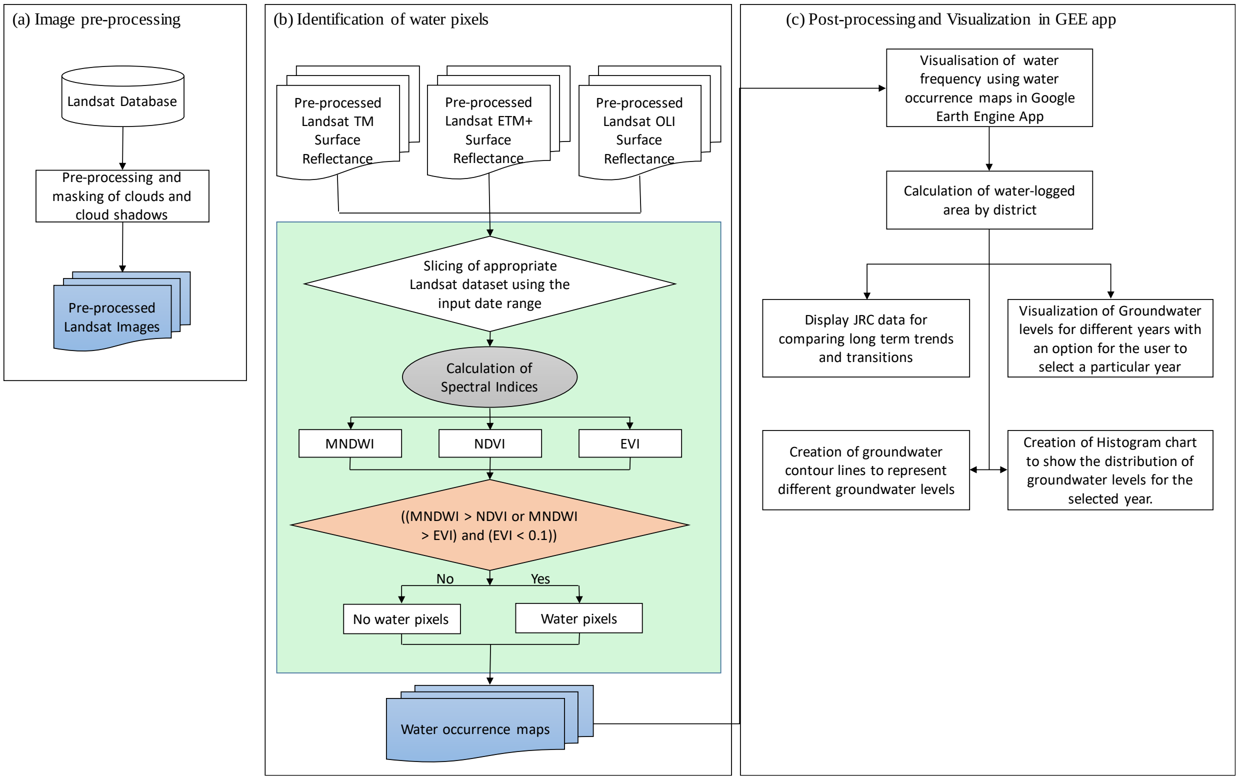

Figure – 4.1: Flowchart of the waterlogged area mapping using Landsat 5, 7 and 8 images and Google Earth Engine (GEE).

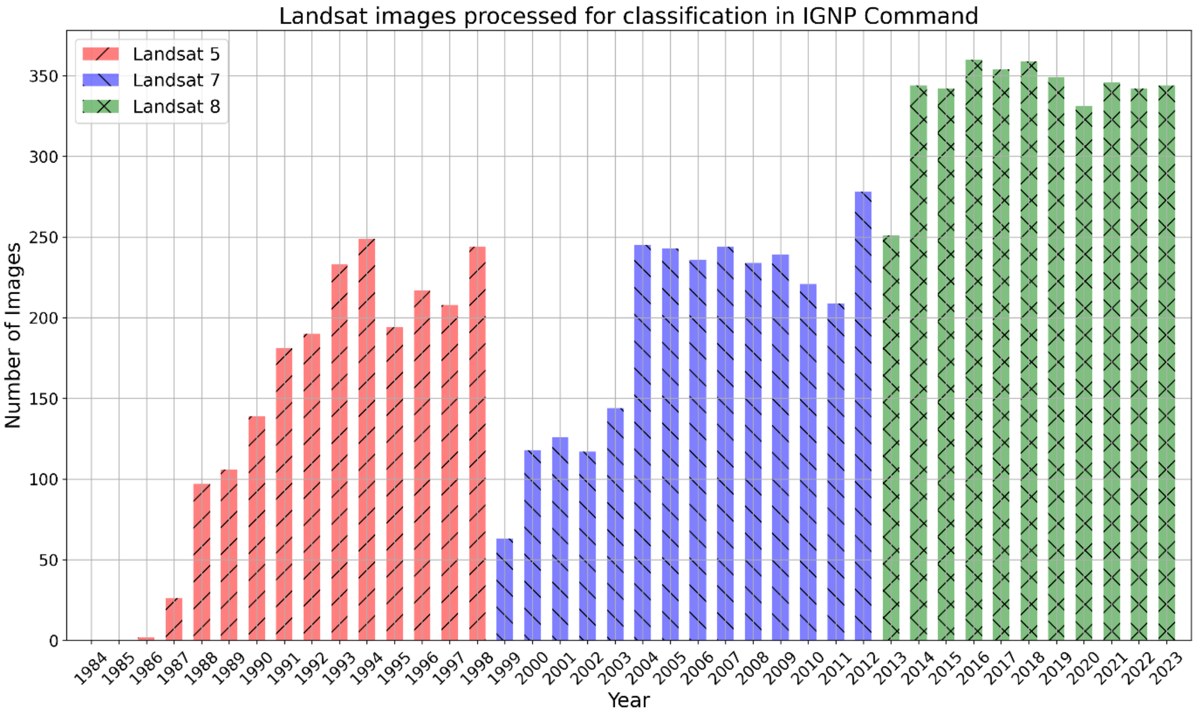

Figure – 4.2: Landsat Images Processed for Classification in IGNP Command

4.3 Image Pre-processing

In remote sensing data analysis, image pre-processing is an important step that involves various crucial activities to ensure that the data is fit for accurate and reliable analysis. For waterlogged areas, in order to keep track of changes precisely, it is imperative to acquire high-quality images so the water pixels can be calculated accurately. These images are then used to find how waterlogged areas changed over time. Each picture should show all parts of the waterlogged zone so as to give a complete picture while sometimes clouds obstruct vision in photographs, therefore requiring filtering technique for clarity. Therefore, an automatic pre-processing procedure was employed to select an image dataset that would fall within specific predetermined standards used for calculating water indexes. Furthermore, geographical coverage problems were resolved by overlapping each image with the designated waterlogged area. Pixels affected by clouds and cloud shadows are masked out. The Fmask (function of mask) algorithm was used to accomplish this task by employing an automated system that uses spectral, spatial and thermal characteristics of every pixel to detect clouds as well as water.

4.4 Calculation of Water Indices

The last few decades have seen extensive analysis of the use of water indices to detect surface water. The main concept involves the use of reflectance characteristics of objects in specific spectral ranges in optical images to differentiate various types of surface cover. This method has been very successful in distinguishing water from other types of land use and is used in many practices applicable to water resource assessment and management.

The NDWI McFeeters index, formulated by McFeeters in 1996 for Landsat 4 Multi-mission Modular Spacecraft (MSS) data, primarily applies to imagery with visible and NIR bands. Similar to the NDVI calculation described by McFeeters, (1996), this index helps in the identification of water by substituting the red band with the green band and changing the factor order. It raises the reflectance of water through green wavelengths, diminishes the reflectance of water in the NIR because of its low reflectance, and uses the relatively greater reflectance of plants and soil in the NIR to differentiate them from waterbodies (Condeça et al., 2022).

In 1996, another water index was introduced by Gao, named NDWI, which differentiates water in vegetated areas through two infrared spectrum channels, which are; 0.86 to 1.24 μm (wavelengths in both near and middle infrared radiation). According to Gao (1996), the spectral signature of green vegetation within the 0.9–2.5 μm range is highly influenced by water in terms of absorption yet minimally by other biochemical constituents. The NDWI is sensitive to the depth of the water in vegetation, generally showing positive values in such areas. However, soil also affects the NDWI values. Typical soil reflectance increases from 0.8 to 1.3 μm, and these soils do not exhibit water absorption in 0.98-1.2 μm bands, including very wet ones. As a result, most bare samples will give negative NDWI values because most do contain water. Consequently, NDWI values tend to be negative for most bare soils, although this index does not completely negate ground reflectance.

Xu (2006), found out that although NDWI developed by McFeeters, (1996) clearly highlighted water-bodies separately from vegetation or soil, it fails to adequately filter out signals from built-up areas, leading to overestimation of water bodies. To counter this effect, Xu (2006) introduced MNDWI, a modification of NDWI which substitutes the NIR band with the SWIR1 band, which minimizes urban noise while enhancing water detection accuracy. Nevertheless, despite their widespread use due to high precision in delineating water bodies, NDWI and MNDWI have two major limitations. The first limitation is that these indices require high sensitivity for correctly detecting water bodies in case there are mixed vegetation and water pixels in the image. Furthermore, finding suitable thresholds for both NDWI and MNDWI is crucial in determining the precision of water body extraction. However, this empirical method is prone to subjective biases, and ultimately, it is tedious.

An alternative method involves correlating MNDWI with the normalized difference vegetation index (NDVI) and the enhanced vegetation index (EVI) to extract water accurately from optical satellite data (Chen et al., 2020). To minimise the commission errors in the areas having both water and vegetation and other land use pixels, like vegetation pixels in waterbodies (Santoro et al., 2015) in MNDWI, Zou et al., (2018) introduced a new algorithm that combined MNDWI with the vegetation indices NDVI and EVI to minimise the effect of vegetation on water identification. Only areas with greater water probability than vegetation (MNDWI > NDVI or MNDWI > EVI) are classified as water pixels. To further refine the results and remove classification errors due to vegetation, EVI is used to remove the pixels of vegetation in water (EVI < 0.1). Thus, the algorithm defines water extraction criteria as ((MNDWI > NDVI or MNDWI > EVI) and (EVI < 0.1)), achieving notable success and accuracy in practical applications. The utility of this approach lies in its elimination of the need to individually threshold images. When the conditions were satisfied, a pixel was identified as water and labelled with a 1. Conversely, if the conditions were not met, the pixel was categorized as non-water and labelled 0. Water and vegetation indices such as the Modified Normalized Difference Water Index (MNDWI), Normalized Difference Vegetation Index (NDVI), and Enhanced Vegetation Index (EVI) utilized for mapping waterbodies were derived from cloud-free surface reflectance images from Landsat TM, ETM+, and OLI, using the following formulas on specific spectral bands:

$$MNDWI = \frac{\rho_{Green} - \rho_{SWIR1}}{\rho_{Green} + \rho_{SWIR1}} \tag{4.1}$$

$$NDVI = \frac{\rho_{NIR} - \rho_{Red}}{\rho_{NIR} + \rho_{Red}} \tag{4.2}$$

$$EVI = 2.5 \times \frac{\rho_{NIR} - \rho_{Red}}{\rho_{NIR} + 6 \times \rho_{Red} - 7.5 \times \rho_{Blue} + 1} \tag{4.3}$$

where ρ_{Red}, ρ_{Green}, ρ_{Blue}, ρ_{NIR}, and ρ_{SWIR1} are the red, green, blue, near-infrared, and short-wave infrared bands of Landsat images, respectively. For each Landsat pixel in the area of interest, the water frequency for a particular time period was calculated using the values of water detection in that time period. An application was developed in Google Earth Engine that lets the user define the time period for calculating water frequency. The app lets the user visualise the waterlogged areas in the IGNP study area and calculates the percentage of waterlogged areas in the different districts of the command area.

4.5 Accuracy Assessment

Evaluating the dependability of remote sensing-derived waterlogged area classifications necessitates an assessment of the precision. This assessment is essential for ensuring the classifications are reliable enough for practical applications and decision-making processes. Landsat data accuracy assessment involves tools such as confusion matrix, kappa coefficient, producer's accuracy, and user's accuracy for Thematic Mapper (TM), Enhanced Thematic Mapper Plus (ETM+), and Operational Land Imager (OLI) sensors. The confusion matrix is one of the fundamental elements in accuracy assessment which gives a detailed comparison between classified data (predicted classes) and reference data (true classes). In the context of water-logged area classification, the confusion matrix consists of: True Positives (TP): Pixels correctly identified as water-logged, True Negatives (TN): Pixels correctly identified as non-water-logged, False Positives (FP): Pixels incorrectly identified as water-logged and False Negatives (FN): Pixels incorrectly identified as non-water-logged.

This matrix is the basis for calculating several accuracy metrics that help evaluate classification performance.

Producer's accuracy quantifies the likelihood that a reference pixel is accurately classified. It is calculated for each class using the following formula:

$$Producer's\ Accuracy = \frac{Number\ of\ Correctly\ Classified\ Pixels\ for\ a\ Class}{Total\ Number\ of\ Reference\ Pixels\ for\ that\ Class} \tag{4.4}$$

For water-logged areas, this metric indicates the effectiveness of the classification process in identifying true water-logged regions.

Consumer's accuracy, also known as user's accuracy, measures the probability that a pixel classified as a certain class actually represents that class on the ground. It is determined by:

$$Consumer's\ accuracy = \frac{Number\ of\ Correctly\ Classified\ Pixels\ for\ a\ Class}{Total\ Number\ of\ Pixels\ Classified\ as\ that\ Class} \tag{4.5}$$

This metric reflects the reliability of the classified water-logged pixels.

The kappa coefficient (κ) is a statistical factor that evaluates the agreement between the classified and reference data, accounting for the possibility of chance agreement. It is calculated as:

$$\kappa = \frac{P_o - P_e}{1 - P_e} \tag{4.6}$$

Where:

P_o is the observed agreement (the proportion of correctly classified pixels).

P_e is the expected agreement (the proportion of agreement expected by chance).

The kappa coefficient ranges from -1 to 1, with higher values indicating stronger agreement beyond chance, thus reflecting more reliable classifications.

4.6 The Google Earth Engine Application

Google Earth Engine (GEE) provides significant benefits over conventional GIS, which are attributed to its reliance on cloud computing and vast data repository. GEE, unlike traditional GIS, which relies on storage capacity and processing power limited by the users' resources, taps into Google's cloud platform to provide virtually unlimited storage and computational capabilities. Consequently, one can analyse extensive datasets such as satellite images spanning many years faster using GEE, without needing much local resources. Furthermore, its extensive library of geo-spatial datasets grants users easy access to a diverse array of information, facilitating more comprehensive and efficient analysis. The ability of the platform to manage complicated temporal and spatial operations through simple scripting increases its relevance, thereby making advanced geographical research tools more accessible to broader categories of users, which include researchers and decision-makers.

One notable dataset available through GEE is the Joint Research Centre's (JRC) Pekel et al., (2016) Global Surface Water dataset. The JRC is a European Union organisation that developed this dataset, which gives information about where and when surface water has occurred worldwide during the past three decades. It describes global surface water dynamics, identifies permanent and seasonal water bodies, and tracks changes over time. The JRC dataset is an important resource for understanding water-related phenomena, such as flooding, droughts, and changes in surface water extent due to human activities or climate change.

In this study, we have designed an application in GEE that enables users to visualise waterlogged areas over a specified period from 1984 onwards. One of the primary advantages of our application is its ability to enable users to select a specific time period range for visualising waterlogged areas. Unlike existing datasets available on the web, such as the JRC's Pekel et al. (2016) dataset, which offers a fixed range of time, our application is flexible to customisation. The Pekel et al. (2016) dataset is a valuable resource for understanding global surface water dynamics, but it is limited to a fixed temporal date range and has many temporal gaps in the available data. This can prove to be restrictive for researchers, planners, and other stakeholders who require a more detailed and dynamic analysis of waterlogged areas over specific periods of time. For instance, understanding the changes in waterlogged areas during specific seasons, years, or decades can offer important insights into the effects of changing climate, land-use, land-cover changes, and hydrological regime changes. The GEE application addresses this need by enabling users to select any desired time frame within the period from 1984 onwards. This flexibility allows for more detailed and context-specific analyses and provides a better understanding of the reasons for the change in water-logged areas.

By integrating Google Earth Engine (GEE) into our application, we use cloud computing capabilities and large datasets to provide an analysis in real-time, where one can observe waterlogged regions. Using a simple and intuitive interface, users can quickly choose their desired start and end dates, thereby enabling instant generation of maps that represent waterlogged areas during the selected period. This solution-based method enhances user interaction and analytical possibilities for the user. For example, a researcher studying the effects of a particular weather event on waterlogging can pinpoint the exact dates surrounding the event to observe changes and patterns. The same is true for any period of time, say several years, for which urban planners might assess flood-prone areas, establish long-term trends and formulate appropriate mitigation measures. The flexibility to select specific time periods makes the application valuable across various fields. In agriculture, it can be used by farmers together with agronomic experts to monitor waterlogged soils, which influence plant growth and crop yield. In disaster management, historical waterlogging data can enable early warning system development by pointing out places that face this problem frequently and where emergency services should concentrate their efforts to save people’s lives. The application leverages the GEE cloud-based platform to efficiently process over 300 Landsat images annually, a task that would be highly time-consuming and computationally intensive on standard computers. For example, image pre-processing, cloud masking, and composite generation are performed more rapidly thanks to Earth Engine’s state-of-the-art algorithms based on the high-speed performance of the computation processes associated with them. This enables us to create annual mosaics, detect changes, and carry out time-series analyses in minutes which would have taken hours or even days when accomplished using standard GIS software.

Moreover, the integration of JRC information for comparison purposes serves to enrich its analytical capacity and provide more inclusive viewpoints when juxtaposed against other datasets. Through this, one can effectively contrast different datasets against the high-quality data from the JRC. A further option that has been integrated is the incorporation of a groundwater layer generated from groundwater level readings. This dataset allows people access to information on groundwater resources that, in turn, improves the application's ability to analyse and manage water resources. Thus, when

JRC data alongside groundwater level information is included in the application, it creates a more comprehensive hydrological analysis platform. This implies that temporal variations could be observed, trends could be detected, and informed decisions could be made by combining information such as satellite images, JRC data, and groundwater data. Consequently, such a comprehensive approach makes this application a potent tool for monitoring and managing water resources as it equips the users with capabilities based on their specific needs.

* * *

CHAPTER – 5

PRESENT GROUNDWATER RESOURCES

5.1 General

The analysis of present status of groundwater (GW) in the enroute commands of IGNP canal is important to analyse the past trends and present status of groundwater in the canal system. The analysis of present GW status is performed using the observed GW levels data of CGWB. Analysis was performed by conducting Mann-Kendall trend analysis on each observation well and by generating spatial maps using interpolation at seasonal and annual scales. The methodology used and results obtained are detailed in the following sections.

5.2 Present GW Scenario in/around Study Area

Groundwater levels indicate the overall GW balance of an area. In this study, GW level data acquired from CGWB were analyzed for the period from 2001 to 2020 to assess the current GW scenario and changes occurred during the past two decades. These datasets are available at different observation wells for four seasons. Through interpolation between datasets at different stations, it is possible to determine the characteristics of elements at any point in the region. CGWB measures depth to GW during April (pre-monsoon), August (monsoon), November (post-monsoon Kharif) and January (Post-monsoon Rabi). These datasets were obtained from India Water Resources Information System (INDIA-WRIS). An area of interest is identified for the GW trend analysis which consists of command areas of IGNP and adjacent area.

5.2.1 Analysis of GW level data

Data pre-processing

GW level data are processed to check the consistency of observations. For analysis, wells for which consistent data is available were selected. Wells with more 30% missing values were eliminated before analysis. A total of 282 selected wells were used in trend analysis and for creating spatial maps.

Interpolation

In order to derive groundwater level maps, data of observation wells was interpolated using Kriging, a geo-statistical interpolation technique. Kriging estimates interpolated surface from a spatially scattered set of points with z-values. The z-value, in this case, was the groundwater level from observation wells. To obtain the interpolated surface, kriging goes through a two-step process: first, it obtains spatial autocorrelation values using variograms and covariance functions, and second, it predicts the z-values. Kriging was applied to groundwater levels using a python program. The interpolated groundwater levels were used in analyzing the spatial variability of groundwater in the study command.

In order to investigate the seasonal fluctuations, groundwater level maps for four seasons, i.e. post-monsoon Rabi (January to March), Pre-monsoon (April to June), monsoon (July to September) and post-monsoon Kharif (October to December), were created and examined.

Trend analysis

Trend analysis was performed on the selected 282 wells, on seasonal and annual scales using modified Mann-Kendall (M-K) test (Hamed and Rao, 1998). The Mann-Kendall test is a non-parametric test for identifying trends in time series data. Being non-parametric, it allows to perform trend analysis on any distribution of data. The data values are evaluated as an ordered time series. Each data value is compared to all subsequent data values. The initial value of the Mann-Kendall statistic, S, is assumed to be 0 (e.g., no trend). If a data value from a later time period is higher than a data value from an earlier time period, S is incremented by 1. On the other hand, if the data value from a later time period is lower than a data value sampled earlier, S is decremented by 1. The net result of all such increments and decrements yields the final value of S. Further, in order to test the significance level, a probability test is integrated with the M-K test.

In this study, the modified Mann-Kendall (M-K) test developed by Hamed and Rao (1998) was used. For each season, an annual time series from 2001 to 2018 of depth to GW was created and used in the modified M-K test. Wells with rising and falling GW level were identified at a significance level of 0.05.

5.2.2 Present scenario of depth to GW

The analysis of groundwater levels in the IGNP region reveals distinct temporal and spatial trends. Observations at individual wells indicate a significant rise in groundwater levels over the past two decades, particularly in the lower command areas of Stage-I. In these areas, groundwater levels rose rapidly until 2008 and have since attained a relatively stable profile (**Figure 5.1**). A rising trend is evident across all seasons and locations, though the rate of change varies.

A considerable spatial variation in groundwater levels was observed across the region. The depth to groundwater varies from shallow levels (10–15 m below ground level) to much deeper levels (35–40 m below ground level). The maps illustrate minimum groundwater depths for 1997, 2007, and 2020. In 1997, groundwater depths exceeded 35 m below ground level in the upper commands, around 20–25 m in the middle commands, and 25–30 m in the lower commands. By 2007, the upper and middle commands experienced significant rises in groundwater levels, while the lower commands showed relatively deeper levels. In 2020, the upper commands exhibit a notable decline in groundwater levels, reflecting a reduction in waterlogging.

Spatially, groundwater in the northern sections of the command area, particularly the upper commands, is relatively shallow. However, moving toward the southern and western portions, especially in the lower commands, groundwater depth increases significantly, transitioning to deeper levels. These variations highlight the complex hydrogeological dynamics of the region over time.

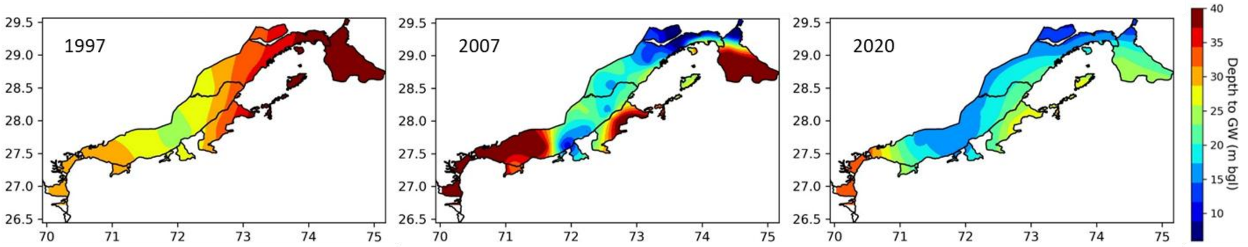

Figure – 5.1: Depth to groundwater (minimum of the year) in 1997, 2007 and 2020

5.2.3 Trends in GW levels

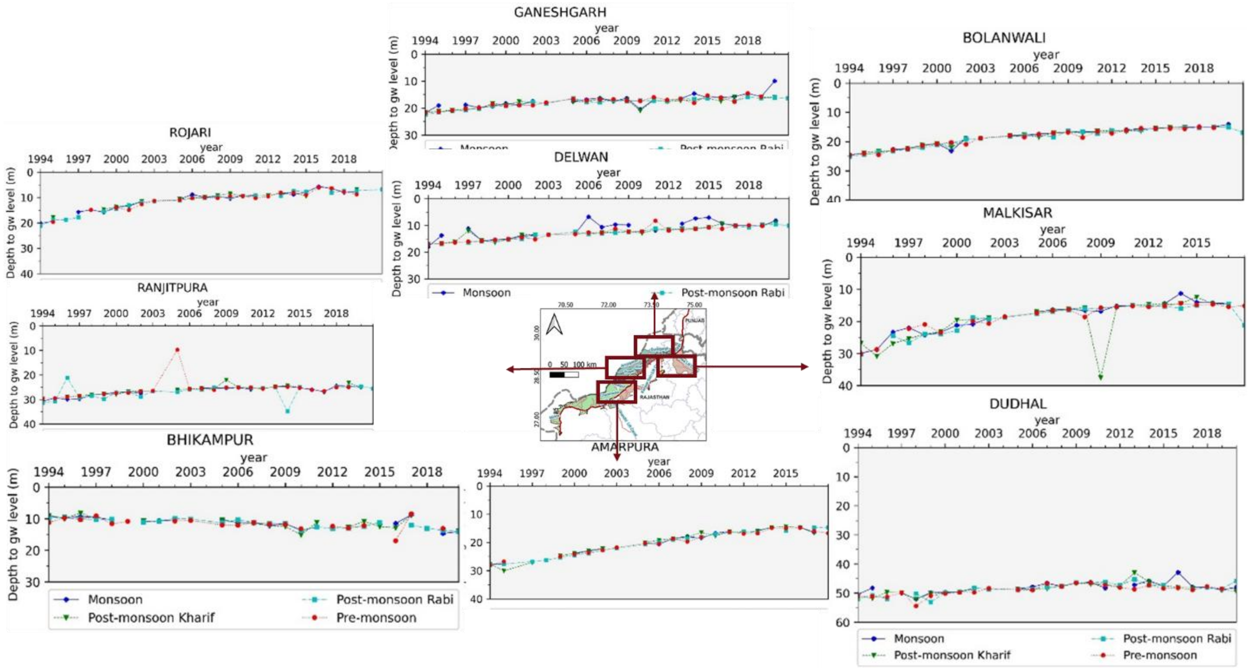

Figure – 5.2: GW depth trends across various locations in the command area.

Figure 5.2 presents detailed groundwater level analysis for various locations within the Indira IGNP command area, showing trends from 1994 to 2018 across different seasons. Each graph illustrates the depth to groundwater (GW) level over the years, with data segmented by seasons: Monsoon, Post-monsoon Rabi, Post-monsoon Kharif, and Pre-monsoon. In most locations, a gradual increase in groundwater depth (indicating a drop in groundwater level) can be observed over the years, reflecting potential depletion. For example, sites like Ganeshgarh and Bolanwali show a notable increase in groundwater depth, particularly during Monsoon and Post-monsoon Kharif periods. Bhikampur and Ranjitpura also show seasonal fluctuations but have relatively stable groundwater depths compared to other areas. Spatial maps of groundwater depths were created for various time periods from 1994 to 2018. In 1994, groundwater was observed to be deep in the upper commands, moderately shallow in the middle commands, and deep in the lower commands. By 2007, groundwater levels in the upper commands (such as Sardarpura, Masitawali, and Suratgarh) had become shallow. During the period from 2007 to 2010, the upper commands exhibited the lowest groundwater depths. In recent years, groundwater levels have declined in the upper commands but have risen in the lower commands.

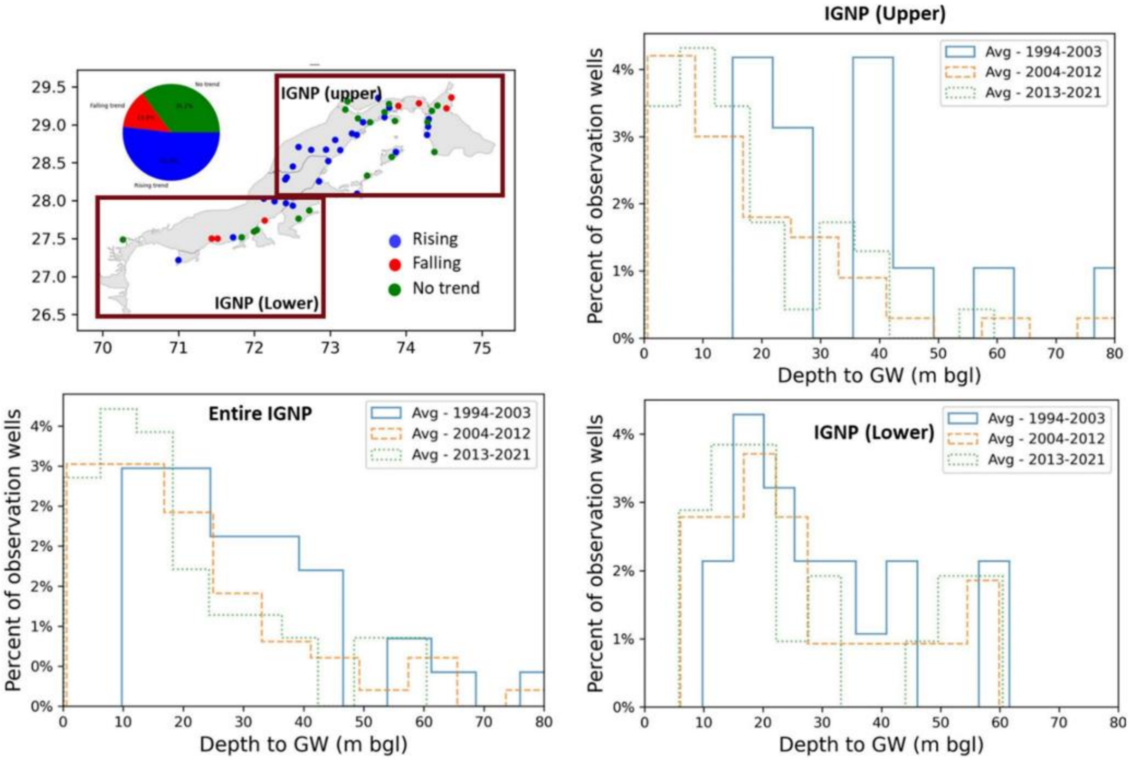

Figure – 5.3: Trend in depth to groundwater during the years 2001 to 2020 and the histograms of percentage of numbers of observation wells in the decades 1994-2003, 2004-2012 and 2013-21 in the lower commands, upper commands and all commands of IGNP.

Figure 5.3 illustrates groundwater trends in the IGNP using the modified Mann-Kendall test and depth-to-groundwater histograms for three time periods: 1994–2003, 2004–2012, and 2013–2021. The spatial analysis of trend at individual wells highlights that 52% of wells in the upper commands exhibit a rising groundwater trend, while 13% show a falling trend, and 35% show no significant change during the period 1994 to 2021. This suggests that waterlogging in the IGNP escalated during 1994–2010, followed by a decline in recent years. Despite these improvements, localized rising trends persist, although groundwater levels remain within safe limits.

The histograms compare depth-to-groundwater trends across the upper, lower, and entire IGNP. For the upper commands, groundwater levels were relatively deep (none below 15 m) during 1994–2003. During 2004–2012, a substantial rise in groundwater levels occurred, with many wells showing shallow groundwater, leading to extensive waterlogging. In 2013–2021, the situation improved, with fewer wells exhibiting shallow groundwater, reflecting reduced waterlogging risks. In the lower commands, groundwater levels remained within a safer range across all time periods. However, noticeable changes are evident, especially during 2004–2012, which corresponds to significant shifts in the groundwater regime.

* * *

CHAPTER – 6
SYSTEMS MODEL

6.1 Introduction to Systems Modeling

Comprehensive and rational water management is necessary for social and economic development, especially in situations of limited water resources. Water resources management involves rational use of scarce water and allied resources. Optimal solution of problems involving competitive water demands needs systems approach as a methodological way that takes all the internal and external relationships into account and utilizes systems theories solved through modern computer hardware and software. Modeling is a process or procedure that is intended to focus and provide clearer thinking to promote better decision-making. Hydrological modeling is defined as the characterization of real-world hydrologic features by the use of small-scale physical models, mathematical analogues, and computer simulations. A hydrologic model is a simplification of some real-life system (e.g., surface water, soil water, wetland, groundwater, estuary etc.) that aids in understanding, predicting, and managing the water resources.

The essence of simulation is to reproduce the behavior of the system in every important aspect to learn as to how the system will respond to conditions that may be imposed on it or may occur in the future. The main advantage of simulation models lies in their capacity to accurately describe the real-world systems. The proposed configuration of projects can be assessed to judge whether their performance would be adequate or not before investments are made. Likewise, operating policies can be tested before they are implemented in actual situations. Following steps are involved in the development and application of a simulation model:

a) Define the problem,
b) Describe the water resource system and its hydrological relationships,
c) Decide the model structure, input, and output,
d) Test the model (if not suitable, go to step ‘c’), and finally
e) Apply the model to the problem.

After the model of a system is developed and tested, experiments are conducted with it to investigate various scenarios or answer the question “WHAT IF?". The simulation models are much helpful in understanding the consequences or implications of changing one or more of the decision variables.

The main objective of the present study is to evaluate the impact of IGNP canal and its water utilization in the enroute commands on the groundwater resources under various scenarios related to changes in canal conditions and future climate. In this study, a python-based system model developed at NIH was utilized for simulating supply for irrigation and losses from the canal. The system model performs:

a) Estimation of recharge from main canal/distributary system, irrigation application/withdrawal from surface water or groundwater, and actual rainfall occurrence (in different climatic scenarios) in each command.

b) Estimation of evaporation and seepage losses in the main IGNP canal after accounting for water diversion for enroute command areas and supply for domestic/industrial demands from main canal corresponding to different scenarios of water availability at the canal head and demands in enroute commands corresponding to various scenarios of canal conditions.

c) Linkage of the systems model (giving SW – GW interaction) with the MODFLOW for estimation of revised groundwater table corresponding to revised patterns of GW withdrawal and recharge.

6.2 Description of Systems Model

A Systems model has been developed for interaction analysis of IGNP canal and its enroute commands with groundwater (GW) resources. The main objective of the model is to compute the GW pumping requirements and occurrence of recharge to GW under various climatic, agricultural, and water availability scenarios after the introduction of IGNP canal. The model components are shown in **Figure 6.1**.

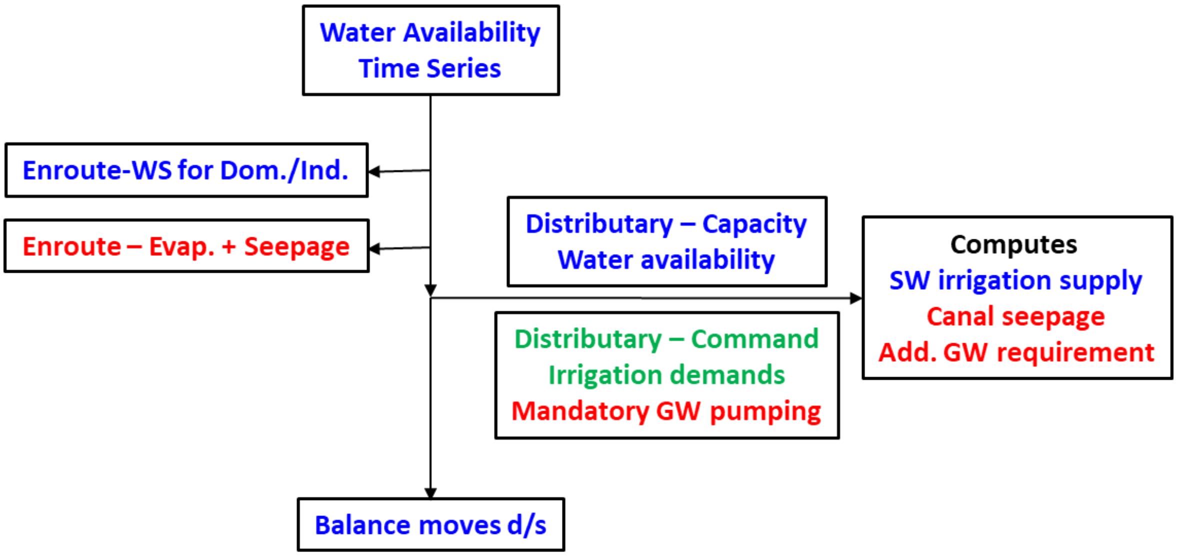

Figure – 6.1: Components of the Systems model for SW – GW interaction

Water availability time series (in Cumecs) is available at the head of a canal system. In the enroute canal segment, water is diverted for meeting the domestic supply and industrial demands of the adjoining buffer area. After accounting for the enroute diversions and available water in the canal segment, flow cross-section computations are revised and the top water surface area and wetted perimeter are worked out. Top water surface area is used to compute the evaporation losses while wetted perimeter is used to compute the percolation losses from the canal segment (as per the rates specified by GEC-2015). A number of iterations of the flow cross-section of canal segment are made till the computations stabilize.

At the point where a distributary canal takes off from the main canal, water is diverted in the distributary canal at the rate which is minimum of the water availability in main canal and the carrying capacity of the distributary canal. The domestic and industrial demands and irrigation demands of all crops within the distributary command at each time step are worked out using NIH-WISDOM after accounting for the mandatory GW withdrawal (to avoid development of waterlogging conditions in the command, if any). The net domestic/industrial demands, irrigation demands, and the demands for environmental purposes (if any) in the distributary canal command are compared with the available water in distributary canal during the time step and its run-time at full capacity is worked out. Based on the run-time and flow cross-section, the canal percolation to GW system is worked out and a number of iterations are made till the run-time computations stabilize. If the canal capacity is limited in comparison to the total demands in a time step, the balance demands are met through GW withdrawal. Within the distributary commands, rainfall and irrigation recharge are computed from WISDOM.

After accounting for the diversion in the distributary canal in a time step, the balance of the available water in main canal segment moves towards the downstream IGNP canal segment to meet the demands of other distributary commands and the water demands of enroute buffer zone. A schematic of Systems model showing overall methodology is also shown in **Figure – 6.2**.

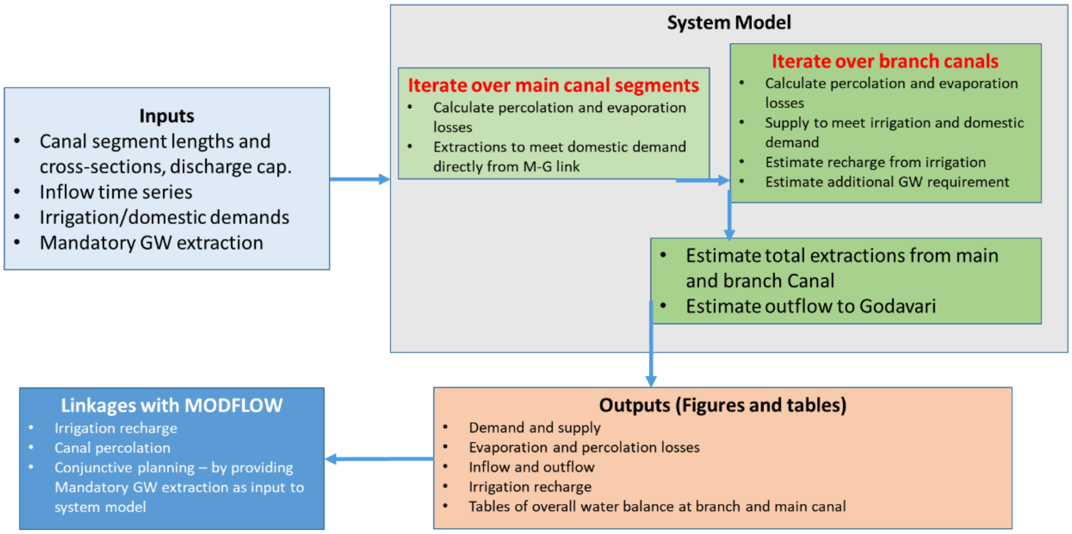

Inputs
- Canal segment lengths and cross-sections, discharge cap.
- Inflow time series
- Irrigation/domestic demands
- Mandatory GW extraction

System Model

Iterate over main canal segments
- Calculate percolation and evaporation losses
- Extractions to meet domestic demand directly from M-G link

Iterate over branch canals
- Calculate percolation and evaporation losses
- Supply to meet irrigation and domestic demand
- Estimate recharge from irrigation
- Estimate additional GW requirement

- Estimate total extractions from main and branch Canal
- Estimate outflow to Godavari

Outputs (Figures and tables)
- Demand and supply
- Evaporation and percolation losses
- Inflow and outflow
- Irrigation recharge
- Tables of overall water balance at branch and main canal

Linkages with MODFLOW
- Irrigation recharge
- Canal percolation
- Conjunctive planning – by providing Mandatory GW extraction as input to system model

Figure – 6.2: Schematic of overall methodology of the Systems model

The Systems model, as described above, has been developed in Python programming language. Various iterations are made at the level of each distributary command and the IGNP main canal segments so as to compute the SW supply to meet various domestic/industrial and irrigation demands and recharge from the canal system and irrigation application to GW aquifers. A view of the model and its output is shown in **Figure – 6.3.**

```
    'y_label': ['Domestic & Industrial Demand', 'Irrigation (FIR) Demand', 'Percolation Los
    'color': ['#DC8686', '#2D9596', 'orange', 'red', 'gray', 'green', 'cornflowerblue'], #,
    'yaxis_label': 'Demand/supply (MCM)',
    'title': 'Monthly losses and extractions for the year 2015',
    'outfileName': 'monthly_demand-supply_year2015.png',
    'xlabel_interval': 1,
    }

plotLines(plot_data)

year = 2015
df = lumpsum_annual[lumpsum_annual['year']==year]

plot_data = {
    'sizes': [df['supply_mandatory'].values[0], df['perc_loss'].values[0], df['evap_loss'].
    'labels': ['Domestic & Industrial Supply', 'Percolation Losses', 'Evaporation Losses',
    'title': 'Supply Proportions (' +str(year) +')',
    'colors': ['#00A8E8', '#FF6B6B', '#FFD166', 'cornflowerblue'],  # Optional colors
    'outfileName': 'supply-proportions_year2015.png',
}


plotPieChart(plot_data)

#Annual tim-series
df = lumpsum_annual.copy()
df = df.sort_values(by='year')
df = df.iloc[1:-1]
x_axis = df['year'].values

plot_data = {
    'x': x_axis,
    'y': [
    df['mandatory_demand'].values,
    df['fir'].values,
    df['perc_loss'].values,
    df['supply_mandatory'].values,
    df['supply_fir'].values,
    df['evap_loss'].values,

    ],

    'y_label': ['Domestic & Industrial Demand', 'Irrigation (FIR) Demand', 'Percolation Los
    'color': ['#DC8686', '#2D9596', 'orange', 'red', 'gray', 'green', 'cornflowerblue'], #,
    'yaxis_label': 'Demand/supply (MCM)',
    'title': 'Annual losses and extractions',
    'outfileName': 'annual_demand-supply.png',
    'xlabel_interval': 2,
    }

plotLines(plot_data)
```

```
...:     'title': 'Supply Proportions (' +str(year) +')',
...:     'colors': ['#00A8E8', '#FF6B6B', '#FFD166', 'cornflowerblue'],  # Optional colors
...:     'outfileName': 'supply-proportions_year2015.png',
```

Figure – 6.3: A view of Systems model in Python along with graphical output

The outputs of the Systems model are obtained for the main IGNP canal and the distributary commands separately. Most important outputs that are provided by the Systems model include evaporation and recharge losses in the main canal and the distributary canals, use of canal water to meet various demands (domestic/industrial and irrigation) in the main canal and the distributary commands, additional GW pumping requirements to meet various demands (if could not be met from the available canal water), and the outflow to Phase 2 from the main IGNP canal. A number of water balance checks have been introduced so as to avoid/check any error in the computations.

Results are obtained in tabular as well as graphical form for easier visualization. A few graphs that are generated using the Systems model are presented in **Figure – 6.4** for the sake of illustration.

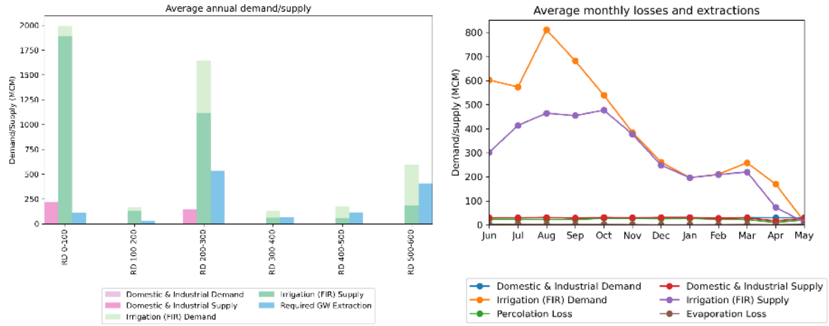

Figure – 6.4: A view of graphical outputs of the Systems Model

6.3 Computation of mandatory GW withdrawal for conjunctive use

The computed GW pumping/recharge corresponding to a particular scenario are convoluted with the calibrated GW model to find the impact of that scenario on GW resources. The results of GW model simulation are compiled and the area of command with shallow depth to GW (< 3 m) in the post-monsoon Kharif season is worked out at different time steps. The difference in water-logged area with conjunctive use and under BAU are compared.

The WISDOM allows automatic calculation of mandatory groundwater pumping to reduce water logging. It estimates the volume of groundwater to be extracted every year to decline the water table by a specified depth. Grid-wise pumping is estimated and assigned to MODFLOW.

* * *

CHAPTER – 7
INTEGRATED MODELLING FOR CONJUNCTIVE MANAGEMENT OF WATER RESOURCES

7.1 Integrated Modelling

Groundwater recharge is an end-result of various processes happening in surface-subsurface and governed by various influxes, such infiltration and irrigation, and outfluxes, such as root water uptake and soil evaporation. Therefore, in order to mimic all such processes, an integrated model is needed. The integrated model developed in this study consists of various modules which simulate processes in unsaturated and saturated zones. The model has three simulation modules, namely Root Zone Flow (RZF), Unsaturated Zone Flow (UZF), and Groundwater Flow (GWF) (**Figure 7.1**). The integrated model is encapsulated into a web-based system which consists of python-based modules, Google Earth Engine (GEE) API, thematic and time-series database. The developed integrated system is named as NIH's Web-based Integrated Catchment Modelling System for Decision Making (NIH-WISDOM). It is empowered by well-stablished hydrologic models, such as MODFLOW, for reliable hydrologic simulations. Theory and concepts used in the integrated model are elaborated below.

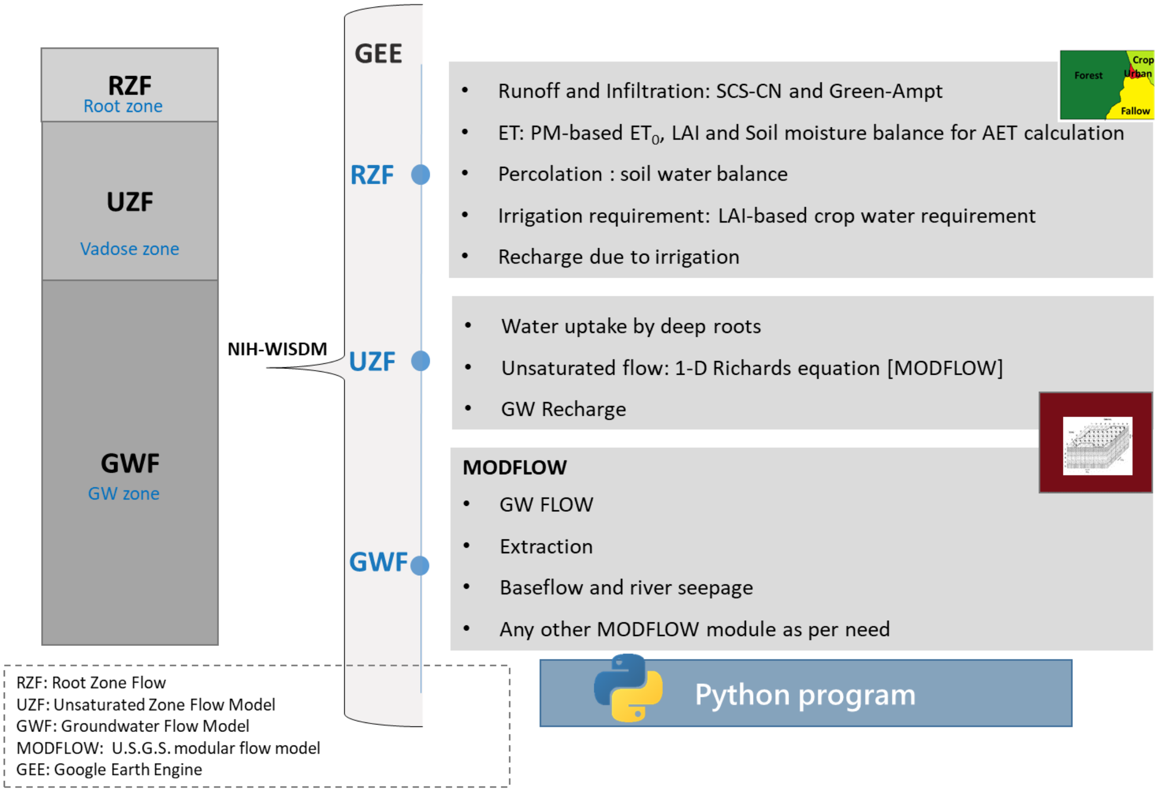

Figure – 7.1: Methods used in simulating surface and sub-surface hydrological variables

7.2 Root Zone Flow (RZF) Module

The RZF is developed during the present study at NIH to simulate processes in the top soil layer (say, upto 500 mm). All the processes happening at top soil layer, such as runoff, infiltration, ET from top soil layer, soil evaporation, etc., are simulated by RZF. RZF is tightly coupled with Unsaturated Zone Flow (UZF) module to further simulate the processes in the vadose zone, such as ET from deep roots and recharge. RZF uses the well-established methods of hydrology to simulate various components, such as SCS-CN, Green-Ampt, Penman-Monteith, etc. These methods are elaborated in the following sections.

7.2.1 Runoff and infiltration

The model provides two methods for estimating runoff, the SCS-CN and Green-Ampt. Runoff is simulated using Green-Ampt when the sub-daily precipitation data is available, the SCS-CN is used otherwise.

SCS-CN method

The Soil Conservation Service - Curve Number (SCS - CN) method is developed by Soil Conservation Service (now called the Natural Resources Conservation Service), U.S. Department of Agriculture (USDA - SCS, 1972). Since its introduction in 1954, the SCS-CN method has become the standard method, in practice, for estimating an event-based rainfall-runoff response. In addition, the popular models, such as Soil and Water Assessment Tool (SWAT) and Soil Water Balance (SWB) Model of USGS, use it for runoff simulation at daily time-step.

According to the SCS-CN method, the ratio of the actual amount of direct runoff to the maximum potential runoff is equal to the ratio of the amount of actual infiltration to the amount of the potential maximum retention. It also assumes that the initial abstractions are fraction of the maximum potential retention. The runoff can be estimated using Eq-7.1.

$$Q = \frac{(P-I_a)^2}{(P-I_a+S)} \tag{7.1}$$

Where, Q is the direct runoff, P is precipitation, I_a is initial abstraction and S is the maximum potential retention. Generally, the I_a is considered as 20% of S, however, in some cases it varies with precipitation intensity. The S is estimated using the Curve Number which is assigned based on combination of land uses and soil.

$$S = \frac{25400}{CN} - 254 \tag{7.2}$$

Where, S is in mm. The CN is assigned using standard values available from literature considering the land uses and soil hydrologic group. Once the runoff is derived, infiltration can be derived using water balance. Total infiltration (F_{day}) at a grid can be estimated as

$$F_{day} = F_i + F_u \qquad (7.3)$$

where,

$$F_i = 0.2 \times S - i \qquad \textit{for } i \leq 0.2 \times S \qquad (7.4)$$

$$F_i = 0 \qquad \textit{for } i > 0.2 \times S \qquad (7.5)$$

$$F_u = P - 0.2 \times S - R \qquad \textit{for } P \geq 0.2 \times S - P \qquad (7.6)$$

$$F_u = 0 \qquad \textit{for } P < 0.2 \times S - P \qquad (7.7)$$

Where, i is interception, F_i is initial infiltration and F_u is final infiltration.

7.2.2 Modifications to SCS-CN

In standard application of SCS-CN method, the condition of land use is generally ignored and the CN values are assigned assuming average/good condition. However, in real, the classes such as forest/shrubs exhibits considerable variations in canopy coverage which affects the canopy interception. In addition, considering rapid urbanization, the impervious surface cannot be assumed constant for entire simulation period. Generally, the CN of urban areas are assigned taking a single land use map which might introduce uncertainties in the runoff estimation as there might have several land cover changes during the period of simulation. In the developed model, the CN is assigned dynamically considering the canopy coverage (8-daily) and impervious surface (annual) time series data. The CN values are assigned at each time step by interpolating values between a user specified minimum and maximum CN values (**Figure 7.2**).

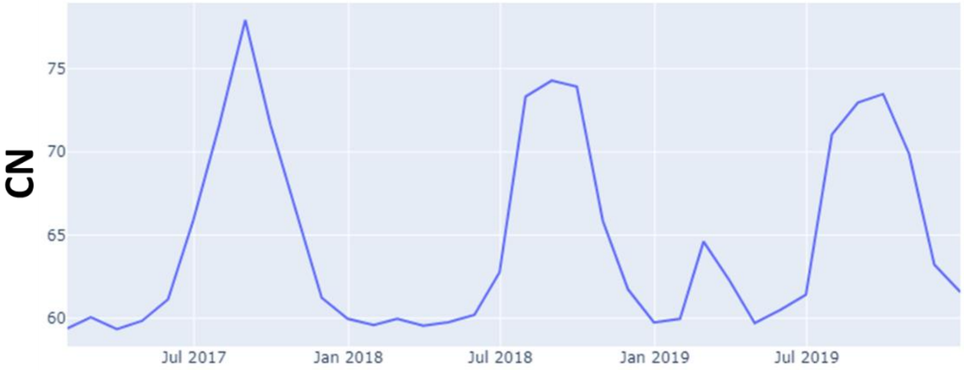

Figure – 7.2: CN values in a forest grid using the developed approach

7.2.3 Green-Ampt (GA) method

The GA method is developed by Green and Ampt in 1911 by applying Darcy's law to homogeneous soil with constant hydraulic conductivity, initial water content and head at the wetting front (Mullem et al., 1991). They proposed a simple model for water infiltration into a homogeneous soil with a uniform initial water content. The saturated wetting front is assumed to move downwards as a single piston like displacement.

The GA is a process-based model which can simulate sub-daily infiltration. It simulates instant infiltration rate for a given wetting front. The location of wetting front is updated after each iteration. The cumulative infiltration can also be simulated using the GA method. The infiltration rate at a given time is given by the following equation.

$$f(t) = K_s + K_s \frac{|\psi_f|(\theta_s - \theta_i)}{F} \qquad \textit{for } t>t_p \tag{7.8}$$

$$f(t) = P \qquad \textit{for } t\leq t_p \tag{7.9}$$

Where, f(t) indicates rate of infiltration (L/T), K_s is the saturated hydraulic conductivity, ψ_f is the matric potential at the wetting front, θ_i and θ_s are the initial and saturated soil moisture contents, and F is the cumulative infiltration (L). In order to estimate f(t), the time to ponding is to be estimated first using the following equation.

$$t = t_p + \frac{1}{K_s}\left[F - F_p + |\psi_f|(\theta_s - \theta_i)\ln\left(\frac{|\psi_f|(\theta_s-\theta_i)+F_p}{|\psi_f|(\theta_s-\theta_i)+F}\right)\right] \tag{7.10}$$

where F_p is the amount of water that infiltrates before water begins to pond at the surface and t_p is the time it takes to have water begin to pond at the surface [T]. The F_p *and* t_p can be estimated using the expression:

$$F_p = \frac{|\psi_f| K_s(\theta_s-\theta_i)}{P-K_s} \qquad t=t_p \text{ and } P>K_s \tag{7.11}$$

$$t_p = \frac{F_p}{P} \tag{7.12}$$

Equation 7.11 is solved for F_p in the model using the Newton-Raphson method. The θ_i is updated at daily time step. The daily cumulative infiltration is then used in the other water balance calculations. In GA method, the infiltration is estimated first, the runoff is then estimated using the water balance approach. The interception losses and infiltration are subtracted from the total precipitation to get the runoff. Since the GA is applied at sub-daily time step, the daily runoff is estimated by summing the runoff for the respective day.

7.2.4 Evapotranspiration (ET)

Potential Evapotranspiration (PET) is estimated using Penman-Monteith equation (Allen et al., 1989). The Actual ET (AET) is then estimated by applying the vegetation and soil moisture resistances over PET. The model divides the grid cell into three biophysical components, i.e. vegetation, soil and impervious surface for estimating the AET (Ritchie, 1972). The maximum transpiration from the vegetated fraction is estimated using the empirical relationship between maximum transpiration and Leaf Area Index (LAI) as follows:

$$Tr_{max} = PET \times (LAI/3) \qquad \textit{for } LAI\leq 3 \tag{7.13}$$

$$Tr_{max} = PET \qquad \textit{for } LAI>3 \tag{7.14}$$

Where, Tr_{max} is the maximum transpiration from the vegetation. The water uptake from the roots varies with depth, it is found that a major portion of transpiration occurs from the top soil layer. According to FAO, 40% of the total transpiration occurs from just 25% of root depth. To simulate this phenomenon, the following exponential relationship is used. The same is also employed in the well-known hydrological model-SWAT. This decay of transpiration with depth is estimated essentially to divide the ET from top and bottom soil layers. The maximum transpiration from the top soil layer ($tr_{max\text{-}top}$) is estimated as

$$Tr_{max-top} = Tr_{max} \times \frac{\left(1-e^{-\beta\times depth/root\_depth}\right)}{\left(1-e^{-\beta}\right)} \qquad (7.15)$$

Where, *depth* indicates soil layer depth, *root_depth* indicates the root depth of the vegetation. The maximum transpiration from the bottom soil is estimated by subtracting the $Tr_{max-top}$ from Tr_{max}. Further, to estimate the actual transpiration the soil moisture availability constraint is imposed. Actual transpiration from the top soil layer is estimated as

$$ATr_{top} = Tr_{max-top} \qquad \text{for AMC} \geq 0.25\times\text{AMC}_{max} \qquad (7.16)$$

$$ATr_{top} = Tr_{max-top} \times e^{\left(5\times\left(\frac{AMC}{(0.25\times AMC_{max})}\right)-1\right)} \qquad \text{for AMC} < 0.25\times\text{AMC}_{max} \qquad (7.17)$$

Where, AMC_{max} is the maximum available soil moisture and *AMC* is the available soil moisture at the respective time step. In order to check if the actual transpiration is not exceeding the AMC, the minimum of the ATr_{top} and (*depth*×*AMC*) is taken as the final ATr_{top}. The soil evaporation also decreases exponentially with depth. The evaporation from the top soil layer is estimated using the following relationship.

$$Ev_{max} = PET \times SCI \qquad (7.18)$$

$$Ev_{\max\_top} = Ev_{max} \times \left(\frac{depth}{(depth + e^{(2.374-0.00713\times depth)})}\right) \qquad (7.19)$$

Where, Ev_{max} is the maximum soil evaporation, SCI is Soil Cover Index, Ev_{max_top} is the maximum soil evaporation from the top soil. The actual soil evaporation from the top soil is estimated by constraining the maximum evaporation by the available soil moisture in the soil layer. The actual evaporation from the top soil AEv_{top} can be estimated using the following equation.

$$AEv_{top} = Ev_{top} \times e^{\left(2.5\times\frac{(\theta-FC)}{(FC-WP)}\right)} \qquad \text{for } \theta < FC \qquad (7.20)$$

$$AEv_{top} = Ev_{top} \qquad \text{for } \theta \geq FC \qquad (7.21)$$

Where, θ is the soil moisture at the time step, FC is the field capacity and WP is the wilting point. Further, it the maximum actual evaporation from the soil is restricted to a maximum of 80% of total available soil moisture in the layer on the respective time step. The actual total ET is the sum of transpiration and soil evaporation weighted by the fractions of vegetation and soil within the soil grid.

7.2.5 Soil moisture in top soil layer

Change in soil moisture is estimated at each time step by performing soil moisture balance (Neitsch et al., 2011). If soil moisture exceeds the maximum moisture holding capacity of the soil, the excess soil moisture content is converted to depth from volumetric water content and is considered as percolation to the second layer. At every time-step, change in soil moisture storage (Δθ) is calculated using the following formula.

$$\Delta\theta = \theta_{i-1} - AET_i + FIR_i \qquad (7.22)$$

Where, θ_{i-1} is soil moisture during previous time-step, AET is actual ET, FIR is field irrigation requirement, and i represent the time-step. Once the change in soil moisture is estimated, the soil moisture at the end of the time-step i is estimated as:

$$\theta_i = \theta_{i-1} + \Delta\theta \times \textit{depth} \qquad (7.23)$$

where, *depth* indicates soil layer depth.

7.2.6 Irrigation demand and supply

Irrigation is an important influx to sub-surface system that considerably affects AET, soil moisture and recharge. To make the recharge estimation more realistic, the inclusion of irrigation is therefore important. Estimation of irrigation demand in the model is based on the soil moisture balance in the RZF. At each time-step, the available soil moisture is estimated and the irrigation is added when soil moisture depletes beyond the specified allowable depletion.

$$FIR_i = (FC - \theta_i) \times \textit{root\_depth} \times \mathrm{vegFrac} / (\eta_{app}/100) \qquad (7.24)$$

Where, vegFrac is the fraction of vegetation in the model grid, and η_{app} is irrigation application efficiency (%). Note that the FIR is only estimated at time-steps when the soil moisture depletes below allowable limits. Effect of irrigation is simultaneously considered by supplying the amount of required irrigation (FIR). Change in soil moisture due to irrigation is considered using the equations 7.22 and 7.23.

7.2.7 Groundwater extraction

Groundwater pumping is an important component to estimate safe groundwater extraction and is also an input to MODFLOW. The rates of groundwater extractions are not readily available for most of the regions in India. Generally, such data are estimated using electricity bills assuming that the power consumptions is mainly due to groundwater pumps used in the agricultural fields. Other approach is to estimate such data using crop water requirement or groundwater fluctuations. However, despite considerable efforts by various government departments, it is still difficult to obtain time-series (say, monthly) of pumping using such methods which is a vital input to modelling. In the developed model, groundwater extractions are estimated internally utilizing the irrigation demand estimates. Since irrigation in many regions is applied from surface water (canal, tanks, lakes, etc.), it is important to subtract the demand that met from surface water. To incorporate this, fraction of demand that is met from surface water is to be supplied to model. The remaining demand is then met from groundwater. The model automatically generates pumping requirements under each grid and generates required mudflow files for well package.

7.3 Unsaturated Zone Flow (UZF) Module

UZF aims at simulating the flow in unsaturated zone. In case of WISDOM, the UZF simulates flow in the zone below the root zone (as simulated by RZF) but above the water table. UZF is a 1-D Richards Equation-based module of MODFLOW which is tightly coupled with RZF and GWF modules. The percolation from the top soil layer becomes the influx to the bottom soil layer which consists the deeper root and the unsaturated zone. The moisture movement in the unsaturated zone is simulated at daily time-step. The actual transpiration from the deep roots is also estimated by UZF. Maximum transpiration from deep root as estimated by subtracting the actual transpiration occurred at the top soil layer from the maximum transpiration, becomes input to UZF. In UZF, the actual transpiration from the deeper roots is estimated considering the moisture availability at each time-step. Finally, the sum of transpiration from the top and bottom soil layers is summed to get the total transpiration. The 1-D Richards equation represents the movement of water in unsaturated soil using a nonlinear partial differential equation

$$\frac{\partial\theta}{\partial t} = \frac{\partial q}{\partial z} - i = \frac{\partial}{\partial z}\left[D(\theta)\frac{\partial\theta}{\partial z} - K(\theta)\right] - i \tag{7.26}$$

Where, the q is the Water flux, i.e. percolation from the top soil layer, z is the elevation, D(θ) is the hydraulic diffusivity, K(θ) is unsaturated hydraulic conductivity, I indicates ET rate, I.e. the transpiration from the deep roots. The Richards equation is solved using the Finite Difference Method (FDE) in MODFLOW. Finally, the volumetric outflux, so called the recharge, is estimated. The detail description of the Richards's equation and UZF is out of the scope of this report, however, it can be found in UZF documentation (Niswonger et al., 2006).

7.4 Groundwater Flow (GWF) Module

Groundwater flow simulation is vital for simulation of recharge-pumping effects and river-aquifer interaction (Langevin et al., 2017). In addition, integration of groundwater model help validating the recharge by comparing groundwater head with observed heads. Results of integrated surface-groundwater model also help better decision making. WISDOM uses the very popular – modular hydrologic simulation program called MODFLOW – developed by U.S Geological Survey. MODFLOW discretizes the area of interest into several grids, control-volume units, to generate finite-difference equations (**Figure 7.3**). The finite-difference equations are formulated for intercell flow, boundary conditions and specified flows in terms of conductance. MODFLOW simulates groundwater flow in 3-dimensions using the Darcy's Law as described below.

$$q = -K\nabla h = \begin{pmatrix} K_{xx} & 0 & 0 \\ 0 & K_{yy} & 0 \\ 0 & 0 & K_{yy} \end{pmatrix} \qquad (7.27)$$

Where q is specific discharge, K is hydraulic conductivity, sub-scripts xx, yy and zz indicates hydraulic conductivity in x, y and z directions, h is groundwater potential head. When combined with a water balance on a small control volume, Darcy's Law leads to a partial-differential equation that describes the distribution of hydraulic head:

$$\frac{\partial}{\partial x}\left(K_{xx}\frac{\partial h}{\partial x}\right) + \frac{\partial}{\partial y}\left(K_{yy}\frac{\partial h}{\partial y}\right) + \frac{\partial}{\partial z}\left(K_{zz}\frac{\partial h}{\partial z}\right) + Q_s = S_s\frac{\partial h}{\partial t} \qquad (7.28)$$

where Q_s is a volumetric flux per unit volume representing sources and sinks of water, with Qs being negative for flow out of the groundwater system, and Q_s being positive for flow into the system. S_s is the specific storage of the porous material and t is time.

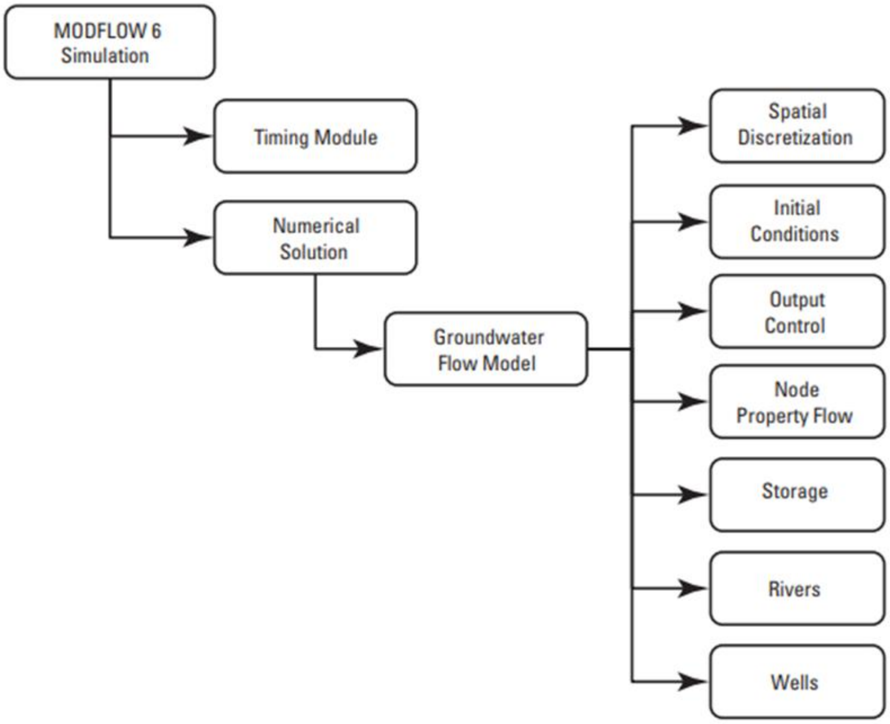

Figure – 7.3: MODFLOW components for groundwater flow simulation

Under real world conditions, the analytical solution of Partial Differential Equations (PDEs) of groundwater flow is rarely possible, therefore the CVFD (Control Volume Finite

Difference) method is used in MODFLOW. In CVFD, the continuous system described by PDEs is replaced by a finite set of discrete points in space and time, and the partial derivatives are replaced by terms calculated from the differences in head values at these points. The process leads to a system of simultaneous linear algebraic difference equations; the solution yields values of head at specific points and times. These values constitute an approximation to the time-varying head distribution that would be given by an analytical solution of the partial-differential equation of flow. The CVFD analog of PDEs may be derived by applying the rules of difference calculus; however, in the discussion presented here, an alternative approach is used with the aim of simplifying the mathematical treatment and explaining the computational procedure in terms of familiar physical concepts regarding the flow system. In MODFLOW 6, the discrete control volumes that comprise the model domain are called model "cells." Within each cell there is a point called a "node" at which head is to be calculated. Many schemes for locating nodes in cells could be used; however, the finite-difference equation developed in MODFLOW uses the block-centered formulation in which the nodes are at the center of the cells. Hydraulic communication between cells is conceptualized in terms of conductive connections between nodes. The assemblage of model cells and its associated network of connections is called the model "grid." To get further description of theory of MODFLOW, readers are recommended to refer to the MODFLOW documentations (Langevin, et. al., 2017).

In WISDOM, the MODFLOW integration mainly aims at the groundwater flow simulation in multi-layer groundwater system. To achieve this object, the required MODFLOW packages are selected and integrated in WISDOM (**Table-7.1**). Each MODFLOW module needs input files in specified format which consists of various options to activate/deactivate MODFLOW functions, package specific parameters, stress period data and time-series data. These inputs files can be created manually for real-case problems, and therefore, an automated process is required. WISDOM derives file for all the modules utilizing various distributed inputs, daily time-series, and user specified options and parameters. It also allows transformation of data from user uploaded excels and shape files. The input preparation for MODFLOW is WISDOM utilizes various python programs and a python library, called FloPy.

The MODFLOW discretizes the model domain into grids to consider spatial variations in various aquifer characteristics and to obtain solution of partial differential equations. The 3D schematic of MODFLOW is shown in **Figure 7.4** which illustrates the computation nodes, aquifer layers and active/in-active cells. MODFLOW writes output in binary and text files which can't be analysed directly. WISDOM reads all MODFLOW output files and convert to excel so that the time series and thematic outputs can be visualized later in WISDOM's dashboard.

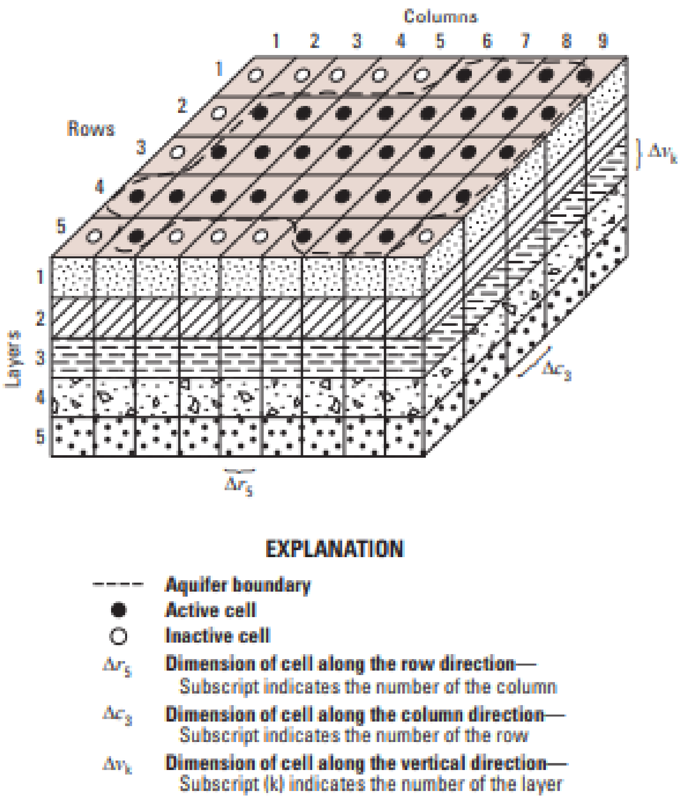

Figure – 7.4: Spatial discretization in MODFLOW (Source: Langevin, et. al., 2017)

Table – 7.1

MODFLOW modules used in WISDOM

Sr. No.	MODFLOW Module	Description
1	DIS6	Discretization package
2	NPF6	Node Property Flow Package Pane
3	STO6	Storage Package
4	UZF	Unsaturated-Zone Flow package
5	SFR6	Stream-Flow Routing package
6	WEL6	Well package
7	GHB6	General Head Boundary package
8	CHD6	Time-Variant Specified Head package

* * *

CHAPTER – 8
RESULTS AND DISCUSSION

8.1 General

This chapter presents the results of the analysis and modelling performed in this study. The areas under surface ponding as derived from remote sensing data and Google Earth Engine (GEE) are shown. A GEE application is developed in this study for monitoring surface ponding due to water-logging in the IGNP command. The application utilizes time-series data of remote sensing acquired by Landsat satellite. The results of integrated modelling under various scenarios are also presented in this chapter. These scenarios include changes in the condition of lining of the IGNP canal, and future projected changes in climate. The integrated modelling is performed using NIH's Web-based Integrated Catchment Modelling System for Decision Making (NIH-WISDOM) and NIH's System Model. The issues related to water-logging are prominent in the Stage-I of IGNP, therefore the analysis and modelling are performed only for the commands of Stage-I.

8.2 Surface Ponding

The IGNP is a vital irrigation project that has transformed the arid and semi-arid regions of Rajasthan by providing much-needed water for agriculture and domestic use. However, the project has also led to certain unintended consequences, one of which is the issue of surface ponding due to water-logging. Surface ponding refers to the accumulation of excess water on the land surface due to various factors such as over-irrigation, seepage from canals, and inadequate drainage systems. This phenomenon poses significant challenges to agriculture, the environment, and the livelihoods of the local population in the IGNP command area. One of the primary causes of surface ponding and water-logging in the IGNP region is the geological setting of the area and the percolation from the canal. The high infiltration capacity of soil in the area amplifies the recharge to groundwater due to canal leakages and irrigation. Hover, a considerable decline in surface ponding has been observed.

The problem of surface ponding in the IGNP command area is a multifaceted challenge that affects agriculture, health, and the environment. While the IGNP has been instrumental in bringing prosperity to the region, managing the adverse effects of surface ponding is vital for sustainable development. By combining technological advancements, infrastructural improvements, and community participation, the issue can be effectively mitigated, ensuring the long-term productivity and well-being of the IGNP region.

8.3 Google Earth Engine (GEE) App

Surface ponding in the IGNP command area was identified using the Google Earth Engine (GEE) application. The details and methodology used can be found in Chapter 4.

The app detects surface ponding within the IGNP command for any period from 1987 to 2023, and the resulting map can be exported to a GIS application for further visualization. It also displays the Global Surface Water data developed by Joint Research Centre (JRC) for reference and comparison. Moreover, it also integrates the recent groundwater level data in the study area. The application is shown in **Figure 8.1**. The application can be accessed using the link: https://ee-surveydaman.projects.earthengine.app/view/ignp-water-monitoring-app.

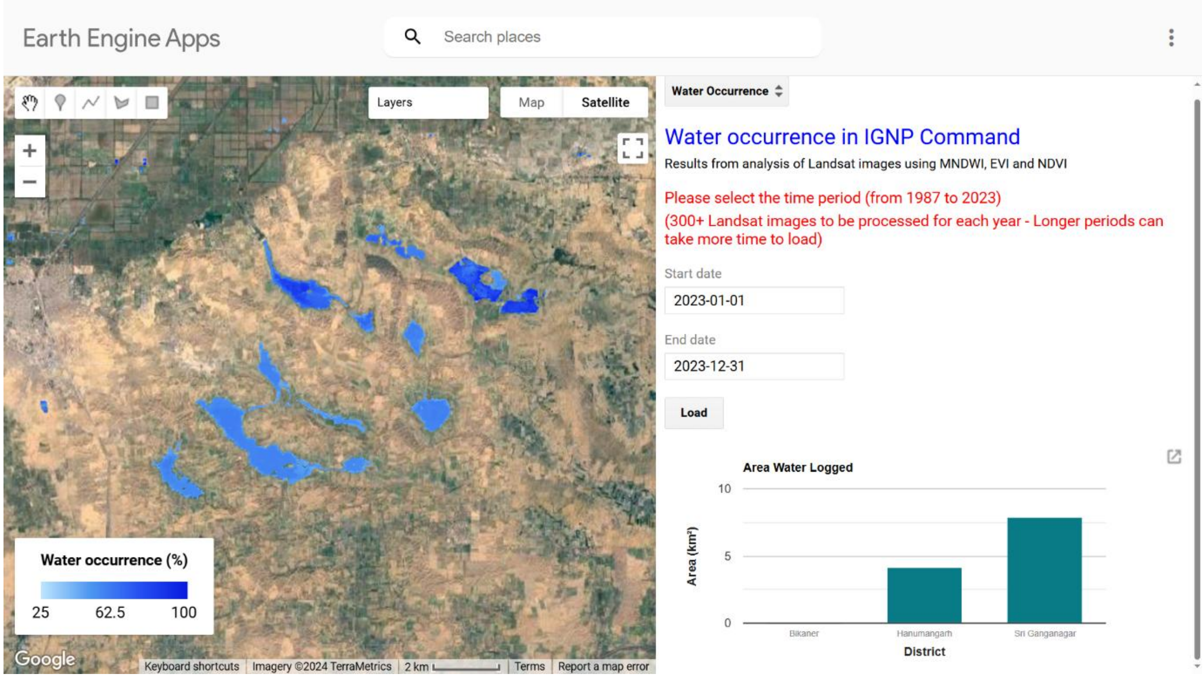

Water occurrence in IGNP Command

Results from analysis of Landsat images using MNDWI, EVI and NDVI

Please select the time period (from 1987 to 2023)

(300+ Landsat images to be processed for each year - Longer periods can take more time to load)

Start date: 2023-01-01

End date: 2023-12-31

Figure – 8.1: GEE App showing the water occurrence in the affected districts of IGNP.

The application calculates waterlogged areas district-wise, which can prove beneficial for mitigating water-logging in the affected areas. The area between Rawatsar and Suratgarh has been identified as water-logged. Due to its low-lying topography and geological settings, this place has been known for waterlogging and related issues since many years. In addition to the rise in groundwater, overflows from River Ghaghar also contribute to occasional surface flooding in the area. Figure 8.3 shows surface ponding in different years in the IGNP.

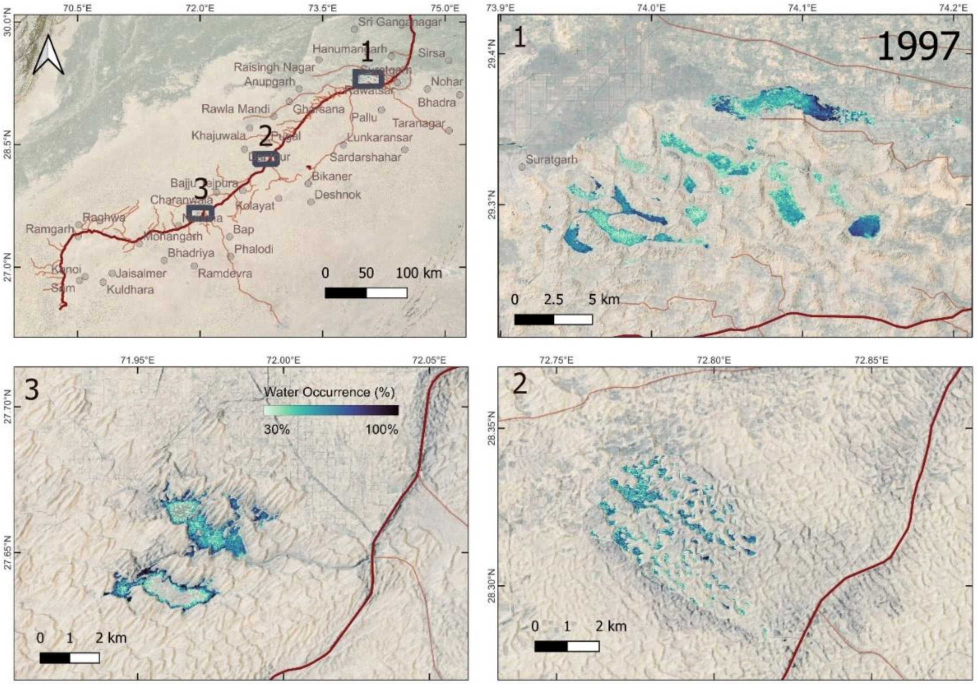

Figure – 8.2: Surface ponded areas identified using GEE app for the year 1997. The areas shown in the figure are just for demonstrating the capability of the app in identifying water pixels. Some of these areas could be the water storage reservoirs. These areas are excluded while calculating the total water-logging area.

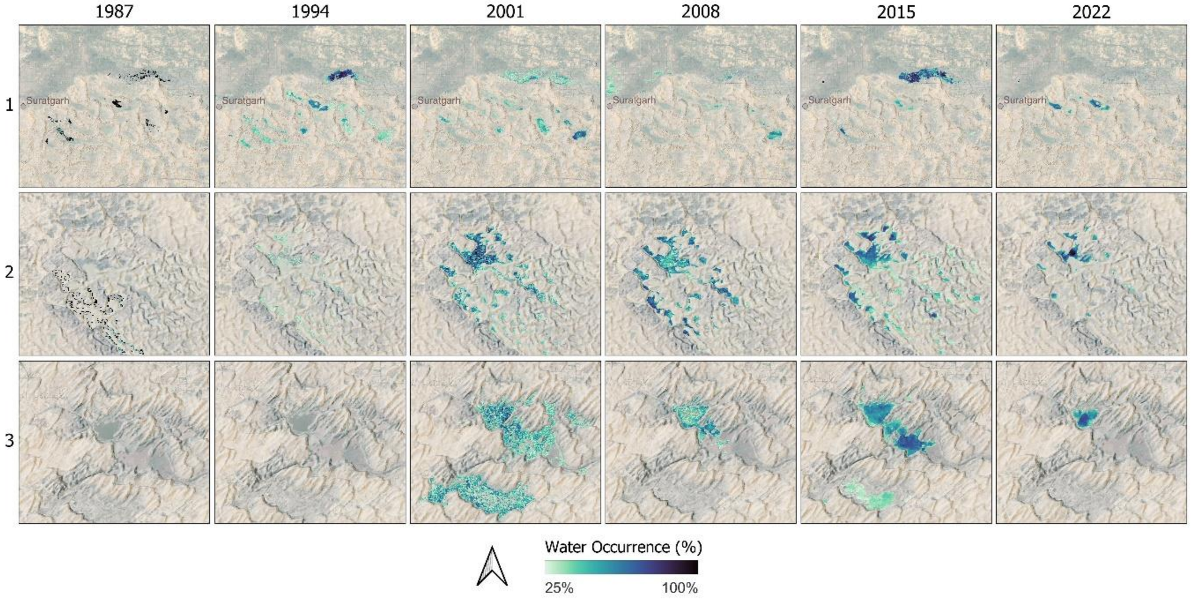

Figure – 8.3: Surface ponding condition for different periods in the three identified hotspots in the command area. The areas shown in the figure are just for demonstrating the capability of the app in identifying water pixels. Some of these areas could be the water storage reservoirs. These areas are excluded while calculating the total water-logging area.

In summary, the Google Earth Engine has been useful in identifying these waterlogged areas. The results can be utilized further by the state department to identify current water-logged areas and plan mitigation strategies for the affected areas.

The data obtained from the application was used to visualise the changes in the area of the two main districts in which the problem of waterlogging is the most widespread. Hanumangarh and Sri Ganganagar were identified as the districts with most areas having waterlogging conditions. **Figure 8.4** shows the temporal distribution of waterlogged areas in the two districts. In the initial phase from 1987, both the districts show an initial rise in the waterlogged areas, leading to an initial peak in waterlogging in the year 1990, with the total area affected by waterlogging peaking at around 58 km^2. For the initial peak year of 1990, out of the total waterlogged area, Sri Ganganagar was the most affected, with the total area affected by waterlogging adding up to around 39 km^2. For the same year, the area of Hanumagarh district affected by waterlogging was around 18 km^2. The increase in waterlogging in the late 1980s could be attributed to canal leakages and the development phase of the canal, leading extensively to waterlogging. The waterlogged area stabilised at around 30 km^2 from 1991 to 1995. This year was the peak year for waterlogging, with the total area of 62 km^2, of which 43 km^2 was in Hanumangarh and 19 km^2 in Sri Ganganagar. After 1997, a significant decline in waterlogged areas has been observed in both districts. The decreasing trend has been observed after 1997. The period after 2015 shows a gradual increase in waterlogged areas, particularly noticeable in the latest years (2022-2023), which can be attributed to variability in precipitation.

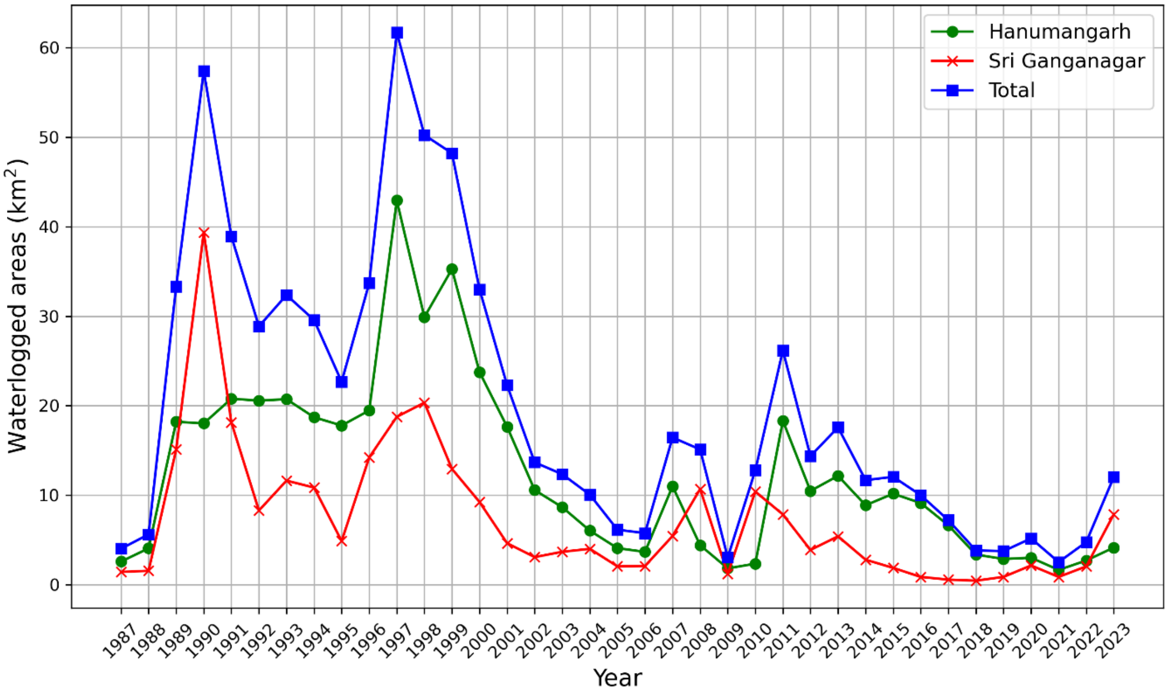

Figure – 8.4: Time-series plot of waterlogged areas (surface ponding)

Table 8.1: Command wise surface ponding (km^2) from 1987 to 2023

S.No	Command	1987	1991	1995	1999	2003	2007	2011	2015	2019	2023
1	Anupgarh	0.02	0.05	0.04	0.01	0.14	0.02	0.50	0.44	0.09	0.20
2	Bhojewala1	0.04	2.88	1.24	3.96	0.04	0.89	2.37	0.01	0.00	2.00
3	Bhojewala2	1.18	6.87	1.09	6.92	0.96	0.11	2.74	0.65	0.00	4.78
4	Kanau	0.00	2.46	3.08	2.82	0.04	1.88	2.12	0.22	0.00	0.60
5	Masitawali	0.00	0.15	0.27	0.35	0.02	0.14	0.14	0.04	0.12	0.11
6	Piperan	0.08	7.71	0.31	0.88	0.21	0.22	0.29	0.19	0.12	0.26
7	Sardarpura	2.06	12.46	9.25	18.44	4.63	7.41	11.71	6.28	1.89	1.90
8	Suratgarh	0.51	5.07	3.44	9.14	3.90	3.55	4.99	3.77	1.21	1.42
9	Zorawarpura	0.03	0.57	2.25	2.28	0.98	0.02	0.03	0.00	0.00	0.00
	Total	**3.92**	**38.22**	**20.96**	**44.80**	**10.93**	**14.23**	**24.89**	**11.60**	**3.42**	**11.25**

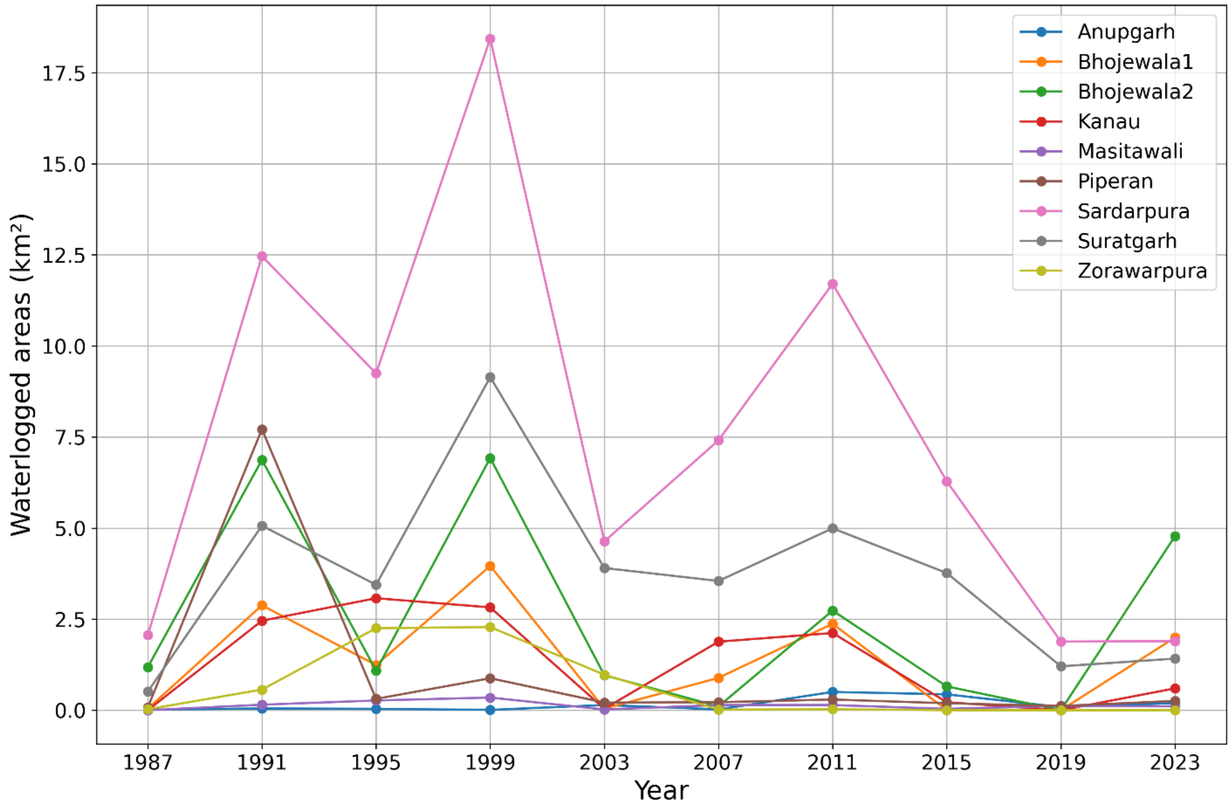

Figure – 8.5: Command-wise area of commands affected by surface ponding

8.4 Water Demands

In the present study, water demands have been computed for crop requirements under different scenarios. Irrigation water demands for crops depend on the reference evapotranspiration, actual rainfall in the area and the crop characteristics. The NIH-WISDOM was used to apply K_c based approach. Various remote sensing data, such Leaf Area Index and crop maps, were utilized. Details about the methods used for demand estimation are elaborated in the Chapter 7. The results obtained are described in the following sections.

The IGNP canal plays a crucial role in fulfilling both domestic and industrial water demands in Rajasthan. With its extensive canal network, IGNP provides water for drinking, power generation, and industrial uses, supporting the sustainability of various sectors in an otherwise arid region. A significant portion of IGNP's water is allocated for domestic consumption, ensuring drinking water supply to numerous cities and towns. Jodhpur, one of the largest cities in Rajasthan, receives 240 cusecs through the Jodhpur Lift Drinking Water Project, while the Nagaur Lift Drinking Water Project supplies 123 cusecs to meet the needs of the region. Bikaner, another major urban center, is supplied with 80 cusecs of drinking water via the Sobhasar Reservoir. Smaller towns such as Rawatsar and Jaisalmer also rely on IGNP water, with allocations of 55 cusecs and 30 cusecs respectively. The Pokaran-Falsoond Peyjal Yojana, an essential water supply scheme for the desert regions, receives 30 cusecs to ensure drinking water availability for rural settlements. Beyond domestic use, IGNP serves as a critical water source for industrial and power sector demands. Thermal power plants, which require substantial water for cooling, are among the largest consumers. The Suratgarh Thermal Power Plant, one of the most significant power generation units in Rajasthan, utilizes 75 cusecs of water. Other power stations, such as the Barsingsar Thermal Power Plant and the Rajwest Project, consume 25 cusecs and 40 cusecs respectively, while the Giral Project requires 24 cusecs. The Barmer Lift Project, which supports industrial development in the region, has an allocation of 50 cusecs. The Ramgarh Gas Distribution Project, is allocated 25 cusecs. Additionally, M/s V S Lignite Power Project Private Limited uses 5 cusecs, while the solar power project operated by M/s Godavari Green Energy Limited requires 1.6 cusecs for its operations.

For the system, the segment-wise supply for domestic/industrial purpose is derived from the data available from the Department of Water Resources (North), Rajasthan.

8.5 Impact of changing climate on different meteorological variables

For the climate change analysis, two different climate scenarios have been used and the daily maximum and minimum temperature and rainfall at ~ 25 km grid size have been worked out. From the gridded data, daily rainfall and maximum/minimum temperature in different commands have been computed. The precipitation is expected to increase in both the moderate and extreme scenarios (Table-8.2 and Figure-8.6a). The temperature is also expected to increase in the future (Figure 8.6b).

Table – 8.2

Average annual rainfall, max./min. temperature in Sardarpura command during various decades of future under Moderate and Extreme Scenarios of climate change

Decade	CMIP6 (Moderate)			CMIP6 (Extreme)		
	Rainfall (mm)	Max.Temp (ºC)	Min.Temp (ºC)	Rainfall (mm)	Max.Temp (ºC)	Min.Temp (ºC)
2021-30	342.96	33.11	20.38	320.78	33.46	20.41
2031-40	306.12	33.18	20.92	495.90	33.45	21.57
2041-50	327.99	33.90	21.31	414.42	34.16	22.58
2051-60	461.80	34.31	20.93	679.17	34.51	23.50
2061-70	556.71	34.34	21.67	577.56	35.21	24.58

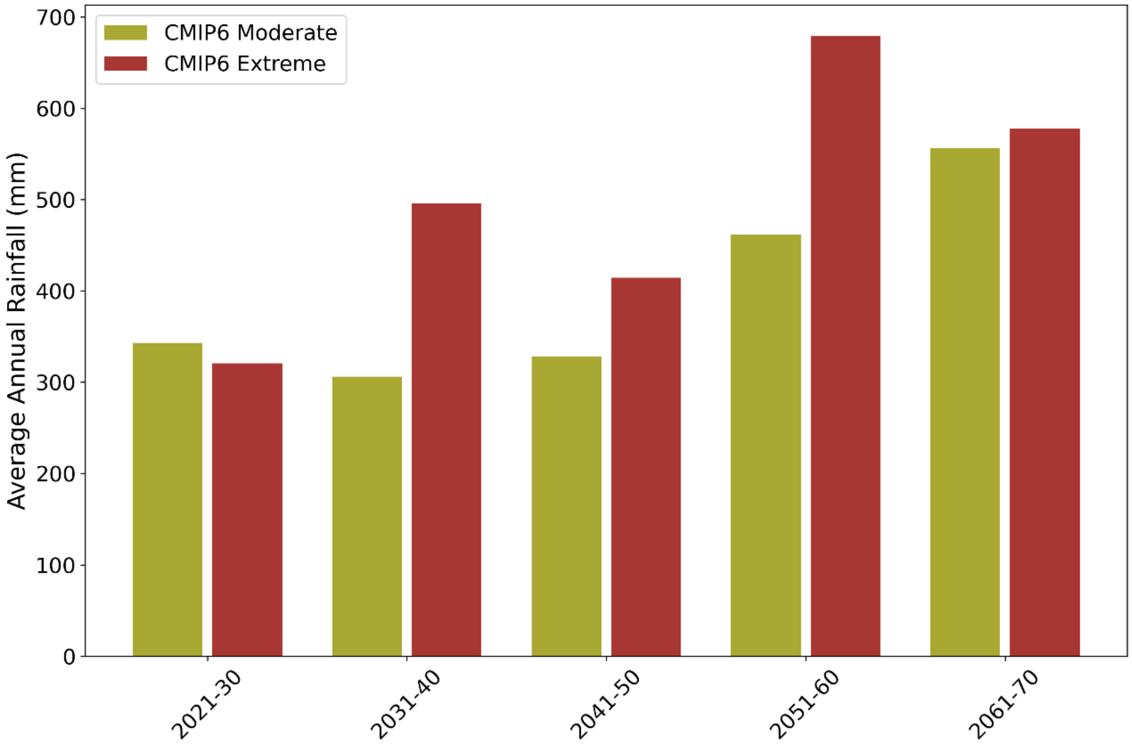

Figure – 8.6a: Average annual rainfall in different decades under CMIP6 climate scenarios

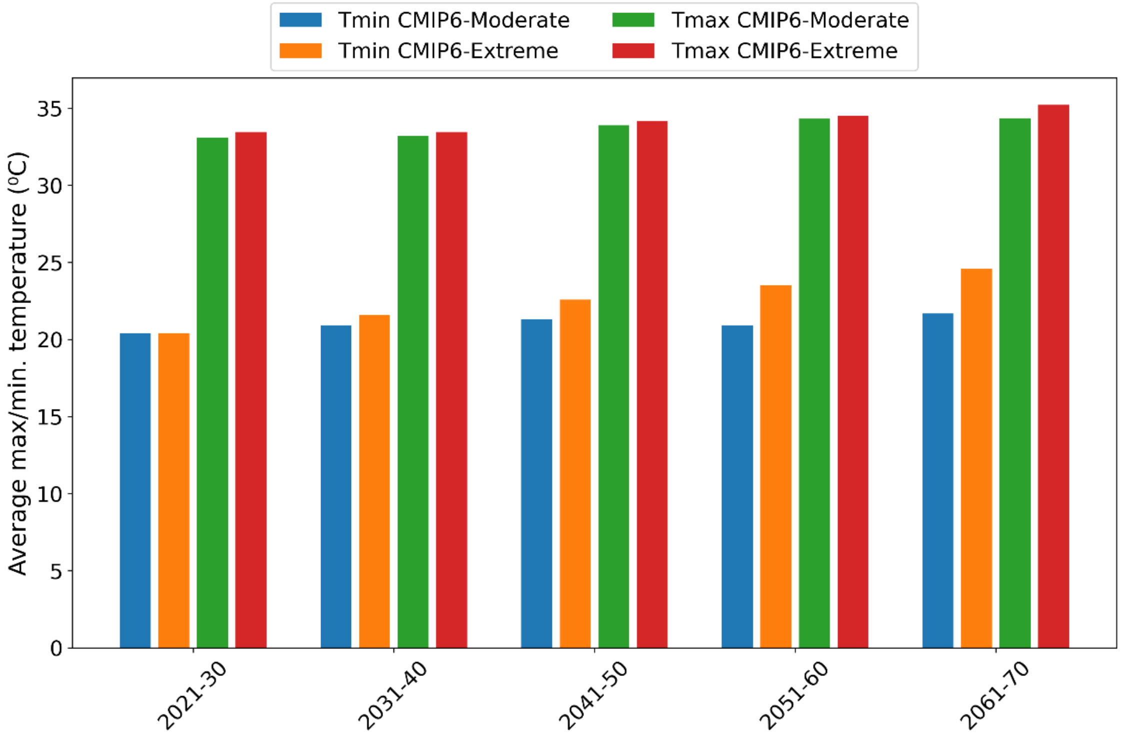

Figure – 8.6b: Average max./min. temperature in different decades under CMIP6 climate scenarios

To quantify the impact of climate change on water resources and hydrological conditions, two distinct Shared Socioeconomic Pathway (SSP) scenarios, SSP245 and SSP585, were considered in this study. SSP245 represents a moderate emissions scenario, where global climate policies and mitigation efforts are partially successful, leading to a gradual decline in greenhouse gas emissions after mid-century. This scenario assumes a balance between fossil fuel and renewable energy use, resulting in a moderate level of climate change impacts on temperature, precipitation patterns, and hydrological processes. On the other hand, SSP585 is a high-emission scenario, often referred to as the "worst-case" trajectory, where global reliance on fossil fuels continues unchecked, leading to rapid warming, extreme weather events, and intensified hydrological shifts. By analyzing these two contrasting scenarios, this study aims to assess the potential range of climate change effects on water availability, groundwater recharge, evapotranspiration, and overall water balance in the study region. This comparison helps in understanding the severity of projected changes and guides the development of adaptive water management strategies to mitigate climate-induced risks.

8.5.1 Future Projections of Precipitation

Precipitation patterns in the IGNP region are expected to undergo significant fluctuations over the coming decades, as indicated by the projections under different Shared Socioeconomic Pathways (SSPs). The precipitation anomaly trends suggest increased variability, with periods of excess rainfall interspersed with potential drought conditions. These changes in precipitation will have crucial implications for water availability, irrigation scheduling, and groundwater recharge in the IGNP command area.

The historical precipitation anomaly, represented by the black dashed line in **Figure 8.7**, indicates a high degree of variability even in the past, with fluctuations ranging between wet and dry periods. However, future projections show that this variability is likely to increase, particularly under high-emission scenarios such as SSP5-8.5 (red dashed line). The spread of uncertainty, represented by the shaded regions, becomes wider over time, indicating that precipitation extremes—both heavy rainfall events and dry spells—could become more frequent and intense. This is particularly concerning for the IGNP region, where water resources are already highly managed and dependent on seasonal rainfall for recharge.

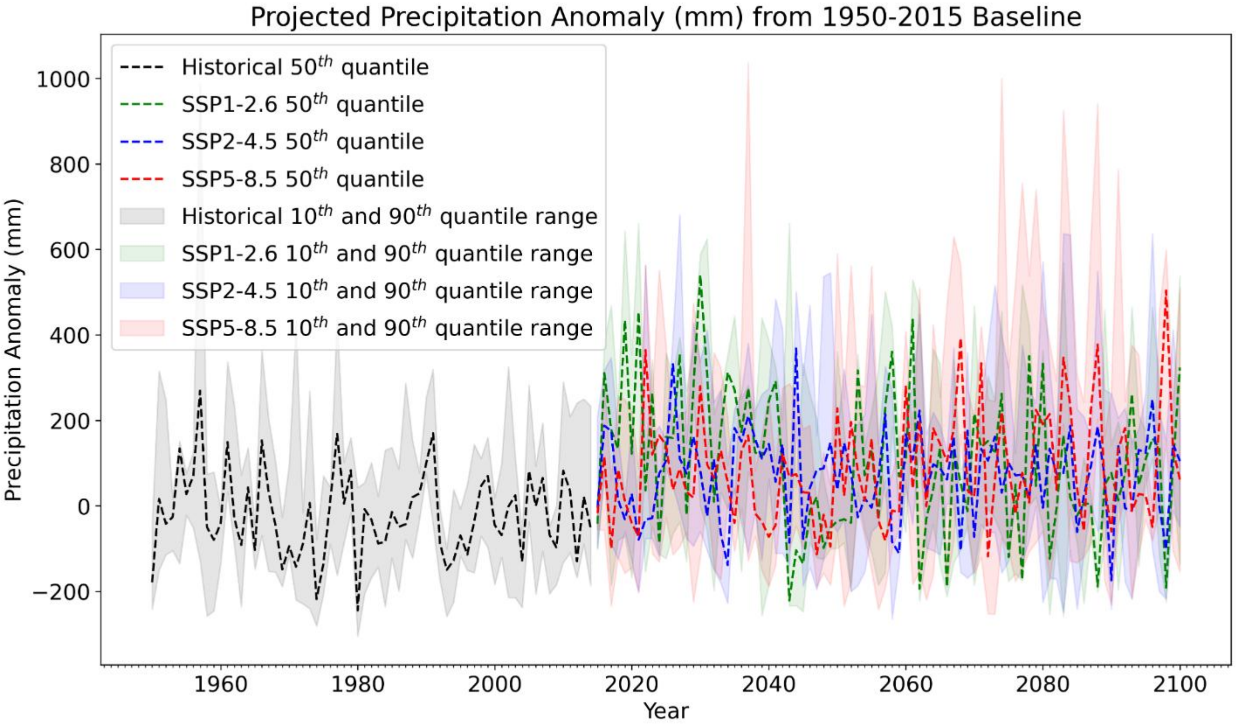

Figure – 8.7: Projected precipitation anomaly (mm) from 1950-2015 in upper IGNP region.

Under SSP1-2.6 (green dashed line), which represents a low-emission, high-mitigation scenario, precipitation variability is still present but appears relatively controlled compared to higher-emission pathways. SSP2-4.5 (blue dashed line) shows moderate fluctuations, while SSP5-8.5 exhibits the highest range of uncertainty and intensity of precipitation anomalies. The increased variability under SSP5-8.5 suggests that while some years may experience significantly higher rainfall, others may see severe deficits, posing challenges for long-term water management.

The projections also highlight the increasing difficulty in predicting future precipitation trends with precision. Unlike temperature, which shows a more consistent warming trend, precipitation is influenced by multiple factors such as monsoon variability, atmospheric circulation changes, and localized climatic conditions. The wide fluctuations in projected precipitation suggest that reliance on historical patterns for water management may no longer be sufficient, necessitating adaptive and dynamic planning approaches.

For the IGNP region, these projections underscore the need for robust water management strategies that can accommodate both excessive rainfall and extended dry periods. Increased precipitation variability means that storage infrastructure, such as reservoirs and groundwater recharge systems, will need to be optimized to capture and store excess rainfall during wet years for use during dry spells. Additionally, improvements in irrigation efficiency and adoption of climate-resilient agricultural practices will be critical to ensuring sustainable water use in response to unpredictable precipitation trends.

Overall, the projected precipitation anomalies for the IGNP region indicate a future where rainfall patterns are likely to be more erratic, with greater uncertainty in both timing and intensity. By integrating climate projections into decision-making processes, the IGNP region can be better prepared for the challenges posed by increasing precipitation variability and secure a stable water future for the communities that depend on it.

8.5.2 Future projections of Temperature

The projected temperature anomalies for the IGNP region indicate significant warming trends over the coming decades, with variations observed between the upper and lower parts of the canal command area. Based on climate scenarios from different Shared Socioeconomic Pathways (SSPs), the results highlight the potential impacts of climate change on temperature patterns, which could have far-reaching consequences for water resources, agriculture, and overall environmental conditions in the region.

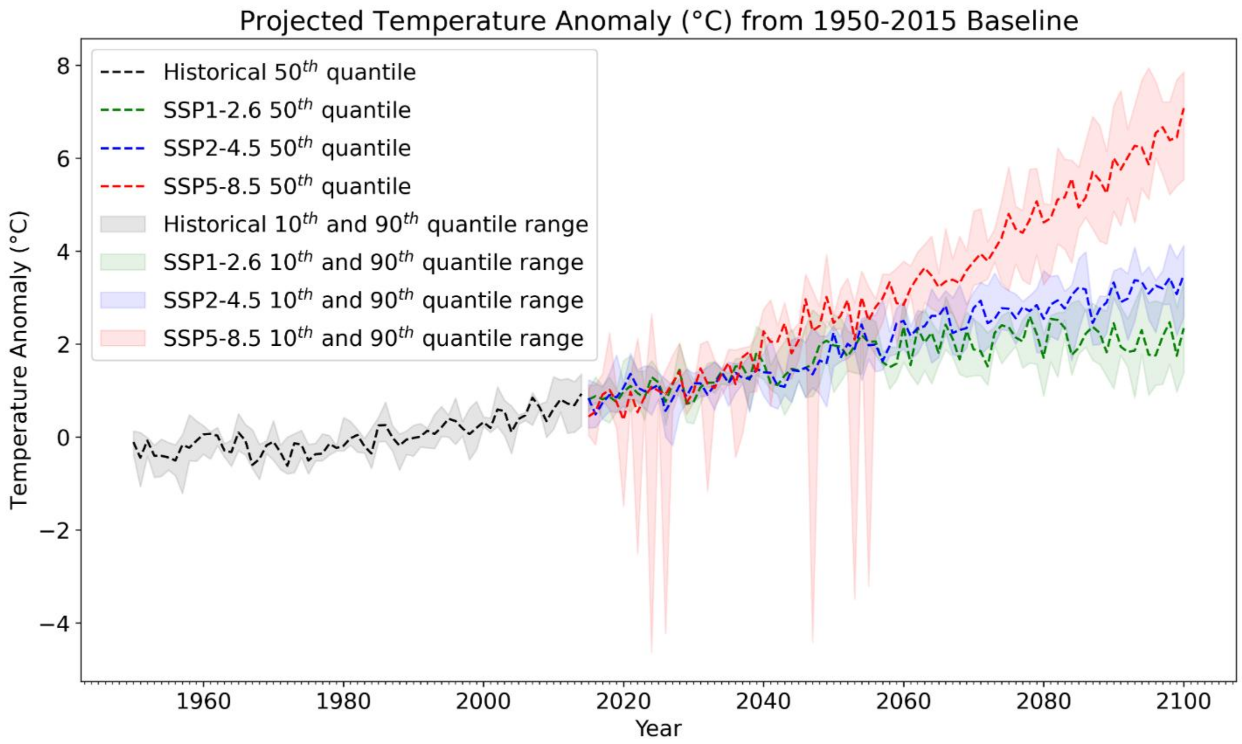

Figure – 8.8: Projected temperature anomaly (°C) from 1950-2015 in upper IGNP region.

In the upper part of the IGNP (**Figure 8.8**), temperature anomalies show a steady and substantial increase throughout the 21st century. The historical trend, represented by the black dashed line, indicates a gradual rise in temperature from 1950 to the present, with notable warming from the late 20th century onward. Future projections under different SSP scenarios exhibit varying degrees of warming, with the highest increase observed under SSP5-8.5 (red dashed line). This scenario, which represents high greenhouse gas emissions and minimal climate mitigation, shows a rapid rise in temperature anomalies after 2050, with a widening uncertainty range, suggesting increased climate variability. SSP2-4.5 (blue dashed line) presents a moderate increase, while SSP1-2.6 (green dashed line), representing aggressive climate mitigation, and results in the lowest projected warming. However, even under the most optimistic scenario, a notable temperature rise is still expected, indicating that climate change impacts cannot be entirely avoided.

A similar warming trend is observed in the lower part of the IGNP region, although the magnitude of temperature rise appears slightly lower compared to the upper command. The temperature anomaly projections for this region also show a clear distinction among different SSPs, with SSP5-8.5 exhibiting the most significant increase, followed by SSP2-4.5 and SSP1-2.6. The spread of uncertainty, particularly in the higher emission scenarios, suggests that climate extremes could become more pronounced, leading to greater variability in temperature patterns. This has critical implications for water availability, as increased temperatures can accelerate evapotranspiration rates, leading to higher water demand for irrigation and potential stress on groundwater resources.

These projections emphasize the urgent need for adaptive water management strategies within the IGNP command area. Rising temperatures will likely exacerbate existing challenges related to water scarcity, affecting both surface water and groundwater resources. The increase in temperature could also impact crop productivity, influencing the types of crops that can be cultivated and the irrigation schedules required to sustain agricultural output. Additionally, the widening uncertainty in temperature projections highlights the importance of climate-resilient infrastructure and policies to ensure the long-term sustainability of water resources in the region.

Given the high dependence on canal irrigation for sustaining livelihoods and agricultural activities, proactive steps must be taken to enhance water conservation measures, improve irrigation efficiency, and integrate climate-smart agricultural practices. By incorporating climate projections into water management planning, the IGNP region can be better prepared for the challenges posed by a warming climate and ensure that the canal command area remains productive and sustainable for future generations.

8.6 Application of Systems Model

The main objective of the present study was to estimate required groundwater extraction to restrict groundwater rise to avoid water-logging. A modeling framework (Systems model) has been employed in integration with WISDOM to simulate required groundwater extraction for conjunctive management.

The system model simulates evaporation and percolation losses in the main canal and the distributary canals, use of canal water to meet various demands (domestic/ industrial and irrigation) in the main canal and the distributary commands, additional GW pumping requirements to meet various demands (if could not be met from the available canal water), and the outflow to Stage II. The outputs of the system model are utilized in the WISDOM for groundwater modelling to map water-logged areas in the IGNP.

8.6.1 Supply and canal losses

Efficient water management in canal irrigation systems is essential for sustaining agricultural productivity and reducing groundwater dependence. This study evaluates three hypothetical scenarios for canals: lined and well maintained, lined and poorly maintained, and unlined. Each scenario impacts water availability, losses, and groundwater extraction differently, influencing overall system efficiency.

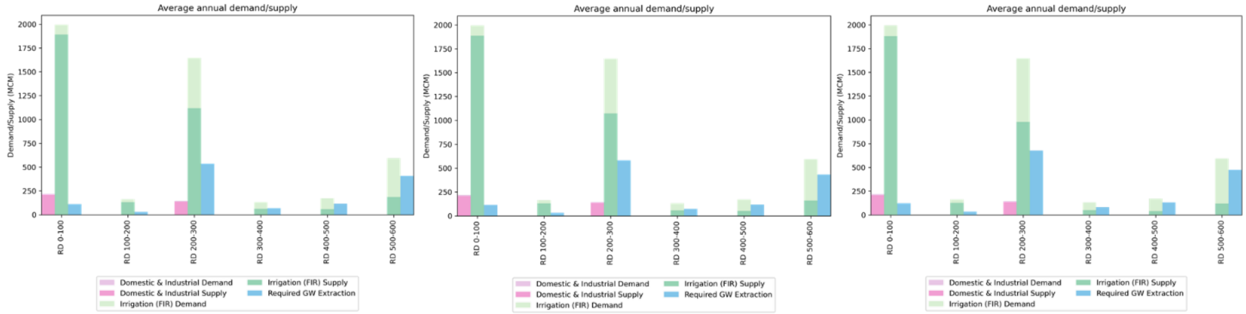

Figure – 8.9: Demand and supply in *lined and well maintained*, *lined and poorly maintained* and *unlined* canal scenarios.

In the lined and well-maintained scenario, it is assumed that the canal is regularly inspected and repaired, ensuring minimal seepage losses. The irrigation demand is approximately 2000 MCM in the stage-I, and the supply reaches 1750 MCM, with only 250 MCM required from groundwater. While the outflow to stage-II remains at ~500 MCM. Additionally, 78.8% of the total supply is utilized for irrigation, while percolation losses are observed to 8.0%, the lowest among all scenarios (Figures 8.9 & 8.10). This demonstrates that well-maintained canal linings significantly reduce losses.

In contrast, the lined but poorly maintained system leads to increased seepage losses. Although the irrigation demand remains 2000 MCM, the actual supply drops to 1500 MCM, requiring 500 MCM of groundwater extraction. The outflow to stage-II reduces to 450 MCM. In this scenario, irrigation supply decreases to 75%, and percolation losses increase to 12.7%, reducing the effectiveness of the system.

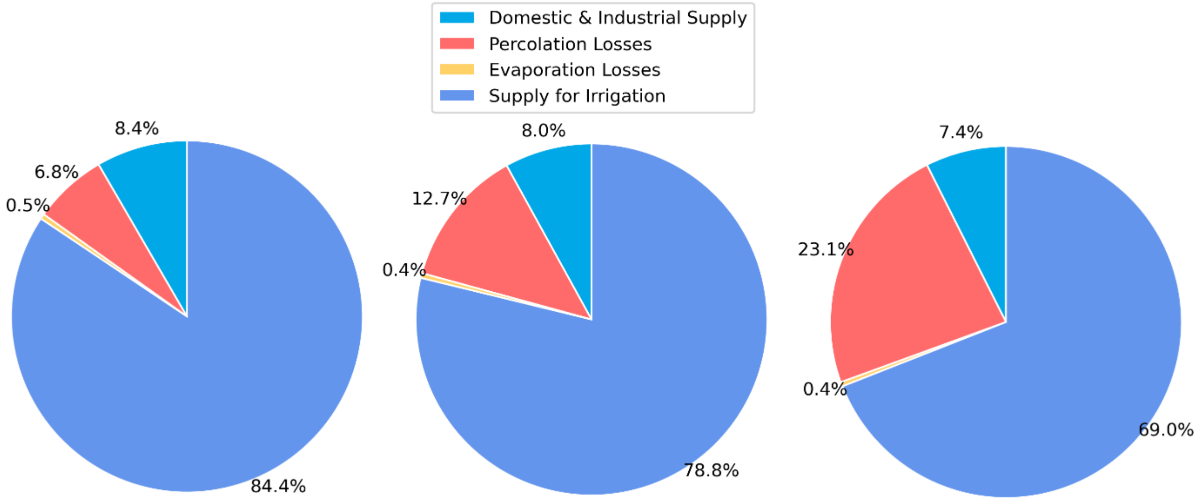

Figure – 8.10: Supply and demand proportions for *lined and well maintained*, *lined and poorly maintained* and *unlined* canal scenarios

The unlined scenario is the least efficient, with severe seepage losses reducing the available irrigation supply. With a demand of 2000 MCM, only 1200 MCM is supplied through the canal system, requiring extraction of 800 MCM from groundwater. The monthly inflow is similar to other scenarios at 600 MCM, but outflow drops sharply to 400 MCM, indicating high percolation losses. Only 70% of the total supply is utilized for irrigation, while 18% is lost to seepage. This results under different hypothetical scenarios elaborates the potential impacts caused by the condition of canal lining.

8.7 Results from Integrated Modelling for Conjunctive Management of Water Resources

8.7.1 Effect of Conjunctive Use Management Practices on Waterlogging

The study compares different scenarios of water management, including a Business as Usual (BAU) scenario and multiple Conjunctive Use (CU) scenarios, to analyze the effectiveness of different strategies in mitigating waterlogging. The analysis for 2015 highlights the impact of increased groundwater extraction on reducing waterlogged areas.

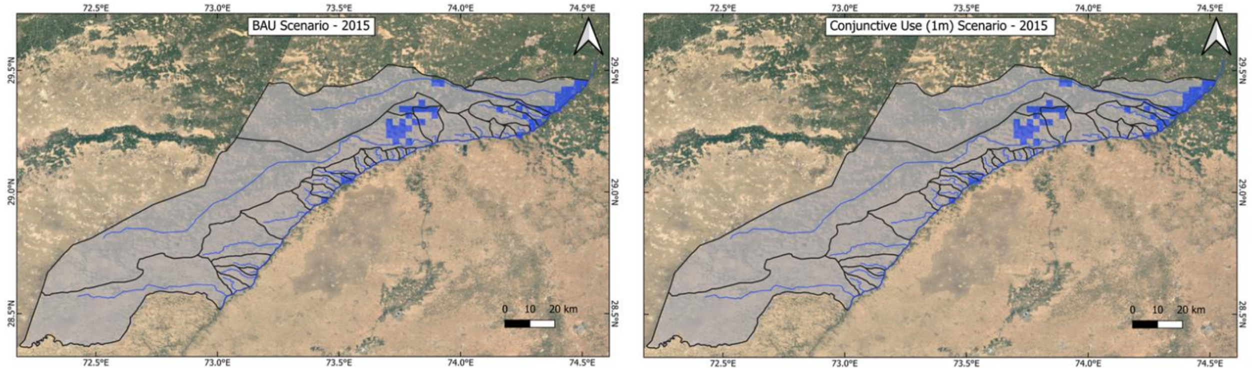

Figure – 8.11a: Waterlogged areas in BAU and CU (1m) Scenarios

In the BAU scenario, where water use practices remain unchanged, a significant portion of the command area exhibits severe waterlogging conditions, particularly in the upper reaches where canal irrigation is intensive. The blue pixels, representing waterlogged regions, indicate the consistent shallow groundwater levels. This situation suggests that under the existing scenario, waterlogging persists in these identified areas.

To quantify the amount of groundwater extraction required to reduce water-logging, five scenarios (1m, 2m, 3m, 4m and 5m) of conjunctive management are formulated. In these scenarios, the pumping is estimated automatically in the model by calculating groundwater extraction required to drop the water table to a specified depth from surface. For instance, in the scenario 1m, the extractions are estimated to decline the water table to 1 m depth. The groundwater extraction is input to MODFLOW model for groundwater flow simulation, which is then utilized to map water-logged areas.

As groundwater extraction is introduced in the CU (1m) scenario, a noticeable reduction in waterlogged areas can be observed. Although some regions still experience waterlogging, particularly in localized depressions, there is an evident improvement compared to the BAU scenario. This suggests that even a moderate level of groundwater withdrawal contributes to lowering of water table, preventing surface water accumulation.

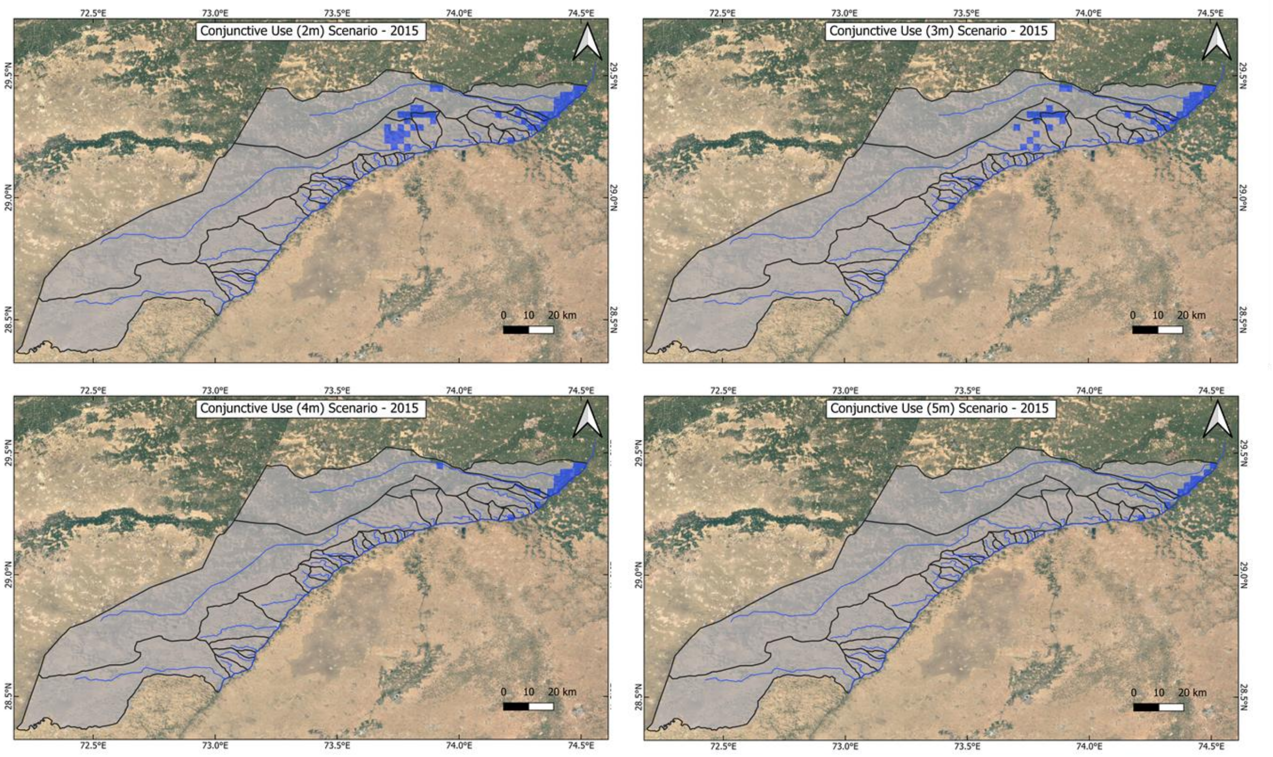

Figure – 8.11b: Waterlogged areas in CU (2m), CU (3m), CU (4m) and CU (5m) Scenarios.

A further increase in groundwater pumping in the CU (2m) and CU (3m) scenarios results in a more pronounced reduction in waterlogged area. In the CU (4m) and CU (5m) scenarios, only a few isolated pockets of waterlogging remain.

Overall, the results from 2015 emphasize the importance of adopting a conjunctive water management strategy, where surface water irrigation is complemented with controlled groundwater extraction. Implementing such measures can significantly alleviate waterlogging, improving agricultural viability and land productivity in the IGNP region.

The above analysis demonstrates that groundwater withdrawal plays a key role in managing water levels and reducing the extent of waterlogging. However, in the IGNP, it is observed that the groundwater is saline and may not be utilized directly for irrigation. Based on water quality analysis and geophysical survey, it is observed that a thin layer of fresh groundwater exists in the area which can be utilized for irrigation. However, extensive groundwater extraction is not feasible in the area due to high salinity in groundwater.

8.7.2 Relation between Groundwater Extraction and Waterlogging in the IGNP Region under Different Conjunctive Use Scenarios

To mitigate waterlogging, different levels of groundwater extraction scenarios were analyzed. The analysis compares the Business as Usual (BAU) scenario, where no additional groundwater extraction is considered, with Conjunctive Use (CU) scenarios, which include varying levels of groundwater extraction.

The results indicate a direct inverse relationship between groundwater extraction and waterlogged area. The BAU scenario consistently shows the highest extent of waterlogging.

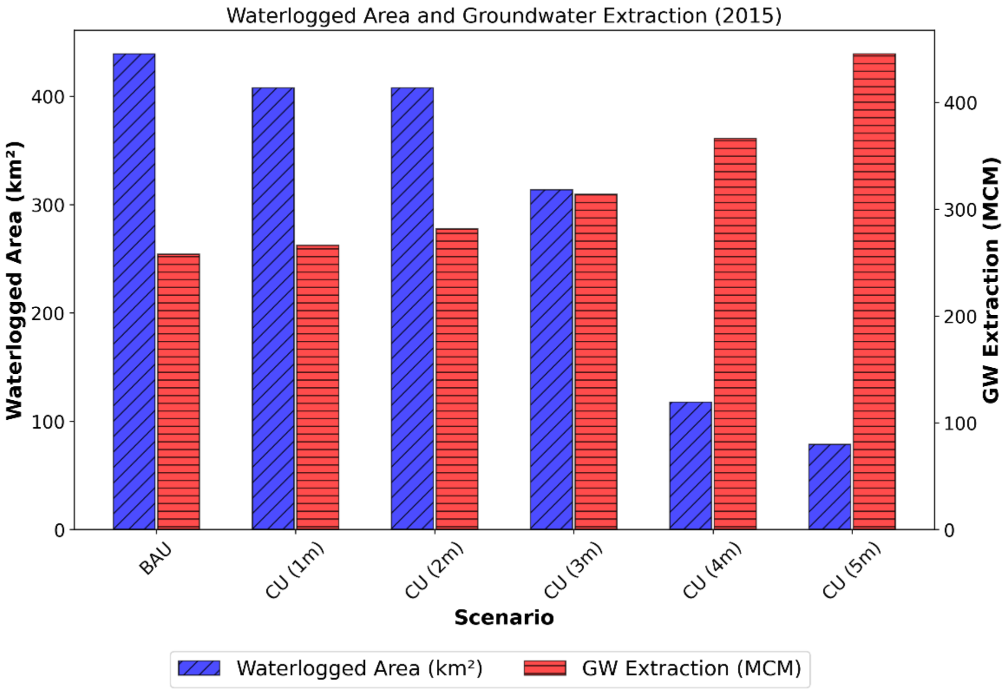

Figure – 8.12: Waterlogged area and groundwater extraction (2015)

As groundwater extraction increases in the CU scenarios, a significant reduction in waterlogged areas is observed. Under BAU scenario, around 430 km^2 area found to be within 3 m depth to groundwater (water-logged area) with a groundwater extraction of 250 MCM. The water-logged area decreases to 70 km^2 when the groundwater extraction is increases to 450 MCM.

8.8 Impact of Climate Change on demand in IGNP Command

The Field Irrigation Requirement (FIR) simulations indicate an expected contrasting pattern to precipitation. Under SSP245, irrigation requirements remain relatively stable, with periodic fluctuations driven by seasonal variations in rainfall and temperature. However, in SSP585, irrigation demands exhibit higher peaks and variability. The irrigation demand is expected to increase in the future due to inconsistent rainfall and higher evapotranspiration rates (Figure 8.13).

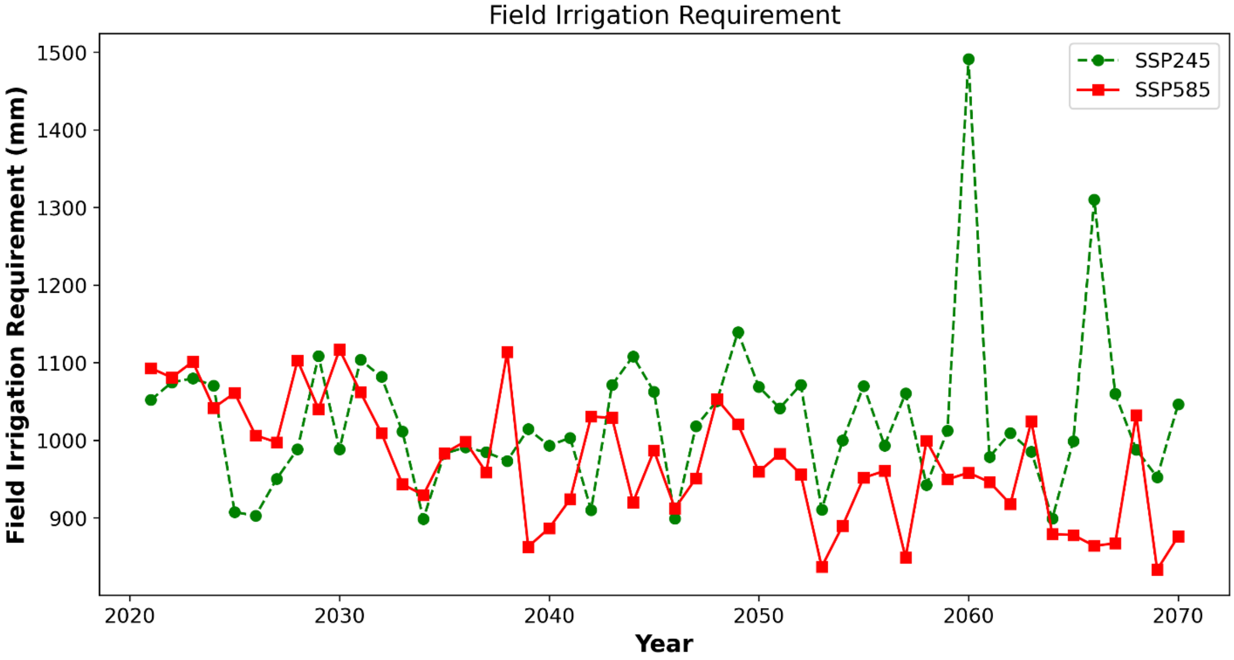

Figure – 8.13: Simulated Field Irrigation Requirement (FIR) under different SSPs (2021-2070)

These findings emphasize the need for a conjunctive water management approach, to mitigate the risks associated with climate variability. Future policies should focus on enhancing irrigation efficiency, and developing adaptive strategies to cope with extreme weather patterns. The insights from this integrated modelling approach provide a foundation to develop robust water management plans that ensure long-term agricultural sustainability and water security.

* * *

CHAPTER – 9

CONCLUDING REMARKS

The Indira Gandhi Nahar Pariyojana (IGNP) is one of India's largest canal irrigation projects, which has contributed significantly to the socio-economic development of the region. It provides potable water to the Thar Desert to meet various water demands. However, despite multi-facet benefits, the project has been criticized by many due to waterlogging and related issues in some patches of the IGNP. A comprehensive study to know the present status of groundwater in the area, the current water-logging area, and conjunctive management scenarios was essential. The study aims to assess the current groundwater scenario, map waterlogged areas using remote sensing, estimate groundwater recharge, and explore conjunctive water management strategies to ensure sustainable water use in the IGNP command area.

In this study, geophysical survey was performed using Electrical Resistivity Tomography (ERT) to investigate subsurface geologic conditions and identify thickness of fresh groundwater in some affected areas of IGNP stage-I. Four subsurface zones corresponding to freshwater, the fresh-saline water interface, saline water, and the unsaturated zone were identified. These zones were interpreted by analyzing the resistivity ranges observed in the individual ERT sections and correlating them with known hydrogeological conditions in the IGNP region. It is observed that the fresh groundwater is available till only a few meters of depth. The thickness of the fresh water zone decreases as the distance from the canal increases. Indicating that the canal contributes considerably to groundwater recharge.

Real-time information about the water-logging in the sensitive areas is useful to plan management strategies. In this study, a web-based application (hosted at https://ee-surveydaman.projects.earthengine.app/view/ignp-water-monitoring-app) is developed to map the water-logged area for the period of interest. In addition, the area under surface flooding is quantified for the period from 1987 to 2023 for the Stage-I of IGNP. Hanumangarh and Sri Ganganagar were identified as the districts with most areas having waterlogging conditions. In the initial phase from 1987, both the districts show an initial rise in the waterlogged areas, leading to an initial peak in waterlogging in the year 1990, with the total area affected by waterlogging peaking at around 58 km^2. For the initial peak year of 1990, out of the total waterlogged area, Sri Ganganagar was the most affected, with the total area affected by waterlogging adding up to around 39 km^2. For the same year, the area of Hanumagarh district affected by waterlogging was around 18 km^2. The increase in waterlogging in the late 1980s could be attributed to canal leakages and the development phase of the canal, leading extensively to waterlogging. After 1997, a significant decline in waterlogged areas has been observed in both districts. The decreasing trend has been observed after 1997. The period after 2015 shows a gradual increase in waterlogged areas, particularly noticeable in the latest years (2022-2023), which can be attributed to variability in precipitation.

To propose groundwater extraction for conjunctive management in the IGNP, an integrated model is set-up for stage-I of IGNP. Recharge to groundwater due to precipitation and canal percolation are estimated using the integrated model. Before the conjunctive management simulation, a hypothetical scenario is formulated to quantify canal percolation to assess the impact of canal lining. Under *well-maintained lining*, canals have the lowest percolation loss (8.0%). The *poorly maintained lined* canals experience increased seepage (12.7%). *Unlined canals* exhibit the highest seepage losses (18.0%), leading to high groundwater recharge and waterlogging.

To quantify the amount of groundwater extraction required to reduce water-logging, five scenarios (1m, 2m, 3m, 4m and 5m) of conjunctive management are formulated. In these scenarios, the pumping is estimated automatically in the model by calculating groundwater extraction required to drop the water table to a specified depth from the surface. For instance, in the scenario 1m, the extractions are estimated to decline the water table to 1 m depth. The groundwater extraction is input to MODFLOW model for groundwater flow simulation, which is then utilized to map water-logged areas. As groundwater extraction increases in the Conjunctive Use (CU) scenarios, a significant reduction in waterlogged areas is observed. Under BAU scenario, around 430 km^2 area found to be within 3 m depth to groundwater (water-logged area) with a groundwater extraction of 250 MCM. The water-logged area decreases to 70 km^2 when the groundwater extraction is increases to 450 MCM. The above analysis demonstrates that groundwater withdrawal plays a key role in managing water levels and reducing the extent of waterlogging. However, in the IGNP, it is observed that the groundwater is saline and may not be utilized directly for irrigation. Based on water quality analysis and geophysical survey, it is observed that a thin layer of fresh groundwater exists in the area which can be utilized for irrigation. However, extensive groundwater extraction is not feasible in the area due to high salinity in groundwater.

The projected temperature anomalies for the IGNP region indicate significant warming trends over the coming decades, with variations observed between the upper and lower parts of the canal command area. Based on climate scenarios from different Shared Socioeconomic Pathways (SSPs), the results highlight the potential impacts of climate change on temperature patterns, which could have far-reaching consequences for water resources, agriculture, and overall environmental conditions in the region. Precipitation patterns in the IGNP region are expected to undergo significant fluctuations over the coming decades, as indicated by the projections under different SSPs. The precipitation anomaly trends suggest increased variability, with periods of excess rainfall interspersed with potential drought conditions. These changes in precipitation will have crucial implications for water availability, irrigation scheduling, and groundwater recharge in the IGNP command area. The irrigation requirement is projected to increase in the future under the moderate climatic scenario (SSP585), while irrigation demand might decrease due to increased precipitation under the moderate climatic scenario (SSP245). The current irrigation demand (field irrigation requirement) is estimated to be 2000 MCM in the stage-I.

The study highlights the critical role of canal lining and groundwater management in mitigating waterlogging in the IGNP region. Well-maintained lined canals exhibit the lowest percolation losses (8.0%), while poorly maintained and unlined canals lead to increased seepage, exacerbating waterlogging issues. Conjunctive water use scenarios demonstrate that controlled groundwater extraction can significantly reduce waterlogged areas, but high salinity limits its direct use for irrigation. Additionally, climate projections indicate rising temperatures and fluctuating precipitation patterns, impacting future water availability and irrigation demand. A strategic approach combining canal maintenance, groundwater management, and climate adaptation is essential for ensuring sustainable water use in the IGNP command area.

REFERENCES

Allen, R. G., Pereira, L. S., Raes, D. and Smith, M., 1998, Guidelines for computing crop water requirements. FAO Irrigation and Drainage Paper No. 56. Food and Agriculture Organization, Rome, 333 pp.

Campos, J. C., Sillero, N., & Brito, J. C. (2012). Normalized Difference Water Indexes have dissimilar performances in detecting seasonal and permanent water in the Sahara-Sahel transition zone. Journal of Hydrology, 464–465, 438–446. https://doi.org/10.1016/j.jhydrol.2012.07.042

Coltin, B., McMichael, S., Smith, T., Fong, T., 2016. Automatic boosted flood mapping from satellite data. Int. J. Remote Sens. 37 (5), 993–1015.

Den Besten, N., Steele-Dunne, S., de Jeu, R., & van der Zaag, P. (2021). Towards Monitoring Waterlogging with Remote Sensing for Sustainable Irrigated Agriculture, Remote Sens., 13, 2929.

Doorenbos, J., Pruitt, W.O., 1977, Guidelines for predicting crop water requirements. FAO Irrigation and Drainage Paper No. 24. Food and Agriculture Organization, Rome, 144 pp.

Eyring, V., Bony, S., Meehl, G.A., Senior, C., Stevens, B., Stouffer, R.J. and Taylor, K.E., 2015. Overview of the Coupled Model Intercomparison Project Phase 6 (CMIP6) experimental design and organisation. Geoscientific Model Development Discussions, 8(12).

Feyisa, G. L., Meilby, H., Fensholt, R., & Proud, S. R. (2014). Automated Water Extraction Index: A new technique for surface water mapping using Landsat imagery. Remote Sensing of Environment, 140, 23–35. https://doi.org/10.1016/j.rse.2013.08.029

Fisher, A., Flood, N., & Danaher, T. (2016). Comparing Landsat water index methods for automated water classification in eastern Australia. Remote Sensing of Environment, 175, 167–182. https://doi.org/10.1016/j.rse.2015.12.055

Frazier, P. S., & Page, K. J. (2000). Water body detection and delineation with Landsat TM data. Photogrammetric Engineering & Remote Sensing, 66(12), 1461–1467.

Gao, B. C. (1996). NDWI – A Normalized Difference Water Index for remote sensing of vegetation liquid water from space. Remote Sensing of Environment, 58(3), 257–266. https://doi.org/10.1016/S0034-4257(96)00067-3

Global Forest Watch, 2014. World Resources Institute, Washington, DC. http://www. globalforestwatch.org (accessed June 30, 2016).

Gorelick, N., Hancher, M., Dixon, M., Ilyushchenko, S., Thau, D., & Moore, R. (2017). Google Earth Engine: Planetary-scale geospatial analysis for everyone. Remote sensing of Environment, 202, 18-27.

Government of Rajasthan, India, 1999, IGNP Studies for the State of Rajasthan. Final Report (Supporting Report 1: Remote Sensing Application Studies).

FAO/UNDP, 1971, Soil Survey and Soil and Water Management Research and Demonstration in the Rajasthan Canal Area, India. AGL: SF/IND 24, Technical Report 1.4.

Hamed, K. H., & Rao, A. R. (1998). A modified Mann-Kendall trend test for auto-correlated data. Journal of Hydrology, 204(1-4), 182-196. doi:10.1016/S0022-1694(97)00125-X

Hansen, M.C., Potapov, P.V., Moore, R., Hancher, M., Turubanova, S.A., Tyukavina, A., et al., 2013. High-resolution global maps of 21st-century forest cover change. Science 342, 850–853.

Hansen, C. (2015). Google Earth Engine as a platform for making remote sensing of water resources a reality for monitoring Inland waters. https://doi.org/10.13140/RG.2.1.3688.1047

Harbaugh, A. W., and McDonald, M. G., (1996). User's documentation for MODFLOW-96, an update to the U.S. Geological Survey modular finite-difference ground-water flow model. Open-File Report 96-485. U.S. Geological Survey.

Harbaugh, Arlen W., (2005). MODFLOW-2005, the U.S. Geological Survey Modular Ground-Water Model—the Ground-Water Flow Process. Techniques and Methods 6–A16. U.S. Geological Survey.

Hooja, R., Sreenivas, V. and Sharma, G., 1995, Water and Salinity Problems in IGNP, Rajasthan. Proceedings of the National Seminar on Reclamation and Management of Waterlogged Saline Soils, K. V. G. K. Rao, M. C. Agarwal, O.P. Singh and R. J. Oosterbaan (Eds), CSSRI, Karnal, pp. 141–159.

Huang, W., Duan, W., Nover, D., Sahu, N., & Chen, Y. (2021). An integrated assessment of surface water dynamics in the Irtysh River Basin during 1990–2019 and exploratory factor analyses. *Journal of Hydrology*, *593*, 125905.

Joshi, A.R., Dinerstein, E., Wikramanayake, E., et al., 2016. Tracking changes and preventing loss in critical tiger habitat. Sci. Adv. 2 (4), e1501675.

Langevin, C. D., Hughes, J. D., Banta, E. R., Niswonger, R. G., Panday, S., & Provost, A. M. (2017). Documentation for the MODFLOW 6 Groundwater Flow Model: U.S. Geological Survey Techniques and Methods. In USGS: Techniques and Methods 6-A55. https://doi.org/https://doi.org/10.3133/tm6A55

Lobell, D., Thau, D., Seifert, C., Engle, E., Little, B., 2015. A scalable satellite-based crop yield mapper. Remote Sens. Environ. 164, 324–333.

McFeeters, S. K. (1996). The use of the Normalized Difference Water Index (NDWI) in the delineation of open water features. International Journal of Remote Sensing, 17(7), 1425–1432. https://doi.org/10.1080/01431169608948714

McFeeters, S. K. (2013). Using the Normalized Difference Water Index (NDWI) within a geographic information system to detect swimming pools for mosquito abatement: A practical approach. Remote Sensing, 5(7), 3544–3561. https://doi.org/10.3390/rs5073544

National Water Development Agency (2018). "Guidelines for working out preliminary water balance in a river basin as finalized by Task Force for ILR in its 9th meeting".

Patel, N., Angiuli, E., Gamba, P., Gaughan, A., Lisini, G., Stevens, F., Tatem, A., Trianni, A., 2015. Multitemporal settlement and population mapping from Landsat using google earth engine. Int. J. Appl. Earth Obs. Geoinf. 35, 199–208.

Pekel, J.F., Cottam, A., Gorelick, N., Belward, A.S., 2016. High-resolution mapping of global surface water and its long-term changes. Nature.

Ritchie, J. T. (1972). Model for predicting evaporation from a row crop with incomplete cover. Water resources research, 8(5), 1204-1213.

Rokni, K., Ahmad, A., Selamat, A., & Hazini, S. (2014). Water feature extraction and change detection using multitemporal Landsat imagery. Remote Sensing, 6(5), 4173–4189. https://doi.org/10.3390/rs6054173

Singh, K. V., Setia, R., Sahoo, S., Prasad, A., & Pateriya, B. (2015). Evaluation of NDWI and MNDWI for assessment of waterlogging by integrating digital elevation model and groundwater level. Geocarto International, 30(6), 650–661. https://doi.org/10.1080/10106049.2014.965757.

Singh, S. and Kar, A., 1991, Morphological characteristics of landforms and associated problems. In Prospect of Indira Gandhi Canal Project, J. Venkateswarulu and I. P. Abrol (Eds), pp. 11–18 (New Delhi: ICAR).

Soulard, C.E., Albano, C.M., Villarreal, M.L., Walker, J.J., 2016. Continuous 1985–2012 Landsat monitoring to assess fire effects on meadows in Yosemite National Park, California. Remote Sens. 8 (5), 371.

Sturrock, H.J., Cohen, J.M., Keil, P., Tatem, A.J., Le Menach, A., Ntshalintshali, N.E., Hsiang, M.S., Gosling, R.D., 2014. Fine-scale malaria risk mapping from routine aggregated case data. Malar. J. 13 (1), 1.

Tamiminia, H., Salehi, B., Mahdianpari, M., Quackenbush, L., Adeli, S., & Brisco, B. (2020). Google Earth Engine for geo-big data applications: A meta-analysis and systematic review. *ISPRS Journal of Photogrammetry and Remote Sensing*, *164*, 152-170.

Thornthwaite, C. W., and Mather, J. R., 1957, Instructions and tables for computing potential evapotranspiration and the water balance: Publications in Climatology, v. 10, no. 3, p. 1–104.

Wang, M., Du, L., Ke, Y., Huang, M., Zhang, J., Zhao, Y., & Gong, H. (2019). Impact of climate variabilities and human activities on surface water extents in reservoirs of Yongding River Basin, China, from 1985 to 2016 based on Landsat observations and time series analysis. *Remote Sensing*, *11*(5), 560.

Westenbroek, S. M., Engott, J. A., Kelson, V. A., and Hunt, R. J., 2018, SWB Version 2.0—A Soil-Water-Balance code for estimating net infiltration and other water-budget components: U.S. Geological Survey Techniques and Methods, book 6, chap. A59, 118 p., https://doi.org/10.3133/tm6A59

Xu, H. (2006). Modification of normalised difference water index (NDWI) to enhance open water features in remotely sensed imagery. *International journal of remote sensing*, *27*(14), 3025-3033.

Zhang, Q., Li, B., Thau, D., Moore, R., 2015. Building a better urban picture: combining day and night remote sensing imagery. Remote Sens. 7 (9), 11887–11913.

Zhou, H., Liu, S., Hu, S., & Mo, X. (2021). Retrieving dynamics of the surface water extent in the upper reach of Yellow River. *Science of the Total Environment*, *800*, 149348.

Zou, Z., Dong, J., Menarguez, M. A., Xiao, X., Qin, Y., Doughty, R. B., & Hambright, K. D. (2017). Continued decrease of open surface water body area in Oklahoma during 1984–2015. *Science of the Total Environment*, *595*, 451-460.

ANNEXURES

Annexure 8.1a: Commandwise Groundwater Recharge, Groundwater Extraction and Waterlogged Area. (BAU Scenario).

S.No	Command	2015		
		GW Recharge (MCM)	**GW Extraction (MCM)**	**Waterlogged Area (km^2)**
1	Masitawali	64.25	29.72	62.72
2	Suratgarh	86.08	56.53	39.20
3	Zorawarpura	10.86	3.42	39.20
4	Sardarpura	16.50	8.17	47.04
5	Khedasari	9.31	1.63	15.68
6	Thethar	7.47	1.16	7.84
7	Kanau	2.66	1.43	0.00
8	Bhojewala1	9.62	3.00	0.00
9	Bhojewala2	26.36	4.93	15.68
10	Piperan	11.90	3.99	54.88
11	Anupgarh	125.45	50.60	109.76
12	Govinda	3.59	0.48	0.00
13	Birmana1	3.35	0.71	0.00
14	Birmana2	5.24	0.97	0.00
15	Dungiawali	8.10	1.77	0.00
16	Sukhchainpura	2.40	0.49	0.00
17	Bhaktawarpura	4.71	1.21	0.00
18	Govindsar	4.03	1.15	0.00
19	Bhopalpura	4.36	0.20	15.68
20	Surjansar	7.88	0.90	15.68
21	Gomawali	6.14	1.78	0.00
22	Takhatpura	9.87	2.96	7.84
23	Kanakpura	9.79	5.59	7.84
24	Sherpura	32.49	18.65	0.00
25	Rozri	27.82	10.65	0.00
26	Chattargarh1	7.26	0.00	0.00
27	Chattargarh2	1.37	0.00	0.00
28	Awa	6.78	0.00	0.00
29	Sattasar	7.59	0.00	0.00
30	Pugal	35.32	45.71	0.00
Total		**558.52**	**257.79**	**439.04**

Annexure 8.1b: Commandwise Groundwater Recharge, Groundwater Extraction and Waterlogged Area. (Conjunctive Use (1m) Scenario).

S.No	Command	2015		
		GW Recharge (MCM)	GW Extraction (MCM)	Waterlogged Area (km^2)
1	Masitawali	62.86	29.88	62.72
2	Suratgarh	79.50	56.81	47.04
3	Zorawarpura	14.71	3.91	39.20
4	Sardarpura	20.69	9.13	31.36
5	Khedasari	5.11	2.09	7.84
6	Thethar	4.58	1.46	7.84
7	Kanau	3.52	1.43	0.00
8	Bhojewala1	9.60	3.06	0.00
9	Bhojewala2	23.72	5.03	15.68
10	Piperan	4.87	4.73	54.88
11	Anupgarh	119.88	53.61	109.76
12	Govinda	3.07	0.48	0.00
13	Birmana1	1.25	0.72	0.00
14	Birmana2	4.24	0.98	0.00
15	Dungiawali	2.65	1.79	0.00
16	Sukhchainpura	0.38	0.49	0.00
17	Bhaktawarpura	0.97	1.22	0.00
18	Govindsar	2.33	1.15	0.00
19	Bhopalpura	2.89	0.56	7.84
20	Surjansar	5.45	1.42	7.84
21	Gomawali	2.19	1.78	0.00
22	Takhatpura	6.94	3.22	7.84
23	Kanakpura	7.95	5.89	7.84
24	Sherpura	27.80	18.72	0.00
25	Rozri	32.39	10.69	0.00
26	Chattargarh1	8.62	0.00	0.00
27	Chattargarh2	0.40	0.00	0.00
28	Awa	6.03	0.00	0.00
29	Sattasar	6.86	0.00	0.00
30	Pugal	26.82	45.85	0.00
Total		**498.28**	**266.10**	**407.68**

Annexure 8.1c: Commandwise Groundwater Recharge, Groundwater Extraction and Waterlogged Area. (Conjunctive Use (2m) Scenario).

S.No	Command	2015		
		GW Recharge (MCM)	GW Extraction (MCM)	Waterlogged Area (km^2)
1	Masitawali	62.96	30.59	70.56
2	Suratgarh	79.87	57.09	62.72
3	Zorawarpura	14.78	5.38	47.04
4	Sardarpura	20.80	11.53	39.20
5	Khedasari	5.06	2.83	7.84
6	Thethar	4.56	1.90	7.84
7	Kanau	3.52	1.43	0.00
8	Bhojewala1	9.61	3.06	0.00
9	Bhojewala2	23.73	5.30	15.68
10	Piperan	4.88	6.05	54.88
11	Anupgarh	119.74	58.87	133.28
12	Govinda	3.07	0.48	0.00
13	Birmana1	1.26	0.72	0.00
14	Birmana2	4.24	0.98	0.00
15	Dungiawali	2.65	1.79	0.00
16	Sukhchainpura	0.38	0.49	0.00
17	Bhaktawarpura	0.97	1.22	0.00
18	Govindsar	2.33	1.15	0.00
19	Bhopalpura	2.85	0.94	7.84
20	Surjansar	5.41	1.97	7.84
21	Gomawali	2.19	1.78	0.00
22	Takhatpura	6.94	3.93	7.84
23	Kanakpura	7.96	6.64	7.84
24	Sherpura	27.83	18.72	0.00
25	Rozri	32.40	10.69	0.00
26	Chattargarh1	8.62	0.00	0.00
27	Chattargarh2	0.40	0.00	0.00
28	Awa	6.03	0.00	0.00
29	Sattasar	6.86	0.00	0.00
30	Pugal	26.82	45.85	0.00
Total		**498.72**	**281.41**	**470.40**

Annexure 8.1d: Commandwise Groundwater Recharge, Groundwater Extraction and Waterlogged Area. (Conjunctive Use (3m) Scenario).

S.No	Command	2015		
		GW Recharge (MCM)	GW Extraction (MCM)	Waterlogged Area (km^2)
1	Masitawali	62.84	32.85	54.88
2	Suratgarh	79.53	58.15	39.20
3	Zorawarpura	14.54	6.93	31.36
4	Sardarpura	20.43	14.02	23.52
5	Khedasari	4.99	3.58	7.84
6	Thethar	4.54	2.35	7.84
7	Kanau	3.52	1.43	0.00
8	Bhojewala1	9.61	3.06	0.00
9	Bhojewala2	23.74	5.73	15.68
10	Piperan	5.00	9.27	47.04
11	Anupgarh	120.43	75.83	54.88
12	Govinda	3.07	0.48	0.00
13	Birmana1	1.25	0.72	0.00
14	Birmana2	4.24	0.98	0.00
15	Dungiawali	2.65	1.79	0.00
16	Sukhchainpura	0.38	0.49	0.00
17	Bhaktawarpura	0.97	1.22	0.00
18	Govindsar	2.32	1.15	0.00
19	Bhopalpura	2.84	1.66	7.84
20	Surjansar	5.38	2.99	7.84
21	Gomawali	2.19	1.78	0.00
22	Takhatpura	6.87	4.64	7.84
23	Kanakpura	7.89	7.40	7.84
24	Sherpura	27.83	18.72	0.00
25	Rozri	32.40	10.69	0.00
26	Chattargarh1	8.62	0.00	0.00
27	Chattargarh2	0.40	0.00	0.00
28	Awa	6.03	0.00	0.00
29	Sattasar	6.86	0.00	0.00
30	Pugal	26.82	45.85	0.00
Total		**498.16**	**313.79**	**313.60**

Annexure 8.1e: Commandwise Groundwater Recharge, Groundwater Extraction and Waterlogged Area. (Conjunctive Use (4m) Scenario).

S.No	Command	2015		
		GW Recharge (MCM)	GW Extraction (MCM)	Waterlogged Area (km^2)
1	Masitawali	62.76	36.52	70.56
2	Suratgarh	78.36	60.33	47.04
3	Zorawarpura	14.24	8.62	23.52
4	Sardarpura	19.89	16.89	7.84
5	Khedasari	4.96	4.33	7.84
6	Thethar	4.53	2.79	7.84
7	Kanau	3.52	1.43	0.00
8	Bhojewala1	9.60	3.06	0.00
9	Bhojewala2	24.13	6.68	0.00
10	Piperan	4.00	13.93	0.00
11	Anupgarh	118.71	105.09	0.00
12	Govinda	3.06	0.48	0.00
13	Birmana1	1.24	0.72	0.00
14	Birmana2	4.14	1.02	0.00
15	Dungiawali	2.64	1.79	0.00
16	Sukhchainpura	0.38	0.49	0.00
17	Bhaktawarpura	0.97	1.22	0.00
18	Govindsar	2.09	1.85	0.00
19	Bhopalpura	2.70	2.77	7.84
20	Surjansar	5.14	5.19	7.84
21	Gomawali	2.16	2.28	0.00
22	Takhatpura	6.84	5.35	7.84
23	Kanakpura	7.86	8.15	7.84
24	Sherpura	27.82	18.72	0.00
25	Rozri	32.40	10.69	0.00
26	Chattargarh1	8.62	0.00	0.00
27	Chattargarh2	0.40	0.00	0.00
28	Awa	6.03	0.00	0.00
29	Sattasar	6.86	0.00	0.00
30	Pugal	26.82	45.85	0.00
Total		**492.87**	**366.25**	**196.00**

Annexure 8.1f: Commandwise Groundwater Recharge, Groundwater Extraction and Waterlogged Area. (Conjunctive Use (5m) Scenario).

S.No	Command	2015		
		GW Recharge (MCM)	GW Extraction (MCM)	Waterlogged Area (km^2)
1	Masitawali	61.71	40.28	54.88
2	Suratgarh	77.64	64.39	7.84
3	Zorawarpura	13.94	10.66	0.00
4	Sardarpura	19.50	20.24	0.00
5	Khedasari	4.92	5.68	7.84
6	Thethar	4.50	3.80	7.84
7	Kanau	3.51	1.43	0.00
8	Bhojewala1	9.60	3.06	0.00
9	Bhojewala2	23.91	7.96	0.00
10	Piperan	3.20	20.92	0.00
11	Anupgarh	117.82	151.46	0.00
12	Govinda	3.06	0.48	0.00
13	Birmana1	1.22	0.72	0.00
14	Birmana2	4.09	1.83	0.00
15	Dungiawali	2.60	2.27	0.00
16	Sukhchainpura	0.38	0.49	0.00
17	Bhaktawarpura	0.96	1.22	0.00
18	Govindsar	2.03	3.10	0.00
19	Bhopalpura	2.63	3.92	0.00
20	Surjansar	4.94	8.17	0.00
21	Gomawali	2.07	3.06	0.00
22	Takhatpura	6.78	6.06	0.00
23	Kanakpura	7.80	8.91	0.00
24	Sherpura	27.83	18.72	0.00
25	Rozri	32.40	10.69	0.00
26	Chattargarh1	8.62	0.00	0.00
27	Chattargarh2	0.40	0.00	0.00
28	Awa	6.03	0.00	0.00
29	Sattasar	6.86	0.00	0.00
30	Pugal	26.81	45.85	0.00
Total		**487.77**	**445.38**	**78.40**